

UC San Diego

UC San Diego Electronic Theses and Dissertations

Title

Developments and applications of tools for studying injury responses in the ischemic border zone

Permalink

<https://escholarship.org/uc/item/4qb5q4gm>

Author

Taghdiri, Nika

Publication Date

2022

Peer reviewed|Thesis/dissertation

UNIVERSITY OF CALIFORNIA SAN DIEGO

Developments and applications of tools for studying injury responses in the ischemic border  
zone

A Dissertation submitted in partial satisfaction of the requirements  
for the degree Doctor of Philosophy

in  
Bioengineering

By  
Nika Taghdiri

Committee in charge:

Professor Kevin R. King, Chair  
Professor Ju Chen  
Professor Karen L. Chirstman  
Professor Adam J. Engler  
Professor Robert S. Ross

2022

Copyright

Nika Taghdiri, 2022

All rights reserved

The Dissertation of Nika Taghdiri is approved, and it is acceptable in quality and form for publication on microfilm and electronically.

University of California San Diego

2022

## **DEDICATION**

This work is wholeheartedly dedicated to my beloved family. A special feeling of gratitude to my parents, who supported the educations of myself and was an inspiration to my passion, science.

## **EPIGRAPH**

*Great things are done by a series of small things brought together.*

Vincent Van Gogh

# TABLE OF CONTENTS

DISSERTATION APPROVAL PAGE	iii
DEDICATION .....	iv
EPIGRAPH.....	v
TABLE OF CONTENTS.....	vi
LIST OF FIGURES.....	xi
LIST OF TABLES.....	xiii
LIST OF ABBREVIATIONS .....	xiv
ACKNOWLEDGEMENTS.....	xv
VITA.....	xvi
ABSTRACT OF THE DISSERTATION.....	xvii
CHAPTER 1: INTRODUCTION.....	3
CHAPTER 2: Transcriptomic single multi-omic tools to redefine border zone.. &investigate its cellular dynamics after myocardial infarction .....	9
.2.1 ABSTRACT: .....	9
2.2 INTRODUCTION:.....	9
2.3: RESULTS.....	10
2.3.1: Single cell transcriptomic classification of CMs after ischemic injury .....	10
2.3.2: Cardiomyocyte transcriptomes define spatially distinct borderzones BZ1 and BZ2	16
2.3.3: The border zone at single cell resolution .....	21
2.3.4: Non-myocytes of the border zone.....	25
2.4: DISCUSSION.....	40
2.5: METHODS.....	42
2.5.1: Animals.....	42

2.5.2.: Permanent ligation (MI).....	43
2.5.3: Immunohistochemistry .....	43
2.5.4: Single-nucleus RNA-seq.....	43
2.5.5: Quality control, normalization, and integration.....	45
2.5.6: Spatial Transcriptomics .....	45
2.5.7: Borderzone mapping strategy .....	46
2.5.8: Neighborhood analyses and spatial correlations.....	47
2.5.9: Pseudotime analysis.....	48
2.5.10: Motif enrichment analysis and gene ontology .....	48
2.5.11: Segmentation, Classification, and Quantification of FISH images .....	49
2.5.12: Human tissue collection.....	49
2.5.13: Statistics .....	50
2.5.14: Data availability statement.....	50
2.6.: ACKNOWLEDGMENT .....	50
 CHAPTER 3: Ischemic injury is not necessary and mechanical trauma is sufficient to elicit BZ biology .....	 51
3.1: ABSTRACT .....	51
3.2: INTRODUCTION .....	51
3.3: RESULTS.....	52
3.3.1: Onset and evolution of the transcriptional border zone .....	52
3.3.3: The transcriptional BZ in fine mechanical injury model invivo.....	58
3.3.4: Determination of hypoxia in fine mechanical injury .....	60
3.3.5: The transcriptional BZ in other mechanical injury model invivo.....	63
3.3.6: The transcriptional BZ in fine mechanical injury model invitro .....	63
3.4: DISCUSSION.....	64
3.5: METHODS.....	66

3.5.1: Animals.....	66
3.5.2.: Permanent ligation (MI).....	66
3.5.3: Transverse Aortic Constriction (TAC) and Isoproterenol treatment (ISO).....	66
3.5.4: Cardiac Needle Pass Injury (NP).....	67
3.5.5: Scratch Assay.....	67
3.5.6: Immunohistochemistry.....	68
3.5.7: Single-nucleus RNA-seq.....	68
3.5.8: Quality control, normalization, and integration.....	69
3.5.9: Spatial Transcriptomics.....	69
3.5.10: Determination of Regional Ischemia or Hypoxia.....	70
3.5.11: Spatial patterning of CM signatures.....	71
3.5.12: Statistics.....	71
3.6.: ACKNOWLEDGMENT.....	72
CHAPTER 4: Macrophage calcium reporter mice reveal immune cell communication <i>in vitro</i> and <i>in vivo</i> .....	73
4.1: ABSTRACT.....	73
4.2: INTRODUCTION.....	73
4.3: RESULTS.....	75
4.3.1: Immune calcium reporter mouse construction and characterization.....	75
4.3.2: Calcium dynamics of macrophage cell death induced by DNA sensing.....	76
4.3.3: Macrophage cell communication is induced by fatal DNA sensing.....	78
4.3.4: Inference of cell communication from $Csf1r^{Cre}GCaMP5^{fl}$ reporter dynamics <i>in vivo</i> .....	83
4.3.5: Excess synchrony: A metric for identifying cell communication events <i>in vivo</i> .....	86
4.3.6: Prediction of spatiotemporal cell communication and regulation in a tumor context <i>in vivo</i> .....	88
4.4: DISCUSSION.....	91

4.5: METHODS.....	93
4.5.1: Animals.....	93
4.5.2: Tissue processing.....	94
4.5.3: Flow cytometry .....	94
4.5.4: Cell culture.....	95
4.5.5: Time-lapse imaging of calcium reporter dynamics in vitro and in vivo.....	95
4.5.6: Quantitative analysis of epifluorescence imaging .....	96
4.5.7: Inference of Cell Communication from Calcium Reporter Time Lapse Imaging .....	96
4.5.8: Spatiotemporal Excess Synchrony pipeline details .....	97
4.5.9: Quantification and statistical analysis.....	97
4.5.10: Data and code availability.....	97
4.6.: ACKNOWLEDGMENT .....	98
CHAPTER 5: Inferring cell communication using single cell calcium spatiotemporal dynamics	99
5.1: ABSTRACT .....	99
5.2: INTRODUCTION.....	99
5.3: RESULTS.....	99
5.3.1 Preprocessing of fluorescence time-series image stacks collected from GECI reporter cells .....	99
5.3.2: Peak finding and impulse train determination from Ca <sup>2+</sup> GECI time series fluorescence .....	100
5.3.3: Inference of cell communication pipeline based on “Excess Synchrony” metric ...	101
5.4: DISCUSSION .....	105
5.5: DATA AND CODE AVAILABILITY.....	106
5.6: ACKNOWLEDGMENT .....	106
6. CONCLUSION.....	107

Supplementary Figure..... 110  
REFERENCES ..... 112

## LIST OF FIGURES

Figure 1. 1 Experimental model to redefine BZ.....	4
Figure 1. 2 Macrophage transgenic reporter to infer cell communication in vitro and in vivo .....	8
Figure 2. 1 CM transcriptional fingerprints after MI using single nuclei RNA seq after MI using single nuclei RNA seq.....	14
Figure 2. 2 CM transcripts redefine the ischemic borderzone using spatial transcriptomic.....	18
Figure 2. 3 Spatial transcriptomics of human STEMI tissue .....	21
Figure 2. 4 BZ2 CMs form a thin boundary between surviving and ischemic myocardium .....	23
Figure 2. 5 Cardiac immune niches after ischemic injury .....	27
Figure 2. 6 Activated fibroblasts localize with BZ2 CMs .....	33
Figure 3. 1 The transcriptional BZ emerges rapidly after ischemia .....	55
Figure 3. 2 Morphological features of the emerging borderzone .....	57
Figure 3. 3 Micro mechanical trauma is sufficient to elicit BZ biology.....	59
Figure 3. 4 Induction of BZ is independent of ischemia .....	61
Figure 3. 5 Induction of BZ in other mechanical injury model .....	63
Figure 3. 6 Induction of BZ in micro injury model invitro (NRVM).....	64
Figure 4. 1 Calcium reporter macrophages reveal the dynamics of fatal DNA-induced calcium overload	78
Figure 4. 2 Macrophage DNA sensing induces cell communication in vitro.....	81
Figure 4. 3 Csf1r-GCaMP5 reporter cell communication in vivo revealed by intravital imaging through a dorsal window chamber.....	84
Figure 4. 4 Characterization of spatiotemporally synchronous cells.....	88

Figure 4. 5 Quantification of excess synchrony and inference of communication in highly dynamic in vivo microenvironments .....90

Figure 5. 1 Diagram of cell communication pipeline inference steps .....103

Figure 5. 2 Example of how varying Sth affects predicted cell communication events .....104

Figure S. 1 Integration of single cell and nuclei RNA-seq heart datasets during acute responses to MI..110

## LIST OF TABLES

Table 2. 1 Top 10 genes significantly expressed in immune niches.....	28
Table 2. 2 Top 10 genes significantly expressed in stromal niches.....	36

## LIST OF ABBREVIATIONS

MI	Myocardial infarction
STEMI	Acute anterior ST elevation myocardial infarction
CM	Cardiomyocyte
snRNA-seq	Single nucleus RNA sequencing
scRNA-seq	Single cell RNA sequencing
m-FISH	Multiplex in situ hybridization
TAC	Transverse aortic constriction model
ISO	Isoproterenol iatrogenic model
LON	Loss of neighbor
NP	Needle pass injury model
NRVM	Neonatal rat ventricular myocyte
qPCR	Quantitative polymerase chain reaction
GECI	Genetically encoded calcium indicator
GFP	Green fluorescent protein

## ACKNOWLEDGEMENTS

I would like to thank my advisor and mentor, Professor Kevin King, who guided me and supported me throughout my PhD as my committee chair and my mentor. Without his guidance, I wouldn't be a critical thinker and a problem solver as I am today. I also thank my Dissertation committee for their valuable input in my research. I would like to thank Dr. Van K. Nih, without her guidance and help in my research, I would not be the scientist I am today. Further I would like to acknowledge the King Lab and Christman Lab, including Zhenxing Fu, David Calcagno, Avinash Toomu, and Josh Mesfin, current and past, for their help and friendship.

Chapter 2 &3 is adapted from Calcagno DM\*, **Taghdiri N\***, Ninh VK, Mesfin JM, Toomu A, Sehgal R, Lee J, Liang Y, Duran JM, Adler E, Christman KL, Zhang K, Sheikh F, Fu Z, King KR. Single cell and spatial transcriptomics of the infarcted heart define the dynamic onset of the border zone in response to mechanical destabilization. *Nature Cardiovascular research*. **2022** (accepted). The dissertation author was the Co first author of this paper.

Chapter 4 &5 is adapted from **Nika Taghdiri**, David M. Calcagno, Zhenxing Fu, Kenneth Huang, Rainer H. Kohler, Ralph Weissleder, Todd P. Coleman, and Kevin R. King. Macrophage calcium reporter mice reveal immune cell communication in vitro and in vivo. *Cell Methods Report*. **2021**, **Nika Taghdiri**, Kevin R. King. Inferring cell communication using single cell calcium spatiotemporal dynamics. *STAR protocol*. **2022**. The dissertation author was the primary author of these papers.

## VITA

2015 Bachelor of Science in Biomedical engineering major, Amir Kabir University of Technology (Tehran Polytechnic)

2022 Doctor of Philosophy in Bioengineering major, University of California San Diego

## PUBLICATIONS

**Nika Taghdiri**, David M. Calcagno, Zhenxing Fu, Kenneth Huang, Rainer H. Kohler, Ralph Weissleder, Todd P. Coleman, and Kevin R. King. Macrophage calcium reporter mice reveal immune cell communication in vitro and in vivo. *Cell Methods Report*. **2021**

David M. Calcagno\*, Angela Chu\*, Susanne Gaul, **Nika Taghdiri**, Avinash Toomu, Aleksandra Leszczynska, Benedikt Kaufmann, Bettina Papouchado, Alexander Wree, Lukas Geisler, Hal M. Hoffman, Ariel E. Feldstein, Kevin R. King. NOD-like receptor protein 3 activation causes spontaneous inflammation and fibrosis that mimics human NASH. *Hepatology*. **2022** (\*Co-first author)

**Nika Taghdiri**, Kevin R. King. Inferring cell communication using single cell calcium spatiotemporal dynamics. *STAR protocol*. **2022**

Calcagno DM\*, **Taghdiri N\***, Ninh VK, Mesfin JM, Toomu A, Sehgal R, Lee J, Liang Y, Duran JM, Adler E, Christman KL, Zhang K, Sheikh F, Fu Z, King KR. Single cell and spatial transcriptomics of the infarcted heart define the dynamic onset of the border zone in response to mechanical destabilization. *Nature Cardiovascular research*. **2022** (\*Co-first author, preprint)

**ABSTRACT OF THE DISSERTATION**

Developments and applications of tools for studying injury responses in the ischemic border  
zone

by

Nika Taghdiri

Doctor of Philosophy in Bioengineering

University of California San Diego, 2022

Professor Kevin R. King, Chair

Myocardial infarction (MI) is the leading cause of mortality and morbidity worldwide.<sup>1</sup> After MI a gradient of anatomical changes occur near a narrow band of fully perfused hypocontractile myocardium, borderzone (BZ), adjacent to frankly ischemic zone (IZ) including wall thinning, progressive ventricular dilation, rupture, and pathologic arrhythmias.<sup>2-4</sup> Studies show that the BZ microenvironment is impacted by immune niche cellular communication because of noninfectious cell death resulting from MI and has a potential regenerative niche.<sup>5-7</sup> However, the cellular and molecular mechanisms of surviving BZ and immune cellular communication in the context of BZ are not well understood. This is due to *first*, because efforts to dissect it inevitably include healthy perfused remote zone (RZ) and infarcted zone (IZ) in uncontrolled proportions and *second* investigating cellular communication conventional tools are spatially destructive with low temporal resolution and throughput<sup>8</sup>.

We developed methods for isolating single nuclei cardiomyocytes (CMs), performing unbiased high throughput single nuclei RNAseq (snRNAseq) and spatial transcriptomics to transcriptionally redefine BZ from RZ after adult mice were subjected to permanent ligation. We tested whether BZ and RZ exhibit distinct transcriptional signatures that can be revealed by unbiased clustering. To determine the spatial patterning of these CM subsets, we performed grid-based spatial transcriptomics (Visium 10x) and validated with multiplexed RNA fluorescence in situ hybridization (mFISH) to show that the BZ can be functionally defined by gene expression patterns. Then we assessed to determine the onset and evolution of the transcriptionally defined BZ on adult mice that are subjected to permanent ligation at various timepoints along with sham controls. We hypothesized that BZ dominantly is induced by mechanical instability, a ‘Loss of Neighbor’ theory. In order to test this hypothesis, we performed spatial transcriptomics on non-ischemia models including a fine needle pass trauma, Transverse aortic constriction model (TAC)

and isoproterenol iatrogenic model (ISO).

Finally, we developed a transgenic tool to provide a non-destructive assay with high temporal resolution for macrophage immune cells,  $Csf1r^{Cre}$  GCAMP5<sup>fl</sup> to investigate cell communication. Upon a stimuli *invitro* or *in vivo*, we attempted to discover the spatiotemporal correlation of intracellular calcium elevation in single cell resolution and infer cellular communication events using a computational pipeline called 'Excess synchrony'.

Overall, these applications and tools enhanced the ability to gain deeper understandings of biology and molecular mechanisms in myocardium tissue after MI.

## CHAPTER 1: INTRODUCTION

The most common cause of death worldwide, myocardial infarction (MI), occurs at an alarming rate of 1 every 25 seconds.<sup>9</sup> MI is the most common cause of heart failure with an estimated annual incidence of 605,000 new cases and 200,000 reinfarction events in the US alone, cumulating in over 8 million hospital admissions per year.<sup>10,11</sup> The annual cost of MI in the US alone is more than \$84.9 billion including direct medical care and lost productivity from morbidity and mortality.<sup>12</sup> This injury results from obstruction of coronary artery blood flow and leaves dependent cardiomyocytes ischemic due to a mismatch between oxygen supply and demand. In adults, cardiomyocyte (CM) proliferative potential is limited, and to date, no consequential cardiac regeneration has been demonstrated. Instead, therapeutic efforts have focused on protecting the surviving borderzone cardiomyocytes (BZ) in the region immediately adjacent to the necrotic myocytes in the ischemic zone (IZ). Anatomically, the topography of the IZ is irregular in shape, with surviving cardiomyocyte islands interdigitating with necrotic tissue and extending into the adjacent spared myocardium. The increase in CM cell size and reduction in capillary density is greater in the region bordering the IZ than in the relatively remote zone (RZ) cardiomyocytes. The borderzone is thought to be a biologically distinct region from the distant, well-perfused RZ; borderzone cardiomyocytes show hallmarks of dedifferentiation, sarcomere remodeling, and decreased mitochondrial volume in comparison with healthy CM's in the RZ. Yet, due to technological limitations, surprisingly little is known about the cellular and molecular biology that characterizes and creates the distinct BZ attributes. Specifically, conventional methods to understand the BZ derives from low resolution, whole organ functional imaging (e.g. MRI, echocardiograms), bulk analysis of manually dissected borderzone-containing myocardium, and

tissue section immunostaining, which require specific and validated antibodies to label proteins of interest.

With the advent of next generation sequencing, new high throughput methods and leveraging whole-genome spatial transcriptomics, we can now redefine functional characteristics of histologically well perfused post-infarcted myocardium borderzone and discover spatially heterogenous niches, containing substructure of BZ, immune and stromal niches (Figure 1.1).

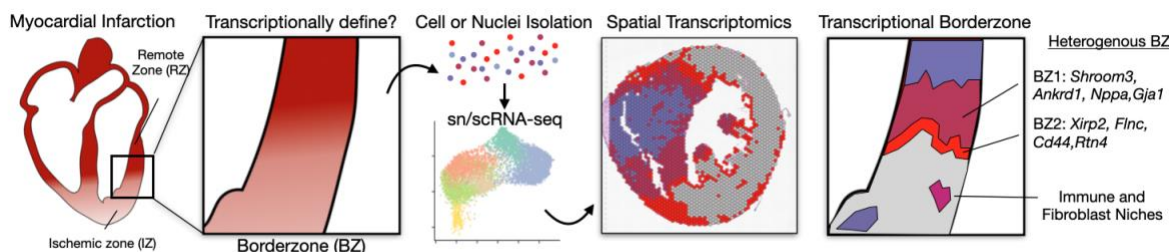


**Figure 1. 1 Experimental model to redefine BZ**

Scientific question and experimental design: to define the BZ transcriptionally, we performed snRNA-seq of mouse hearts without (no injury) and with ischemic injury, defined cell types based on unsupervised clustering and marker genes, and mapped the resulting transcriptomic signatures in space using spatial transcriptomics. We then validated our findings using multiplex RNA FISH (mFISH; Rebus, Biosystems).

Current therapeutics such as emergency reperfusion after MI are time critical to protect myocardium BZ. This suggests an importance of investigating the emergence and evolution BZ biology. In addition, there are no treatment options available to mitigate adverse remodeling in the surviving myocardium BZ after MI, which causes patients progress to heart failure with reduced ejection fraction characterized by dilated ventricular chamber and thinning myocardial walls. Therefore, discovering whether the dominant cause of BZ emergence transcriptionally is due to ischemia or not.

In Chapter 3, we perform snRNAseq and spatial transcriptomics on adult mice that are subjected to permanent ligation at various timepoints along with sham controls to discover the onset and evolution of borderzone. Then we ask whether the emergence of BZ is due to ischemia or mechanical instability. We answer this question by performing spatial transcriptomics on non-ischemic fine-needle-trauma and other mechanical injury model such as Transverse aortic constriction model (TAC) and isoproterenol iatrogenic model (ISO) and compared with MI model.

Moreover, MI is fundamentally a noninfectious cell death process; this sterile injury releases intracellular contents of cardiomyocytes collectively known as alarmins or damage associated molecular patterns (DAMPs).<sup>13,14</sup> DAMPs are sensed by genome-encoded pattern recognition receptors (PRRs) expressed by professional immune and amateur non-immune cells that are collectively referred to as stromal cells.<sup>15</sup> A maladaptive Interferon regulatory factor 3 (IRF3) dependent innate immune response and type I interferon (IFN), a master regulator of the antiviral response, are activated by DAMPs after MI. In addition, the interruption of IRF3-dependent signaling results in decreased cardiac expression of inflammatory cytokines and chemokines of the heart, higher survival rate and overall improved cardiac function suggesting that DAMPs provokes infarct phagocytes and immune infiltration. This event emphasizes the significance of immune niches influence on BZ.<sup>16</sup>

Recently it has been appreciated that the myocardium contains resident immune macrophages derived from different developmental lineages; more importantly, there are heterogenous resident macrophages that appear to differentially regulate the healing process post-infarct. Bone marrow derived monocytes, a classic innate immune cell, infiltrate the myocardium in the days following infarct, and interact with the cues and regulation from resident macrophages,

where they receive molecular instructions to undergo polarization. Based on the messages they receive upon arrival in the infarcted heart, they may contribute to optimal healing or promote pathophysiological remodeling in the microenvironment of the *borderzone*. Investigating macrophage dynamics are promising since *acutely*, their functions impact myocardial tissue over the days and weeks following MI and *chronically* they form cellular networks and alter the BZ microenvironment via cell-cell communication with myocytes to influence cardiac conduction and function <sup>7</sup>. Nevertheless, existing methods for visualizing and interrogating the cellular crosstalk between macrophages and resident cardiac cells are limited to coculture systems with transwells or Boyden chambers, fluorescence recovery after photobleaching (FRAP) imaging, or measurement of electrical conductance via patch clamping. These methods are spatially destructive with low temporal resolution and throughput <sup>8</sup>.

For the chapter 4& 5, we developed a transgenic tool to provide a non-destructive assay that infer cell communication with high temporal resolution. We leveraged high resolution imaging with a using tissue-specific genetically encoded calcium indicator (GECI) mice reporter (GCAMP5<sup>fl</sup>) animal in which is calcium dependent green-fluorescence protein (GFP) specifically in (Csf1r<sup>Cre</sup>) macrophages. Calcium represents an attractive indicator of cell communication in cells because it is a dynamic second messenger influenced by multiple signaling pathways. In non-communicating populations of cells, calcium dynamics are not necessarily correlated. We reasoned that non-destructive monitoring of calcium dynamics in a population of cells and detection of their spatiotemporal correlations could be used to infer cell communication, even if the molecular stimuli, mediators, and mechanisms were unknown. In this study we use cytosolic double-stranded DNA (dsDNA), as a freely diffusible innate immune stimuli *in vitro*. We reasoned to choose dsDNA since it is an endogenous DAMPs that activates IRF3 via the adaptor STING and GMP-

AMP synthase (cGAS) pathway and influences BZ niches caused by immune dynamics.<sup>16</sup> We also take an advantage of intravital microscopy techniques and detect spatiotemporal correlation of their calcium dynamics in a dorsal window chamber reporter model *in vivo* by stimulating with tumor-associated cell lines. In order to infer cell communication, we create a computational pipeline called ‘Excess Synchrony’ which automatically preprocess GECI fluorescence time-series measured by time-lapse imaging or intravital microscopy, detect peaks with single cell resolution, and infer cell communication from the synchrony of single cell calcium transients (Figure 1.2).

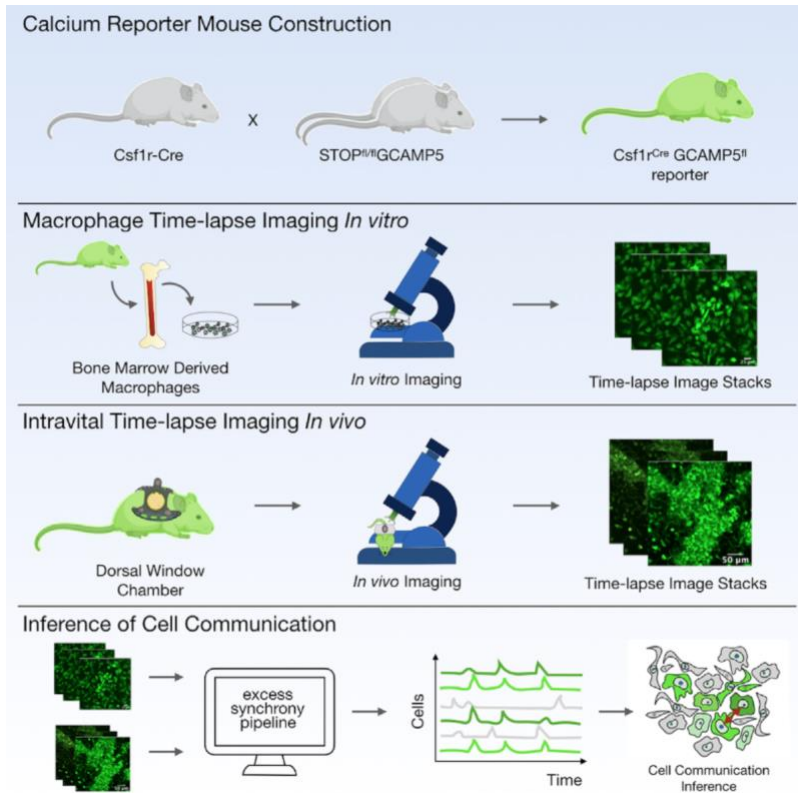


**Figure 1. 2 Macrophage transgenic reporter to infer cell communication in vitro and in vivo**

Constructing nondestructive, genetically encoded calcium indicator (GECI) reporter mice using the cre-lox transgenic system to specifically track macrophage-dependent calcium dynamics. We bred GCAMP5<sup>fl</sup> mice with Csf1r<sup>Cre</sup> to generate the calcium reporter mice specifically in macrophages. After harvesting bone marrow, bone marrow derived cells are differentiated into macrophages, which were then treated with double stranded DNA(dsDNA) and imaged *in vitro*. *In vivo* intercellular calcium dynamics were measured using high resolution imaging by implanting MC38-H2B mCherry cells, a murine colon adenocarcinoma cell line, into Csf1r<sup>Cre</sup> GCAMP5<sup>fl</sup> reporter mice. The intercellular calcium dynamics were visualized by leveraging the dorsal window chamber. Cell-cell communication was then inferred using a pipeline called ‘Excess synchrony’ based on calcium dynamics.

## **CHAPTER 2: Transcriptomic single multi-omic tools to redefine border zone.. &investigate its cellular dynamics after myocardial infarction**

### **.2.1 ABSTRACT:**

The ischemic borderzone (BZ) is a geographically complex and biologically enigmatic interface separating poorly perfused ischemic zones (IZ) from comparatively healthy remote zones (RZ). BZ cellular and molecular mechanisms are not well understood because efforts to dissect it inevitably include RZ and IZ in uncontrolled proportions. Here, we use single-cell/nuclei RNA-sequencing, spatial transcriptomics, and multiplexed RNA fluorescence in situ hybridization (m-FISH) to identify BZ cardiomyocytes (CMs) subsets. BZ1 (Nppa+Xirp2--) forms a hundreds-of-microns-thick transitional layer adjacent to RZ, while BZ2 (Nppa+Xirp2+) forms a tens-of-microns-thick layer at the IZ edge. BZ2 CMs have reduced CM cell contact; colocalize with matricellular-protein-expressing myofibroblasts; and upregulate focal adhesion-, sarcomere-, and cytoskeletal-genes.

### **2.2 INTRODUCTION:**

The ischemic borderzone (BZ) is a geographically complex and biologically enigmatic area of the infarcted heart that separates regions of cell death (the ischemic zone, IZ) from comparatively normal myocardium (the remote zone, RZ) <sup>17-19</sup>. It has been implicated in processes such as infarct expansion, ventricular remodeling, and arrhythmia origination, as well as cardiomyocyte proliferation and regeneration <sup>18,20-27</sup>. Zones are often recognized histologically based on the appearance of cardiomyocytes (CMs). For example, at early time points after MI, dying CMs in the IZ exhibit characteristic wavy appearances with intracellular contraction bands that progress to necrosis <sup>28</sup>. Meanwhile, surviving BZ CMs retain relatively normal cellular morphology but are thought to be functionally distinguishable from RZ CMs based on

hypocontractility despite preserved perfusion <sup>4</sup>. Over time, the BZ is thought to evolve, expand, and remodel, leading to macroscopic ventricular dilation, wall thinning, and even rupture <sup>24,29,30</sup>. This manifest clinically as progressive symptomatic heart failure experienced by patients. Despite the growing armamentarium of pharmacologic therapies aimed at limiting adverse ventricular remodeling, ischemic heart disease remains the most common cause of death in the world <sup>31,32</sup>.

The determinants of the BZ remain largely unknown because the territory is challenging to isolate and study at a cellular and molecular level. Historically, the BZ was anatomically defined, but it could not be easily microdissected without including uncontrolled proportions of IZ and RZ. The inability to isolate BZ tissue with microscopic precision prevented its investigation using unbiased multi-omic assays. However, recent developments in single cell and spatial transcriptomic technologies are resolving biological processes in complex cardiac tissues with unprecedented detail and without the need for mechanical microdissection <sup>16,19,33-45</sup>. Here, we leverage single cell and single nuclei transcriptomics (scRNA-seq, snRNA-seq), grid-based spatial transcriptomics, and multiplexed RNA fluorescence in situ hybridization (mFISH) to show that the BZ can be functionally defined by gene expression patterns. Our data show that BZ CMs can be categorized into two major subgroups (BZ1 and BZ2) with distinct spatial and functional characteristics, each containing additional substructure and immune and stromal context. BZ1 forms a hundreds-of-microns-thick transitional layer adjacent to the RZ, while BZ2 is a tens-of-microns-thin layer that decorates the complex boundaries of the IZ.

## **2.3: RESULTS**

### **2.3.1: Single cell transcriptomic classification of CMs after ischemic injury**

To test whether the infarcted heart BZ can be functionally defined by “transcriptional microdissection”, we subjected adult mice to left anterior descending coronary artery ligation and

harvested hearts at various timepoints along with sham controls and isolated single cells and nuclei (no injury; n = 3, 31580 sc/sn), 24hrs (n =6, 33,336), 72hrs (n =3, 10380 sc/sn) for sc/snRNA-seq (Figure S.1b,d). We collected myocardial tissue extending from the non-infarcted to the infarcted myocardium to ensure comprehensive capture of BZ biology. The resulting counts matrices were integrated with previously published whole single cell RNA-seq (scRNA-seq) dataset collected at similar timepoints after MI to create a unified sc/snRNA-seq object with clusters representing cardiomyocytes (CMs), fibroblasts (Fibs), endothelial cells (ECs), smooth-muscle cells (SMCs), neutrophils (Neuts), dendritic cells (DCs), monocytes (Mono), and macrophages (Macs) (Figure S.1d). Most cell types were represented in both whole cell and nuclei data; however, CMs, which are large and difficult to isolate as intact cells, were exclusively represented as nuclei, whereas neutrophils, which have fragile polymorphic nuclei, were primarily represented in whole cell samples (Figure S.1 f g, h,i). From these data, we generated subset-specific gene signatures or scores (Figure S.1a-c).

In parallel, we performed spatial transcriptomics (Visium, 10X Genomics) on short-axis sections of hearts from mice subjected to: (i) sham surgery or (ii) experimental MIs harvested at 72hrs, and 168hrs post-MI. In total, we analyzed the transcriptomes of 75,297 single nuclei and cells across 9 samples, and 17,802 pixels across 8 spatial transcriptomic samples (Figure S.1d). To quantify the spatial distribution of cell subsets, we integrated spatial transcriptomic data and performed clustering analysis to first understand the native structure of the transcriptomes across space before superimposed sn/scRNA-seq derived subset-specific scores to infer pixel composition, spatial patterning and colocalization, which were then validated by probe-based m-FISH (see mapping strategy in methods for more detail; Figure S.1 a).

We began by analyzing CMs transcripts since they are the predominant cell type most used to morphologically recognize the BZ in histological sections (Figure 2.4). Within the integrated dataset, CM transcriptomes formed a distinct cluster characterized by elevated expression of cardiac-specific genes such as *Tnnt2* (encoding for protein troponin T) and *Ckm* (encoding for protein creatine kinase M) (Figure 2.2a bottom, Figure S.1e). Subclustering the CMs revealed a continuum of five distinct yet overlapping transcriptional states (CM1-CM5) suggestive of a regulated multi-step progression (Figure 2.1 a, left, c, d). Gene ontology and motif enrichment analysis was performed to infer functional and putative regulatory programs<sup>46</sup>. Based on cluster composition changes after injury, gene dynamics, and spatial distribution, clusters were collapsed into three major functional groups (RZ, purple; BZ1, maroon; BZ2, red; Figure 2.1, right) as described below.

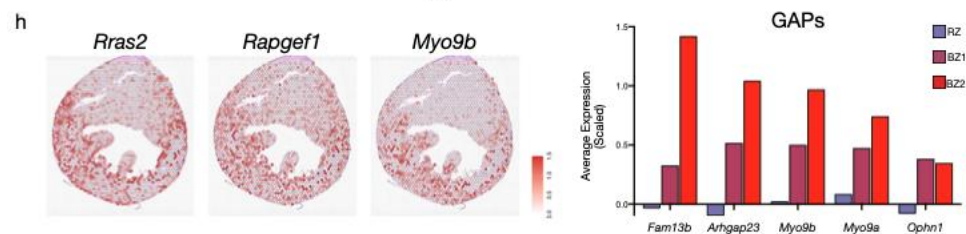
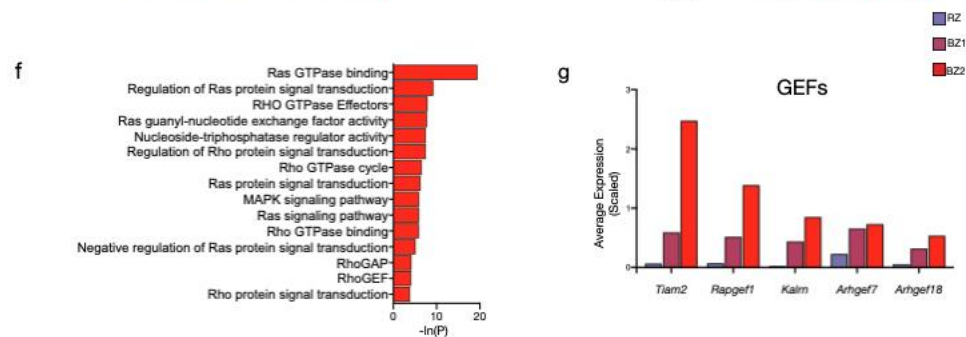
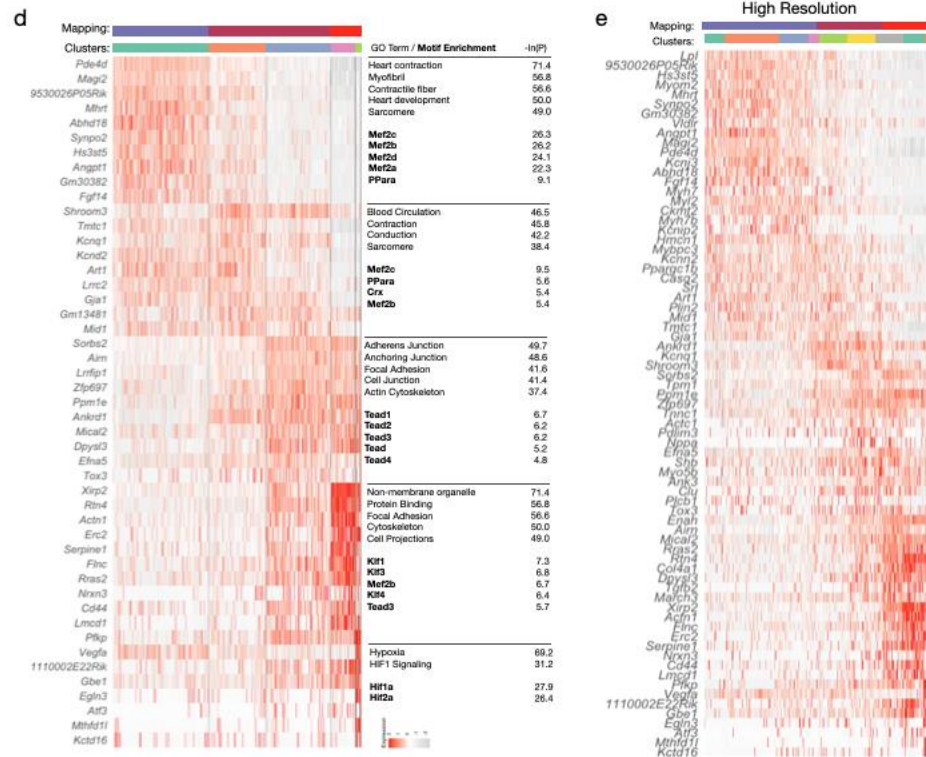
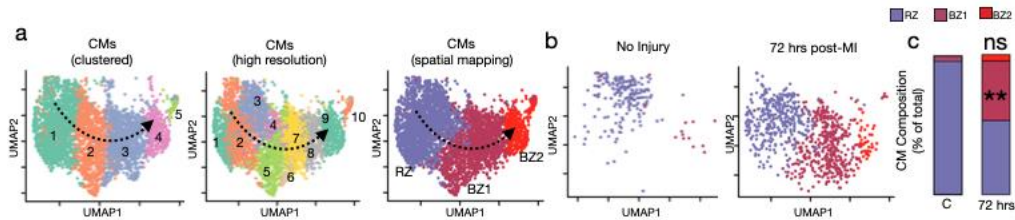
To identify RZ CMs, CM subsets from infarcted hearts that co-clustered with CMs from non-infarcted hearts were assessed. Within the integrated data, almost all CMs from non-infarcted hearts co-clustered with CM1 from infarcted hearts. These cells were characterized by elevated levels of myosin heavy chain 6 (*Myh6*) and other markers of cardiac homeostasis (Figure 2.1b, c, d). In contrast, cells from clusters 2/3 and 4/5, were minimally present in control samples (4.6% and N.D.) yet represented  $42.6 \pm 6.9\%$  and  $4.6 \pm 2.6\%$  of CMs on 72hrs post-MI, respectively, suggesting they were unique to the post-infarct heart and candidate BZ CMs (Figure 2.1 c; mean  $\pm$  SEM).

CM4 and CM5 were defined by elevated expression of Xin actin-binding repeat containing 2 (*Xirp2*; aka *Cmya3*, *mXin $\beta$* , *Myomaxin*), filamin C (*Flnc*), and desmin (*Des*)<sup>47-50</sup>. *Xirp2* is an actin- and  $\alpha$ actinin- binding protein which localizes to Z-disc regions and intercalated discs to maintain structural integrity and conduction<sup>51,52</sup>. Similarly, *Flnc* is an actin binding

protein critical to costamere structure; mutations in Flnc are associated with hypertrophic and inherited dilated cardiomyopathies and sudden cardiac death<sup>53-57</sup>. To understand the functional significance of this cluster, gene ontology enrichment analysis was performed and revealed an impact on mechanical instability. We found enrichment for genes related to cytoskeletal binding, cell projections, and focal adhesions as well as enrichment for Ras and Rho GTPase signaling (Figure 2.1f,g,h) which regulate cytoskeletal dynamics and cellular replication, respectively. CM5s, which formed a distinct island in UMAP space, are a specialized subset of CM4 defined by elevated levels of HIF-regulated genes (e.g., Vegfa, Egl3) (Figure 2.1d). This cluster likely represented actively ischemic CMs. The absence of HIF-dependent gene expression in other subsets suggested that these regions were well-perfused.

**Figure 2. 1 CM transcriptional fingerprints after MI using single nuclei RNA seq after MI using single nuclei RNA seq**

(a) UMAP plots of clustered CMs with coarse resolution clustering (left), high resolution clustering (middle), and annotated clustering (right) based on spatial mapping and gene patterns. Representative data shown from control, 24hrs post-MI and 72 hrs post-MI samples (n=3 mice). (b) UMAP plots of CMs split by condition. (c) Quantification of CM composition by time after injury. (d) Heatmap displaying DEGs as determined by clustering with color bars above indicating cell ownership based on the annotation method. Gene ontology and motif enrichment terms are displayed to the right of each respective group. (e) Heatmap of resulting DEGs based on high resolution. (f) Select gene ontology terms enriched in BZ2 CMs related to Ras/Rho signaling. (g) Average scaled expression of guanine nucleotide exchange factors (GEFs) and GTPase activating proteins (GAPs) in CM subsets. (h) Spatial feature plots of representative Ras/Rho related genes showing distribution in BZ.



A notable characteristic of CM4/5s was the downregulation of CM1 genes including *Mhrt*, a long non-coding RNA that is downregulated in heart failure and *Myh6*, the predominate myosin heavy chain isoform of adult CMs <sup>27</sup>. Motif enrichment analysis showed that CM1s were enriched for Mef2 binding sites while clusters 4/5 were enriched for binding sites associated with several kruppel like factors, in agreement with a recent report demonstrating transition from Mef2 binding in CMs after injury (Figure 2.1 d) <sup>19,58</sup>.

Between CM1 and CM4/5 were transitional cardiomyocyte clusters CM2-3. CM2/3 expressed Ankyrin repeat domain 1 (*Ankrd1*; aka *Carp*), Shroom family member 3 (*Shroom3*), and natriuretic peptide A (*Nppa*; aka ANP, PND, Atrial Natriuretic factor prohormone). *Nppa* and *Ankrd1* were recently identified in infarct BZs using single gene in situ hybridization (ISH) <sup>19</sup>. *Ankrd1* is often considered a YAP regulated gene involved in mechanotransduction and proliferation during development and cancer <sup>59</sup>. Interestingly, both CM2/3 and CM4/5 were enriched for TEAD binding sites, which is the DNA binding partner involved in mediating YAP/TAZ signaling (Figure 2.1d). These CMs also expressed *Shroom3*, which is regulated by *Pitx2*, a necessary component for neonatal regeneration in Hippo-deficient mice <sup>60</sup>. Further, they expressed genes that encode proteins involved in cardiac conduction including *Cx43* (*Gja1*), *Scn5a*, and *Ryr2* that are collectively regulated by *Tbx5* and *Pitx2* <sup>61</sup>. Additionally, the natriuretic peptides, *Nppa* and *Nppb*, which are clinical biomarkers of heart failure and activated by CM stretch, suggest that this population is under mechanical stress <sup>62</sup>.

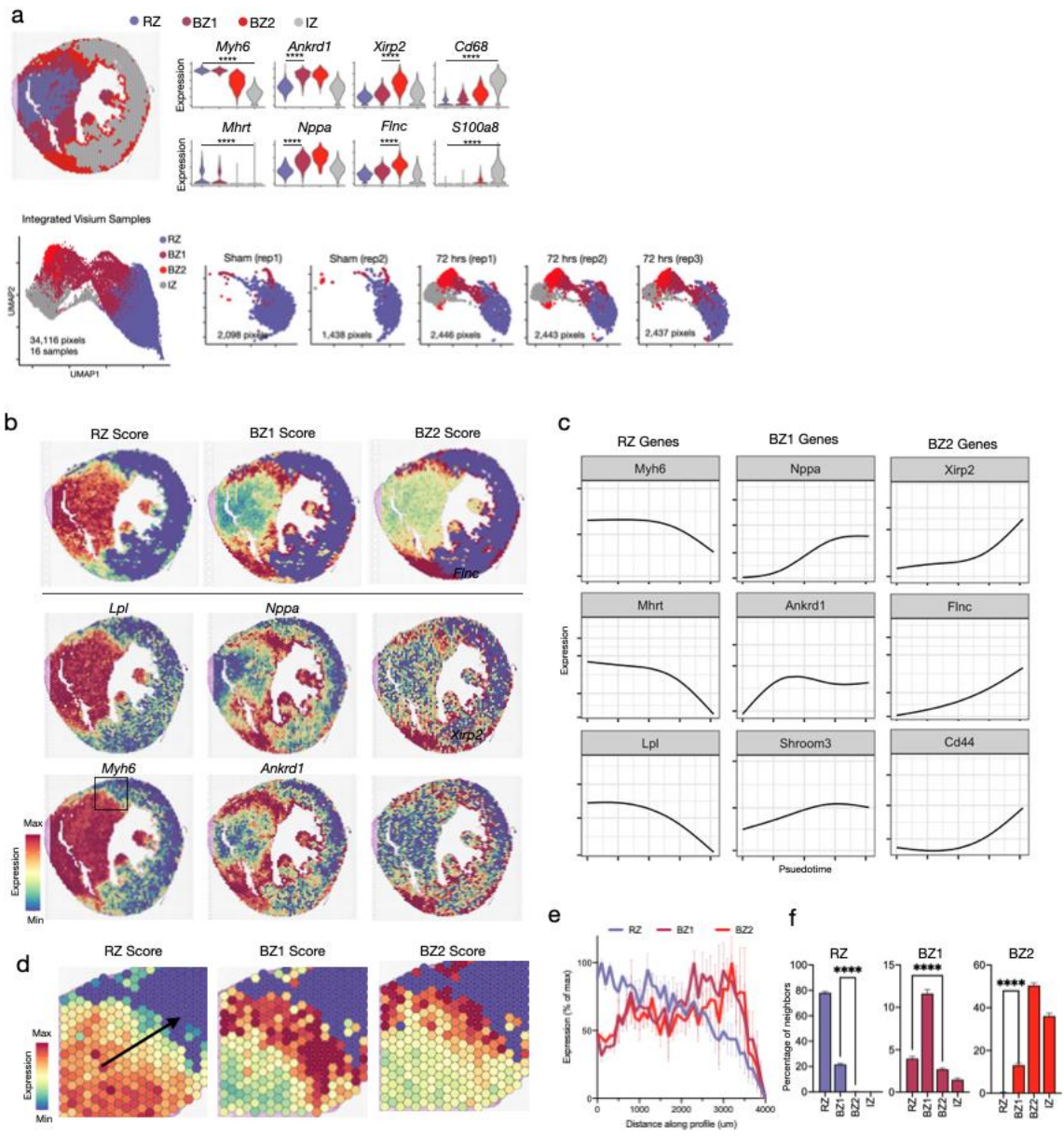
### **2.3.2: Cardiomyocyte transcriptomes define spatially distinct borderzones BZ1 and BZ2**

Since CM1s represented transcriptionally normal RZ myocytes and because IZ myocytes are, by definition, dead, we hypothesized that CM2/3 and CM4/5 may represent transcriptionally distinct areas of the BZ. To test this, we first performed clustering analysis on spatial data and

mapped snRNA-seq derived CM signatures (Figure 2.2a bottom). We found that differentially expressed genes (DEGs) discriminating CM2/3 and CM4/5 appeared in distinct contiguous locations in space, which we named BZ1 and BZ2, respectively (Figure 2.2b). To quantify these groups, we constructed genes scores by summing the top 10 DEGs derived from snRNA-seq data. Then to define spatial transcriptomic clusters as RZ, BZ1, BZ2, or IZ, we applied gene-set scores in a series of hierarchical classifiers. As predicted by snRNA-seq data, RZ scores were most elevated near the septum in regions distal to the infarct and slowly decreased in magnitude in regions that approached the infarct area; BZ1 CMs formed contiguous regions hundreds-of-microns in thickness, which associated with RZ and BZ2 CMs; and BZ2 CMs formed relatively smaller contiguous regions that directly neighbored the IZ and BZ1 CMs (Figure 2.2b). This patterning was consistently observed across replicates (Figure 2.4e, g). We performed trajectory analysis (Monocle) on snRNA-seq data and found that line profiles in space spanning from healthy to frankly infarcted regions had gene patterns that mirrored these results (Figure 2.2c, d, e, f). RZ genes (*Myh6*, *Mhrt*, *Lpl*) slowly decreased in magnitude as BZ1 genes (*Nppa*, *Ankrd1*, *Shroom3*) and BZ2 genes (*Xirp2*, *Flnc*, *Cd44*) were sequentially activated. Further, quantification of neighboring pixels confirmed that CM subsets most commonly neighbor CMs as predicted by snRNA-seq derived trajectory analysis.

## Figure 2. 2 CM transcripts redefine the ischemic borderzone using spatial transcriptomic

(a) Representative spatial transcriptomic data of mouse heart harvest after ischemic injury (Visium, 10X Genomics), clustered independent of snRNA-seq data as part of integrated spatial transcriptomic dataset (top). UMAP plot of integrated dataset composed of 34,116 pixels in 16 samples. Clusters were clustered and annotated based on DEG expression to identify RZ, BZ1, BZ2 and IZ pixels, and UMAP plots split by sample and replicates. (bottom) (b) Gene-set scores in space derived from snRNA-seq data with example genes shown below. (c) Trajectory analysis of snRNA-seq data with direction of pseudotime indicated in (Figure 2.1a). (d) Gene-set scores in space at BZ from box indicated in (b). (e) Gene-set scores as a function of space from RZ towards IZ as indicated by arrow in (d). (f) Quantification of neighboring pixels, split by mapping classification (mean  $\pm$  S.E.M.; statistics based on comparison to respective zone). \*\*\*\* P-value < .0001, Mann-Whitney Test. CM, cardiomyocytes; RZ, remote zone; BZ, borderzone; IZ, ischemic zone.



To test the relevance of this model to humans, we performed spatial transcriptomics on an ischemic human heart sample. The patient was a 45 year-old male who presented with an acute anterior ST elevation myocardial infarction (STEMI) and underwent PCI to the infarct-related left anterior descending artery, but despite successful revascularization he remained in refractory cardiogenic shock dependent on inotrope infusion. He underwent implantation of a left ventricular assist device 7 weeks after his initial STEMI, during which a core biopsy of ventricular myocardium was collected from the LV apex and processed for Visium spatial transcriptomics. We observed a similar distribution of BZ1- and BZ2-associated genes in humans compared to mice. However, because the sample was collected from a large ischemic zone, we found no clear evidence of RZ CMs in the region sampled (Figure 2.3). Taken together, these data show that after ischemic injury, CM transcriptomes form a continuous trajectory corresponding to spatial position within IBZ, thus validating the “transcriptional microdissection” method.

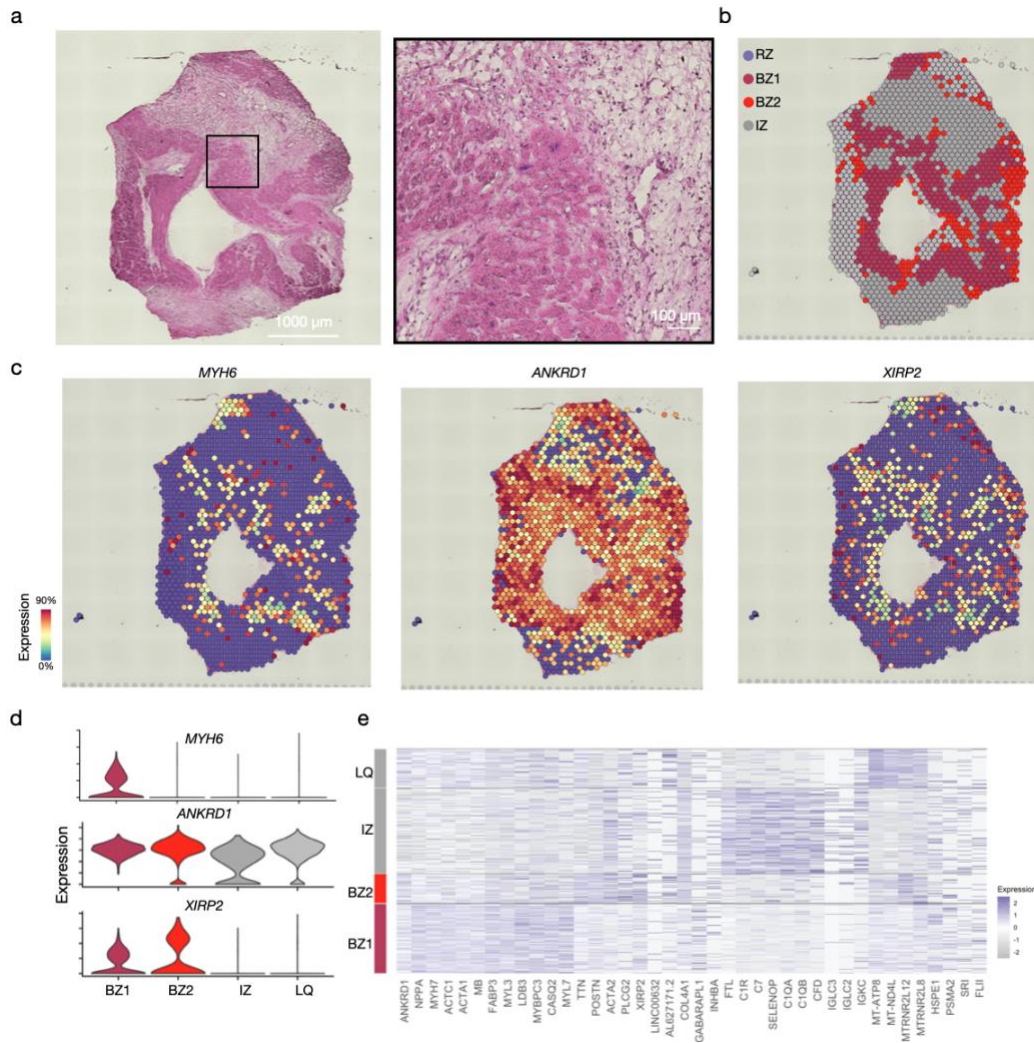


**Figure 2.3 Spatial transcriptomics of human STEMI tissue**

(a) H&E of cross section of human heart sample from patient presenting with LAD STEMI. (b) Spatial transcriptomic clustering results based on DEG analysis and assessment of BZ marker genes shown in space in (c) and by violin plots in (d). (e) Heatmap of cluster defining DEGs.

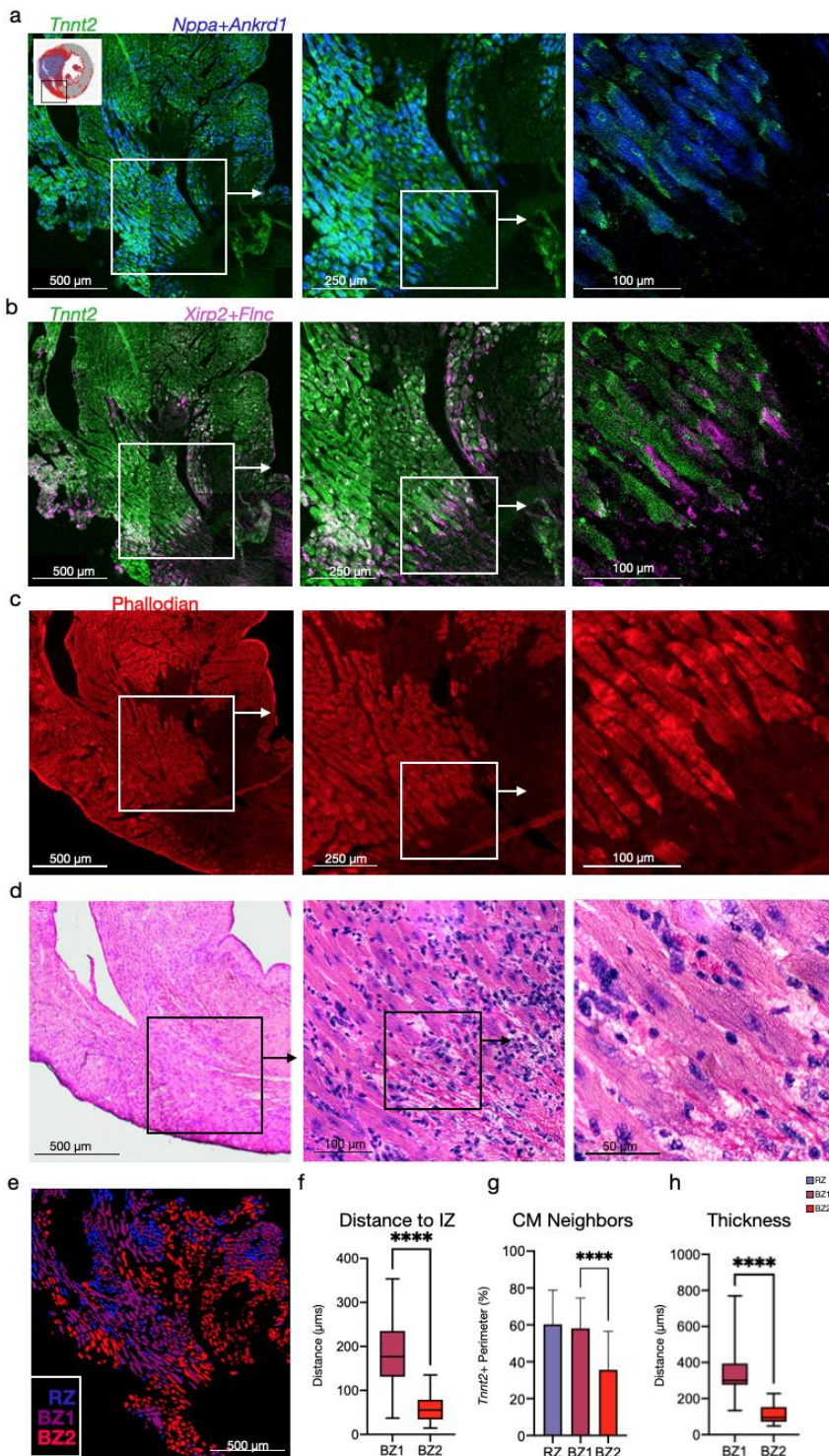
### 2.3.3: The border zone at single cell resolution

The spatial transcriptomics method is based on spatially-barcoded capture slides and next generation sequencing, which enables unbiased transcriptional profiling, but lacks single cell resolution because RNA capture sites are 55 μm diameter with 100 μm spacing. To achieve single cell spatial resolution, we performed multiplexed RNA fluorescence in situ hybridization (mFISH) using image cycling of barcoded probes for selected BZ transcripts (Rebus Biosystems) on

adjacent tissue sections. Consistent with the experiments above, CM1 probes (*Tnnt2*, *Myh6*) localized to RZ, CM2/3 probes (*Ankrd1*, *Nppa*) to BZ1, and CM4/5 probes (*Xirp2*, *Flnc*) to BZ2 (Figure 2.4a, b). However, interestingly, BZ2 was only several cell-lengths deep, as if the transcriptional signature was unique to cells at edge of the IZ. *Xirp2*- and/or *Flnc*-expressing cells decorated the complicated boundaries separating myocyte-free IZ from the much larger BZ1 (several hundred microns). Morphologic inspection of H&E and Phalloidin/WGA-stained sections showed BZ2 myocytes to be elongated and distorted cells that appeared to drip off the BZ ‘shore’ (Figure 2.4c, d). In addition to the surviving myocardial ‘shore’, we observed many isolated ‘islands’ of surviving myocytes within the IZ, and they also appeared as a core of BZ1 myocytes decorated by a boundary of *Xirp2*- and *Flnc*-expressing BZ2 myocytes (Figure 2.4a-d). To quantitatively confirm the spatial arrangement of RZ, BZ1, and BZ2 myocytes, we re-stained the mFISH-probed sections with WGA to label cell membranes and we performed cell segmentation and classification based on expression of *Nppa*, *Clu* (BZ1), *Xirp2*, *Flnc* (BZ2), and *Tnnt2* (RZ) (Figure 2.4e). Quantification of neighboring cell types confirmed that CM subsets most commonly contacted CMs from the same subset followed by the adjacent CMs predicted by trajectory analysis; that distance to the IZ was smallest for BZ2 CMs and largest for RZ CMs (Figure 2.4f) that BZ2 CMs had significantly fewer myocyte neighbors than BZ1 or RZ CMs (Figure 2.4g); and that BZ2 had a much smaller average contiguous thickness of  $109.9 \pm 50.0$   $\mu\text{m}$  compared to  $348.1 \pm 180.7$   $\mu\text{m}$  BZ1 (mean  $\pm$  S.D.) (Figure 2.4h). Taken together, these data suggest that the transcriptional progression from BZ1 to BZ2 occurs primarily at a single cell border with IZ.

**Figure 2. 4 BZ2 CMs form a thin boundary between surviving and ischemic myocardium**

(**a, b**) mFISH images of serial section from Figure. 2.3a (inset shown); (**a**) Blue, RZ marker, Tnnt2; Red, BZ1 markers, Nppa and Ankrd1; (**b**) Blue, RZ marker, Tnnt2; Green, BZ2 markers, Xirp2 and Flnc. (**c**) H&E images of serial section. (**d**) Phalloidin stained serial section. (**e**) CM classification based on WGA staining and mFISH data for quantification in f-g. (**f**) Quantification of nearest distance to IZ based. (**g**) Quantification of contacting CM neighbors. (**h**) Quantification of contiguous thickness. \*\*\*\* P-value < .0001, Mann-Whitney Test.



### 2.3.4: Non-myocytes of the border zone

MI results in the recruitment of millions of leukocytes into the IZ from hematopoietic reservoirs. Monocytes, monocyte-derived macrophages, and, to a lesser extent, neutrophils have received considerable attention as potential treatment targets for MI, yet more precise therapeutics are required<sup>63</sup>. Recent advancements in unbiased profiling have revealed heterogeneity in this compartment; however, their relationship to the newly defined BZ is unknown. Therefore, we mapped myeloid subpopulations in space after MI.

We classified immune subpopulations by subclustering *Ptprc*<sup>HI</sup> (encoding Cd45) cells (Figure 2.5a). In agreement with previous reports, this revealed several myeloid subsets including resident Macs (*Lyve1*<sup>HI</sup>), monocyte-derived Macs (*Ly6c2*<sup>HI</sup>, *Ifit1*<sup>HI</sup>, *Arg1*<sup>HI</sup>, *C1qa*<sup>HI</sup>, *Gclm*<sup>HI</sup>, *H2.Aa*<sup>HI</sup>, Rep), DCs (*Cd209a*<sup>HI</sup>) and Neuts subsets (*Retnlg*<sup>HI</sup>, *Siglec*<sup>HI</sup>, *Ifit1*<sup>HI</sup>) (Figure 2.5 a,b). To determine their spatial location, we first analyzed spatial transcriptomic data independent of snRNA-seq to understand its underlying structure by subsetting and clustering non-CM pixels, focusing on 72 hrs post-MI and 168 hrs post-MI (D7) when immune populations are known to be dynamic (Figure 2.5c). This revealed four spatially distinct ischemic zones (IZ1-4; Figure 2.5c). Cluster-defining DEGs suggested that each niche was composed of multiple underlying cell types, which is expected given the multicellular spatial resolution (Figure 2.5d, left). Therefore, we applied subset-specific scores to infer contributing cell types (Figure 2.5d, right). Overall, we found excellent reproducibility across replicates both in the abundance and spatial distribution of zones. IZ1 represented acellular regions as it had very few DEGs and showed no evidence of any immune signatures and minimal CM signatures. IZ2 was predominately composed of *Ly6c2*<sup>HI</sup> Monos and several macrophage subpopulations (*C1qa*<sup>HI</sup>, *Gclm*<sup>HI</sup>, *Lyve1*<sup>HI</sup>) and consistently formed along the posterolateral left ventricular wall near the papillary muscle (Figure 2.5e,f; top row). As

expected given the known flux of monocytes and macrophages at D4-D7 post-MI, IZ2 represented  $18.5 \pm 4.7\%$  of IZ pixels at 72 hrs post-MI, and  $37.7 \pm 1.4\%$  at 168 hrs post-MI (Figure 2.5h). *Arg1<sup>HI</sup>* Macs, which are thought to resolve inflammation, were a dominate signature in IZ3 in the anterior and anterolateral left ventricular wall, which is the territory supplied by the occluded LAD coronary artery (Figure 2.5e,f; middle row). The region was heavily fibrotic and contained abundant markers of Neuts (*S100a8*, *S100a9*). IZ3 pixels declined from  $17.8 \pm 5.7\%$  of IZ pixels at 72 hrs post-MI to  $6.13 \pm 3\%$  at 168 hrs post-MI, perhaps driven by the decline in infiltrating neutrophils (Figure 2.5 h). Spatial correlation analyses confirmed the colocalization of subset specific marker genes in space.

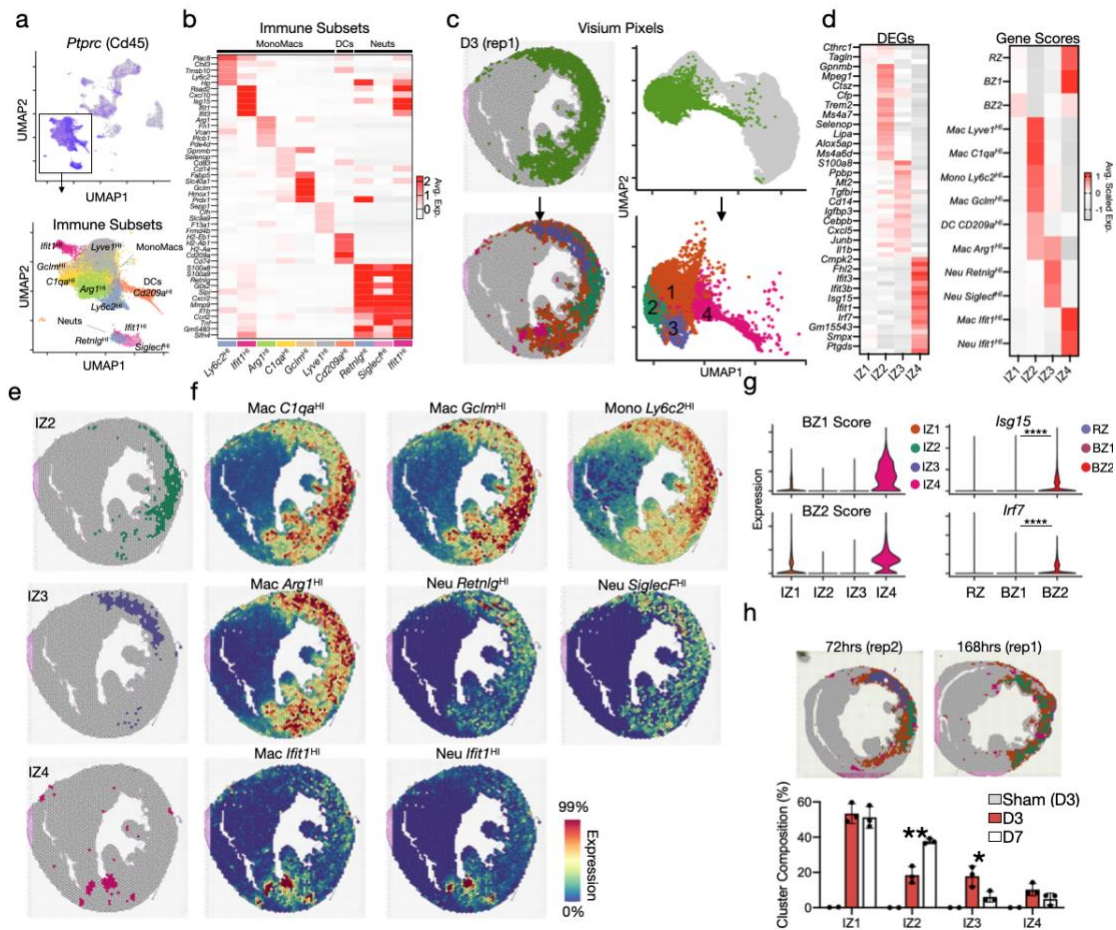


**Figure 2. 5 Cardiac immune niches after ischemic injury**

(a) Top: feature plot of *Ptprc* (Cd45) of integrated sc/snRNA-seq data Bottom: subset and reclustered monocytes, macrophages, and neutrophils. (b) Heatmap of average, scaled expression of cluster defining DEGs in (a). (c) Clustering results of IZ spatial transcripts derived from integrated spatial dataset including sham, 72hrs (D3) post-MI, and 168hrs (D7) post-MI samples with biological replicates and number of pixels annotated. Clusters are color coded in space (left) and in UMAP plots (right) as part of full dataset (top) and subset (bottom). (d) Heatmap of cluster defining DEGs (left) with gene-set scores derived from (b) superimposed (right). (e, f) Spatial plots of cluster (e, left) with contributing genes scores (f, right) demonstrating colocalization of immune subpopulations. (g) BZ1 and BZ2 scores applied to IZ showing highest expression in IZ4 (left) and select interferon-stimulated genes in CMs (right). (h) Top: representative spatial plots of clusters in 72 hrs post-MI and 168 hrs post-MI samples with bar plots quantifying the representation of each IZ across time/sample as percentage of total IZ pixels. Mono, monocyte; Mac, macrophage; Neut, neutrophil; DC, dendritic cell. Rep, replicating. \* P-value < .05; \*\* P-value < .01; student's t-test.

We took advantage of the low resolution of Visium to test which populations neighbored CM BZ subsets (Figure 2.5d, right); however, we found no evidence of CM co-localization suggesting that the above populations do not directly interact with transcriptionally active BZ CMs (Figure 2.5d). In contrast, interferon (IFN) induced cells (IFNICs) from Mono and Neut clusters, which expressed many stereotypical IFN-stimulated genes (ISGs, e.g., *Ifit1*, *Ifit3*, and *Cxcl10*), formed spatially localized colonies with the highest levels of CM co-localization (Figure 2.5e,f; bottom row; IZ4). BZ1 and BZ2 scores were highest in IZ4 (compared to IZ1-3) and *Isg15* and *Irf7* were most elevated in BZ2 (compared to RZ, BZ1) (Figure 2.5g). This suggests that type I IFN signaling, which when inhibited leads to improved survival after MI, is mediated by or directly impacts BZ CMs<sup>16,35,64</sup>.

**Table 2. 1 Top 10 genes significantly expressed in immune niches**

p_val	avg_log2FC	pct.1	pct.2	p_val_adj	cluster	gene
0	4.642585041	0.621	0.083	0	Sigf	Tnf
0	4.546563782	0.972	0.194	0	Sigf	Il1b
0	4.258273834	0.647	0.111	0	Sigf	Ccl3
0	4.2419071	0.948	0.365	0	Sigf	Nfkbia
0	4.181948792	0.75	0.128	0	Sigf	Ccr12
0	4.145292298	0.719	0.102	0	Sigf	Clec4e
0	3.91156132	0.637	0.115	0	Sigf	Ptgs2
0	3.878328655	0.624	0.018	0	Sigf	Cxcr2
0	3.852393168	0.874	0.298	0	Sigf	Zfp36
0	3.831247938	0.615	0.023	0	Sigf	Mmp9
0	7.035220544	0.954	0.051	0	Retnlg	S100a8
0	6.865329978	0.966	0.04	0	Retnlg	S100a9
0	5.495972995	0.599	0.007	0	Retnlg	Retnlg
0	4.870083892	0.636	0.044	0	Retnlg	G0s2
0	4.177052193	0.711	0.033	0	Retnlg	Slpi
0	4.010073353	0.654	0.059	0	Retnlg	Ifitm1
0	3.987730582	0.958	0.193	0	Retnlg	Il1b

**Table 2. 1 Top 10 genes significantly expressed in immune niches ( continued)**

p_val	avg_log2FC	pct.1	pct.2	p_val_adj	cluster	gene
0	3.959399796	0.369	0.005	0	Retnlg	Gm5483
0	3.928022008	0.869	0.247	0	Retnlg	Cxcl2
4.11E-226	3.835845768	0.532	0.145	1.32E-221	Retnlg	Ccl4
0	4.278192491	0.662	0.099	0	DC	H2-Ab1
0	4.268931624	0.654	0.084	0	DC	H2-Eb1
0	4.189485349	0.667	0.096	0	DC	H2-Aa
0	3.50982192	0.907	0.237	0	DC	Cd74
0	2.943687809	0.468	0.004	0	DC	Cd209a
0	2.821054429	0.513	0.055	0	DC	Ifitm1
0	2.425335935	0.577	0.057	0	DC	H2-DMb1
0	2.389248164	0.606	0.202	0	DC	Rps11
0	2.359492113	0.623	0.064	0	DC	Napsa
0	2.306084061	0.565	0.069	0	DC	H2-DMa
0	2.764672891	0.585	0.191	0	Lyve1	F13a1
0	2.563416035	0.651	0.151	0	Lyve1	Mrc1
0	2.442186141	0.642	0.175	0	Lyve1	C1qc
0	2.416832235	0.664	0.183	0	Lyve1	C1qa
0	2.374928854	0.79	0.389	0	Lyve1	ApoE
0	2.35516606	0.403	0.115	0	Lyve1	Slc9a9
0	2.323983215	0.366	0.117	0	Lyve1	Sepp1
4.80E-176	2.255487668	0.427	0.297	1.55E-171	Lyve1	Rbpj
0	2.211964619	0.669	0.198	0	Lyve1	C1qb
0	2.182444422	0.614	0.167	0	Lyve1	Maf
0	4.81439902	0.967	0.222	0	NSG	Hmox1
0	3.648828514	0.945	0.348	0	NSG	Prdx1
0	3.452320242	0.774	0.033	0	NSG	Slc40a1
0	3.296605144	0.866	0.102	0	NSG	Gclm
0	3.208022366	0.849	0.125	0	NSG	Clec4n
2.86E-263	3.1336122	0.782	0.216	9.21E-259	NSG	Fabp5
1.80E-257	2.967695133	0.935	0.473	5.80E-253	NSG	Fth1
3.65E-306	2.952753163	0.961	0.36	1.17E-301	NSG	Ctsd
0	2.927439496	0.874	0.189	0	NSG	Creg1

**Table 2. 1 Top 10 genes significantly expressed in immune niches (continued))**

p_val	avg_log2FC	pct.1	pct.2	p_val_adj	cluster	gene
0	2.893480828	0.908	0.274	0	NSG	Sqstm1
0	3.735519604	0.485	0.052	0	Arg1	Arg1
0	2.502340009	0.527	0.16	0	Arg1	Thbs1
0	2.342267465	0.446	0.14	0	Arg1	Ccl2
0	2.296805021	0.515	0.194	0	Arg1	Spp1
0	2.167707924	0.721	0.25	0	Arg1	Fn1
0	2.122841142	0.422	0.144	0	Arg1	Alcam
0	2.078776355	0.708	0.351	0	Arg1	Pid1
0	2.056473592	0.532	0.19	0	Arg1	Ccl6
0	2.055340746	0.731	0.26	0	Arg1	Tgfb1
0	1.884366552	0.497	0.212	0	Arg1	Hmox1
0	3.897799615	0.81	0.085	0	Mono	Plac8
0	3.215628397	0.514	0.065	0	Mono	Chil3
0	2.619260657	0.77	0.273	0	Mono	Tmsb10
0	2.476260835	0.89	0.353	0	Mono	Lyz2
0	2.352790797	0.725	0.136	0	Mono	Ccr2
0	2.292568151	0.805	0.204	0	Mono	Coro1a
0	2.258853007	0.511	0.037	0	Mono	Hp
0	2.245313399	0.541	0.205	0	Mono	Rps28
1.39E-288	2.158974149	0.547	0.246	4.49E-284	Mono	Rps29
0	2.15788652	0.574	0.061	0	Mono	Napsa
0	4.060510892	0.815	0.072	0	ISG	Rsad2
0	4.033772702	0.53	0.035	0	ISG	Cxcl10
0	3.805548128	0.76	0.093	0	ISG	Isg15
0	3.325599298	0.633	0.029	0	ISG	Ifit1
0	3.230168277	0.671	0.028	0	ISG	Ifit3
0	2.857262649	0.612	0.034	0	ISG	Ifit2
0	2.849062716	0.675	0.085	0	ISG	Irf7
0	2.792378717	0.582	0.095	0	ISG	Ms4a4c
8.44E-224	2.763585821	0.518	0.144	2.72E-219	ISG	Ccl4
0	2.73809657	0.508	0.02	0	ISG	Mx1

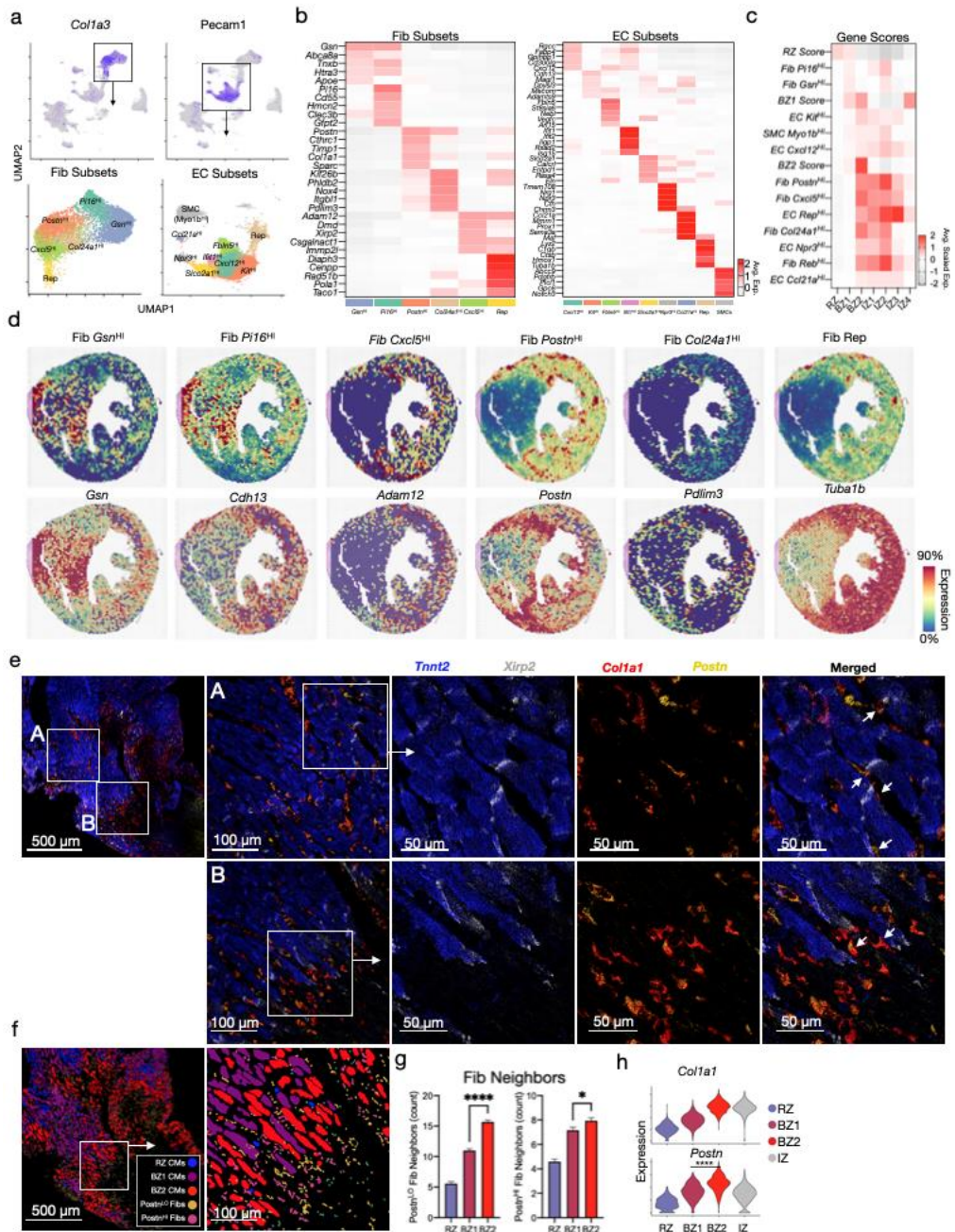
Fibroblasts (Fibs) in the BZ are known to transition from proinflammatory to profibrotic phenotypes where they synthesize supportive ECM components and release matricellular signaling proteins; however, their colocalization with BZ1 and BZ2 CMs remains unknown. To analyze Fibs as well as ECs, we subset coarse clusters defined by elevated expression of *Colla3* and *Pecam1* (encodes Cd31), respectively (Figure 2.6a). Consistent with previous reports, we identified inactivated and activated Fibs by the expression of *Gelsolin* (*Gsn*) and *actin-alpha 2, smooth muscle* (*Acta2*) with additional underlying heterogeneity. Within activated Fibs, we observed a subset of proinflammatory (*Cxcl5<sup>HI</sup>*), matricellular expressing (*Postn<sup>HI</sup>*), *Col24a1<sup>HI</sup>* and replicating (Rep) Fibs<sup>38,65,66</sup>. Similarly, we found heterogenous EC populations (*Kit<sup>HI</sup>*, *Ifit1<sup>HI</sup>*, *Npr3<sup>HI</sup>*, *Slco2a1<sup>HI</sup>*, *Fbln5<sup>HI</sup>*, *Ifit1<sup>HI</sup>*, *Ccl21a<sup>HI</sup>*, Rep), and a small population of smooth muscle cells (*Myo1b<sup>HI</sup>*) (Figure 2.6b)<sup>67-70</sup>. Next, we superimposed Fib and EC subset gene scores within the context of the above defined zones to understand their spatial distribution (Figure 2.6c).

Fibroblasts (Fibs) in the BZ are known to transition from proinflammatory to profibrotic phenotypes where they synthesize supportive ECM components and release matricellular signaling proteins; however, their colocalization with BZ1 and BZ2 CMs remains unknown. To analyze Fibs as well as ECs, we subset coarse clusters defined by elevated expression of *Colla3* and *Pecam1* (encodes Cd31), respectively (Figure 2.6a). Consistent with previous reports, we identified inactivated and activated Fibs by the expression of *Gelsolin* (*Gsn*) and *actin-alpha 2, smooth muscle* (*Acta2*) with additional underlying heterogeneity. Within activated Fibs, we observed a subset of proinflammatory (*Cxcl5<sup>HI</sup>*), matricellular expressing (*Postn<sup>HI</sup>*), *Col24a1<sup>HI</sup>* and replicating (Rep) Fibs<sup>38,65,66</sup>. Similarly, we found heterogenous EC populations (*Kit<sup>HI</sup>*, *Ifit1<sup>HI</sup>*, *Npr3<sup>HI</sup>*, *Slco2a1<sup>HI</sup>*, *Fbln5<sup>HI</sup>*, *Ifit1<sup>HI</sup>*, *Ccl21a<sup>HI</sup>*, Rep), and a small population of smooth muscle cells

(*Myo1b<sup>HI</sup>*) (Figure 2.6b) <sup>67-70</sup>. Next, we superimposed Fib and EC subset gene scores within the context of the above defined zones to understand their spatial distribution (Figure 2.6c).

## Figure 2. 6 Activated fibroblasts localize with BZ2 CMs

(a) Top: Feature plots of Fib (*Colla3*) and EC (*Pecam1*) markers. Bottom: UMAP plots of Fib and EC subsets with marker gene overlayed. (b) Heatmaps of cluster defining DEGs from (a). (c) Heatmap of sn/scRNA-seq derived gene-set scores (scaled for visualization) applied to previously defined BZs and IZs. (d) Spatial feature plots with genes scores shown above and representative genes shown below. (e) mFISH images of BZ (blue, *Tnnt2*; grey, *Xirp2*; red, *Colla1*; yellow, *Postn*). (f) Segmented and classified mFISH data displaying CM and fib subsets. (g) Quantification of *Postn*<sup>HI/LO</sup> fibs surrounding CM subsets. (h) Violin plots of activated fib markers applied to barcode based spatial transcriptomic data. Fib, fibroblast; EC, endothelial cell; SMC, smooth muscle cell; Rep, replicating. \*\*\*\* P-value < .0001, Wilcoxon Rank Test. \* P-value < .05; \*\*\*\* P-value < .0001; Wilcoxon Rank Test.



As expected, we found inactivated Fibs associated with RZ CMs and BZ1 CMs (Figure 2.6c,d). Proinflammatory Fibs (*Cxcl5<sup>HI</sup>*), *Postn<sup>HI</sup>* and Rep Fibs, while homogenously distributed throughout the IZ, also colocalized with BZ2 CMs (Figure 2.6c,d). BZ2 pixels represent a region of overlapping Fib and CM specialization. Spatial correlation analyses supported these claims . Fibs are known to transition from proinflammatory phenotype to a myofibroblast phenotype in the early time points after MI, and our data suggests potential for a differential role of BZ1 and BZ2 CMs in contributing to those dynamics<sup>38,71</sup>. We performed mFISH to validate colocalization of *Postn<sup>HI</sup>* Fibs with BZ2 CMs (Figure 2.6e). To do so, we segmented and classified stromal cells as *Postn<sup>HI/LO</sup>* Fibs based on expression of *Colla1* and *Postn*, and quantified their localization to CM subsets (Figure 2.6f). This data showed that BZ2 CMs preferentially localized to *Postn<sup>HI</sup>* Fibs compared to BZ1 CMs, in agreement with capture-based spatial transcriptomics (Figure 2.6g,h). Analysis of human ischemic heart sample showed a similar correlation of activated fibroblasts and BZ2 CMs (Figure 2.4). *Postn<sup>HI</sup>* Fibs express several genes encoding for matricellular proteins, which have been previously associated with the BZ, notably Secreted protein acidic and cysteine rich (*Sparc*), Tenascin c (*Tnc*), Periostin (*Postn*), and Osteopontin (*Opn*)<sup>72-74</sup>. The latter of which is known binding partner with CD44, a marker gene for BZ2 CMs. These nonstructural signaling proteins appear to have both beneficial and adverse roles in ventricular remodeling as *Postn*<sup>-/-</sup>, *Sparc*<sup>-/-</sup> and *Opn*<sup>-/-</sup> null mice exhibit poor ventricular remodeling after injury, while *Tnc*-null mice have increased ventricular dilation and diastolic function<sup>72,75-77</sup>. Here, our data shows matricellular-expressing Fibs preferentially localize to BZ2 CMs. Taken together, these data provide a spatial transcriptomic atlas of immune and stromal subpopulations in the heart after ischemia and suggest differential inflammatory, fibrotic, and matricellular microenvironments surrounding BZ CMs.

**Table 2. 2 Top 10 genes significantly expressed in stromal niches**

p_val	avg_log2FC	pct.1	pct.2	p_val_adj	cluster	gene
0	3.51001561	0.891	0.245	0	EC_Cyyr1	Fabp4
0	2.97032621	0.563	0.068	0	EC_Cyyr1	Gpihbp1
0	2.90209864	0.565	0.084	0	EC_Cyyr1	Ly6c1
0	2.85507978	0.587	0.096	0	EC_Cyyr1	Cxcl12
0	2.76372065	0.688	0.116	0	EC_Cyyr1	Mgll
0	2.6844408	0.47	0.074	0	EC_Cyyr1	Aqp1
0	2.58562214	0.574	0.085	0	EC_Cyyr1	Kdr
0	2.53680058	0.523	0.113	0	EC_Cyyr1	Rgcc
0	2.49341547	0.483	0.096	0	EC_Cyyr1	Gng11
0	2.46246093	0.676	0.127	0	EC_Cyyr1	Cav1
0	2.947136249	0.346	0.043	0	EC_Fbln5	Rbp7
0	2.904630036	0.642	0.14	0	EC_Fbln5	Tm4sf1
3.26E-70	2.703539556	0.444	0.266	1.05E-65	EC_Fbln5	Arl15
0	2.683860229	0.526	0.118	0	EC_Fbln5	Ly6c1
0	2.658987585	0.527	0.131	0	EC_Fbln5	Cxcl12
0	2.535841745	0.367	0.063	0	EC_Fbln5	Vegfc
4.49E-245	2.458883533	0.423	0.103	1.45E-240	EC_Fbln5	Ldb2
0	2.348273891	0.431	0.054	0	EC_Fbln5	Efnb2
3.29E-250	2.339205303	0.564	0.183	1.06E-245	EC_Fbln5	Ly6a
0	2.325935528	0.608	0.142	0	EC_Fbln5	Epas1
0	2.592581846	0.672	0.233	0	EC_Kit	Cdh13
0	2.253092098	0.423	0.135	0	EC_Kit	Adams9
0	2.049368544	0.551	0.252	0	EC_Kit	Magi1
0	2.016924496	0.578	0.266	0	EC_Kit	Mecom
0	1.967881794	0.582	0.239	0	EC_Kit	Plcb4
0	1.946827921	0.586	0.272	0	EC_Kit	Col4a1
0	1.932103667	0.619	0.296	0	EC_Kit	Apbb2

**Table 2. 2 Top 10 genes significantly expressed in stromal niches( continued )**

p_val	avg_log2FC	pct.1	pct.2	p_val_adj	cluster	gene
0	1.882232025	0.592	0.309	0	EC_Kit	Ptprm
p_val	avg_log2FC	pct.1	pct.2	p_val_adj	cluster	gene
0	1.856954202	0.511	0.232	0	EC_Kit	Col4a2
0	1.855905839	0.551	0.21	0	EC_Kit	Tshz2
0	4.892678017	0.723	0.015	0	EC_Npr3	Tmem108
0	4.466008772	0.458	0.059	0	EC_Npr3	Nrg1
0	4.158232926	0.601	0.01	0	EC_Npr3	Npr3
0	3.854729379	0.559	0.015	0	EC_Npr3	Chrm3
0	3.847648987	0.752	0.122	0	EC_Npr3	Hmcn1
0	3.598024749	0.535	0.032	0	EC_Npr3	Cdh11
0	3.471359734	0.676	0.06	0	EC_Npr3	Cgnl1
0	3.436703343	0.582	0.031	0	EC_Npr3	Vwf
0	3.140696682	0.847	0.232	0	EC_Npr3	Cfh
0	3.056282658	0.549	0.094	0	EC_Npr3	Tmem2
0	4.567316435	0.469	0.003	0	EC_ccl21a	Ccl21a
0	4.28542399	0.67	0.003	0	EC_ccl21a	Mmrn1
0	3.379298286	0.628	0.025	0	EC_ccl21a	Flt4
0	3.342138945	0.445	0.014	0	EC_ccl21a	Sema3a
0	3.27467572	0.605	0.072	0	EC_ccl21a	Reln
0	3.222253291	0.578	0.053	0	EC_ccl21a	Prox1
0	3.096281366	0.413	0.014	0	EC_ccl21a	Adamtsl1
1.56E-130	2.936908585	0.254	0.029	5.02E-126	EC_ccl21a	Igfbp5
4.16E-182	2.880313724	0.569	0.106	1.34E-177	EC_ccl21a	Galnt18
0	2.827074152	0.41	0.028	0	EC_ccl21a	D5Ert615e
0	2.842443706	0.63	0.059	0	Rep	Stmn1
0	2.734718887	0.652	0.022	0	Rep	Top2a
0	2.720548539	0.675	0.248	0	Rep	Tuba1b
0	2.356026011	0.641	0.143	0	Rep	Hmgb2
0	2.311782953	0.669	0.244	0	Rep	Tubb5
0	2.05311559	0.397	0.024	0	Rep	Mki67

**Table 2. 2 Top 10 genes significantly expressed in stromal niches( continued )**

p_val	avg_log2FC	pct.1	pct.2	p_val_adj	cluster	gene
0	1.967469255	0.4	0.011	0	Rep	Tk1
0	1.937016014	0.465	0.015	0	Rep	Birc5
0	1.909540093	0.354	0.027	0	Rep	Diaph3
0	1.83585906	0.704	0.283	0	Rep	H2afz
0	2.614993132	0.359	0.031	0	Cxcl5	Cxcl5
0	2.380670726	0.451	0.139	0	Cxcl5	Tnc
0	2.259309976	0.673	0.232	0	Cxcl5	Adam12
0	2.174525243	0.276	0.051	0	Cxcl5	Ccl2
0	2.118461465	0.352	0.072	0	Cxcl5	Cxcl1
0	2.015404961	0.471	0.193	0	Cxcl5	Serpine1
0	1.984602946	0.748	0.574	0	Cxcl5	Abi1
0	1.821277547	0.366	0.127	0	Cxcl5	Pdpm
0	1.666503891	0.599	0.29	0	Cxcl5	Itga5
0	1.555116835	0.304	0.086	0	Cxcl5	Pak1
0	3.200837474	0.633	0.097	0	Postn	Postn
0	2.787734639	0.466	0.052	0	Postn	Kif26b
0	2.72214	0.634	0.253	0	Postn	Col1a1
0	2.614203586	0.576	0.133	0	Postn	Fn1
0	2.4126012	0.777	0.428	0	Postn	Col1a2
0	2.383611853	0.604	0.366	0	Postn	Sparc
0	2.184919191	0.797	0.458	0	Postn	Col3a1
0	1.913541467	0.481	0.063	0	Postn	Ltbp2
0	1.789313991	0.297	0.042	0	Postn	Ptn
0	1.746314308	0.486	0.171	0	Postn	Kalrn
0	1.849025878	0.29	0.053	0	Hsd11b1	Kcnp1
0	0.973301313	0.847	0.58	0	Hsd11b1	Abca8a
0	0.689186655	0.949	0.851	0	Hsd11b1	Rora
8.47E-307	0.636106764	0.91	0.813	4.53E-302	Hsd11b1	Lama2
2.70E-293	1.133206926	0.31	0.116	1.44E-288	Hsd11b1	Hsd11b1
2.91E-266	1.047780595	0.33	0.139	1.56E-261	Hsd11b1	D630003M21Rik

**Table 2. 2 Top 10 genes significantly expressed in stromal niches( continued )**

p_val	avg_log2FC	pct.1	pct.2	p_val_adj	cluster	gene
4.03E-249	1.063589871	0.291	0.115	2.16E-244	Hsd11b1	Gsta3
7.80E-233	0.858655082	0.635	0.455	4.18E-228	Hsd11b1	Prex2
1.79E-232	1.173545858	0.391	0.209	9.60E-228	Hsd11b1	Fap
1.94E-206	0.639424064	0.767	0.641	1.04E-201	Hsd11b1	Lncpint
0	1.386387304	0.796	0.511	0	Gsn	Gsn
0	1.350807861	0.301	0.059	0	Gsn	Myrip
0	0.978291958	0.474	0.198	0	Gsn	Scara5
0	0.765598268	0.867	0.688	0	Gsn	Kent2
0	0.743878057	0.861	0.589	0	Gsn	Abca8a
0	0.716453747	0.977	0.912	0	Gsn	Celf2
3.44E-268	0.780759303	0.641	0.367	1.84E-263	Gsn	Tnxb
2.47E-259	0.749930237	0.832	0.657	1.32E-254	Gsn	Ebf2
5.43E-255	0.839670056	0.689	0.443	2.91E-250	Gsn	Pcsk6
7.65E-251	0.819534574	0.582	0.327	4.10E-246	Gsn	Htra3
8.11E-246	0.906999779	0.427	0.196	4.34E-241	Gsn	Stxbp6
0	1.698751527	0.347	0.055	0	Dkk3	Accs3
0	1.692584239	0.853	0.58	0	Dkk3	Sgcd
0	1.407488048	0.508	0.182	0	Dkk3	Fmo2
0	1.398499522	0.426	0.119	0	Dkk3	Col6a6
0	1.366219402	0.891	0.561	0	Dkk3	Slit3
0	1.347533032	0.48	0.177	0	Dkk3	Gfra1
0	1.317030864	0.612	0.279	0	Dkk3	Gm2163
0	1.257296591	0.849	0.598	0	Dkk3	Thsd7a
0	1.148381777	0.894	0.665	0	Dkk3	Arhgap24
3.11E-306	1.177136907	0.685	0.351	1.66E-301	Dkk3	4930578G10Rik
0	2.502517544	0.652	0.175	0	Pi16	Pi16
0	2.348484994	0.831	0.324	0	Pi16	Gfpt2
0	2.299831894	0.726	0.217	0	Pi16	Adgrd1
0	2.149047037	0.472	0.16	0	Pi16	Ugdh
0	2.007232557	0.666	0.247	0	Pi16	Uap1
0	1.89153095	0.671	0.229	0	Pi16	Sdk1

**Table 2. 2 Top 10 genes significantly expressed in stromal niches( continued )**

p_val	avg_log2FC	pct.1	pct.2	p_val_adj	cluster	gene
0	1.793118857	0.603	0.257	0	Pi16	Pde10a
0	1.768849156	0.467	0.13	0	Pi16	Cd55
0	1.762935706	0.541	0.179	0	Pi16	Limch1
0	1.678635736	0.44	0.097	0	Pi16	Ackr3
0	2.694508545	0.484	0.005	0	Myh11	Lmod1
0	1.849057598	0.263	0.002	0	Myh11	Ccdc3
0	2.634075385	0.447	0.003	0	Myh11	Slc38a11
0	3.396394293	0.605	0.02	0	Myh11	Kenab1
0	2.301061042	0.389	0.001	0	Myh11	Olfcr78
0	1.619321565	0.263	0.005	0	Myh11	Stac
0	4.17728445	0.758	0.01	0	Myh11	Myh11
0	1.455559675	0.263	0.005	0	Myh11	Map3k7cl
0	3.26989766	0.621	0.038	0	Myh11	Acta2
0	1.55507369	0.274	0.007	0	Myh11	Olfcr558
0	2.703461628	0.474	0.024	0	Myh11	Tagln
0	2.671158936	0.733	0.173	0	SMC	Myo1b
0	3.316591989	0.885	0.273	0	SMC	Plcl1
0	3.407237729	0.652	0.077	0	SMC	Rgs5
0	2.452557432	0.42	0.025	0	SMC	Cacnb4
0	1.779495883	0.277	0.021	0	SMC	Klhl23
0	2.385427423	0.552	0.125	0	SMC	Chn1
0	2.018324511	0.254	0.017	0	SMC	Lrrc4c
0	2.294142887	0.441	0.061	0	SMC	Slc24a3
0	3.874887742	0.677	0.026	0	SMC	Trpc3
0	3.166202694	0.568	0.031	0	SMC	Serpini1

**2.4: DISCUSSION**

The BZ of the infarcted heart has fascinated and mystified the cardiovascular community for nearly a century. Here, we show that the ischemic BZ can be transcriptionally microdissected

and functionally redefined with single cell spatial resolution using single cell and single nuclei RNA-seq, spatial transcriptomics, and multiplexed FISH. We find that BZ CMs divide into two major populations, each with internal substructure. BZ1 CMs (Nppa+Xirp2<sup>-/-</sup>) extended hundreds of microns into the surviving myocardium and were morphologically indistinguishable from nearby RZ CMs despite being transcriptionally distinct. In contrast, BZ2 CMs (Nppa+Xirp2<sup>+/-</sup>) formed a thin, nearly single-cell thick layer of morphologically disturbed cells decorating the complex interface between surviving and dead myocardium.

Our report is not the first report to show that BZ CMs express unique transcriptional fingerprints. In situ hybridization has shown that CMs selectively express candidate genes at the infarct BZ in mice and humans <sup>3</sup>. Here, we extend and generalize the observation by showing that unbiased transcriptional profiling of CM nuclei encodes spatial context within the infarcted heart. The gene sets revealed by single nuclei transcriptomics add to the growing body of literature surrounding BZ CM subsets and transcriptional regulators such as Yap/Tead, Pitx2, and Mef2-, within the injured heart <sup>19,51,59,60,78,79</sup>. In addition, we define local stromal and immune contexts within the RZ, BZ, and IZ, topics that will be mechanistically explored in future manuscripts.

At the time of this writing, a complementary manuscript was published using spatial multi-omics to define the cells and niches in the human heart after MI <sup>31</sup>. Human samples offer a real-world look at tissue from the sickest patients suffering from life-threatening ischemia, cardiogenic shock, and arrhythmias that require ventricular assist devices or transplant, which makes their injured heart tissue available for research. Because of this, one must keep in mind that the effects of acute ischemic injury may be superimposed on prior ischemic injuries and may be affected by clinical interventions such as inotropes, defibrillations, and percutaneous mechanical circulatory support. From a technical perspective, the length scale of human MI is large compared to the size

of commercially available spatial transcriptomic samples. As a result, RZ, BZ, and IZ must be identified grossly and processed separately. Mouse models offer more defined injuries, more controlled sampling times, and transpire on length scales that allow whole short axis sampling using commercial spatial transcriptomic platforms. Mice also allow mechanistic investigations via comparison to genetically modified strains. Finally, mouse models avoid confounding from the clinical care that accompanies life-threatening MI in humans. With that said, mice are merely a model and may not reflect important elements of human disease.

The present report raises many questions for future studies. What are the molecular mechanisms that transmit information from the IZ to BZ1 cells hundreds of microns away? Do immune infiltration impact transcriptional profile of BZ? What are the functions and fates of BZ1 CMs? Do BZ1 and BZ2 have proliferative potential? Do BZ2 CMs represent a recoverable population or are they destined to die? Do they BZ2 CMs represent the evolving edge of “infarct expansion” and is the process modifiable limit development of ischemic heart failure? A specialized subset of BZ2 defined by elevated levels of HIF-regulated genes. This cluster likely represented actively ischemic CMs. Are these BZ2 protected or destined to die?

In conclusion, by defining the single cell spatial transcriptomes of the borderzone, and infarcted heart more generally, we hope to offer a reference dataset for future mechanistic studies aimed at defining and therapeutically modulating the determinants of ischemic heart disease for clinical benefit.

## **2.5: METHODS**

### **2.5.1: Animals**

Adult C57BL/6 J (WT, stock 000664) was purchased from the Jackson laboratory. All experiments were performed with 10- to 14-week-old animals and were carried out using age- and

gender-matched groups without randomization. All mice were maintained in a pathogen-free environment of the University of California San Diego facilities, and all animal experiments were approved by the Subcommittee on Animal Research Care at University of California San Diego.

### **2.5.2.: Permanent ligation (MI)**

For the following surgical procedures, mice were intubated and ventilated with 2% isoflurane. For MI, thoracotomy at the fourth left intercostal space was performed to expose the heart. The left anterior descending artery (LAD) was permanently ligated with an 8-0 nylon suture in MI mice; for I/R injury, the LAD was occluded for 30 minutes to induce ischemia after which the ligature was released to reperfuse the myocardium. Hearts were harvested at various timepoints post-surgery (24hrs, 72hrs).

### **2.5.3: Immunohistochemistry**

Hearts were perfused with 10 ml of cold PBS through the ventricular apex to remove contaminating blood. Ventricular tissue was embedded in OCT and flash frozen in an isopentane bath on dry ice. OCT-embedded hearts were sectioned into serial 10  $\mu\text{m}$  thick short axis sections to use for immunohistochemical staining with hematoxylin and eosin according to the manufacturer's instructions. Sections were stained with the following primary antibodies to identify cellular and biochemical features: cell boundaries (WGA Alexa Fluor488, Invitrogen), actin (Phalloidin Alexa Fluor64, Cell Signaling). Slides were imaged and tiled on Nikon Eclipse Ti2-E widefield microscope.

### **2.5.4: Single-nucleus RNA-seq**

Single nuclei were isolated from frozen tissue using a modified version of the protocol described.<sup>80</sup> Mice hearts were weighed and minced before flash freezing with liquid nitrogen. Minced samples were resuspended in 0.5 ml nuclei lysis buffer (Millipore Sigma, Nuclei EZ prep,

NUC101), 0.2 U/ $\mu$ l RNase inhibitor (stock 40U/ $\mu$ l, Enzymatics Y9240L) and homogenized with a 2 ml Dounce grinder for 10 strokes with A motor and at least 20 strokes with B motor (Sigma-Aldrich D8938). The lysates were resuspended with another 1 mL of nuclei lysis buffer and 2.5 minutes of incubation, and were filtered through 100  $\mu$ m, 50  $\mu$ m and 20  $\mu$ m cell strainers (CellTrics filters 04-004-2318, 04-004-2317, 04-0042-2315). Then, they were centrifuged at 1000 x g for 5 min at 4°C to pellet nuclei. As Cui et al., 2020 described, the nuclear pellet was subsequently washed once in 6 mL of Sucrose buffer and centrifuged the cushioned suspension at 1,000 g for 10 min at 4°C to pellet nuclei. The pellet then was washed with 2ml of Nuclei Storage Buffer with 10  $\mu$ g/ml 4',6-diamidino-2-phenylindole (DAPI) and centrifuged at 1000 x g for 5 min at 4°C (5mg/ml, Invitrogen D1306). 200  $\mu$ l of nuclei wash buffer (freshly 2% bovine serum albumin (BSA) in 1xPBS, 0.2 U/ $\mu$ l RNase inhibitor and 1mM of EDTA) were added and nuclei were resuspended. Fluorescence-activated cell sorting (FACS) were used to sort extracted nuclei. Nuclei was collected based on the separation between DAPI<sup>high</sup> and DAPI<sup>low</sup>; (Figure S.1 c) After sorting using purity mode, DAPI<sup>high</sup> nuclei were pelleted at 1000 x g for 15 min at 4°C, resuspended in 2% BSA and trypan blue stained nuclei suspension were quality controlled and counted using hemocytometer (Hausser Scientific 3110V).

Single-nucleus RNA-seq was performed by microfluidic droplet-based encapsulation, barcoding, and library preparation, (10X Genomics). Paired end sequencing was performed on an Illumina Novaseq instrument. Low-level analysis, including demultiplexing, mapping to a reference transcriptome (mm10-1.2.0-premRNA), and eliminating redundant UMIs, was performed with Cell Ranger 3.0.2 pipeline for 10X samples.

### **2.5.5: Quality control, normalization, and integration**

To account for variations in sequencing depth, total transcript count for each cell was scaled to 10,000 molecules, and raw counts for each gene were normalized to the total transcript count associated with that cell and then natural log transformed. Cells with between at least 200 uniquely expressed genes and genes that at least expressed in 3 cells were retained for further analysis. Ribosomal and hemoglobin genes were excluded to avoid incorporation of any artifacts such as technical variables. Since low quality/ dying cells present a mitochondrial genome, we calculated mitochondrial QC metrics for all samples and replicates from single nuclei and single cells using the *PercentageFeatureSet* function. Then we excluded cells that present more than 5% mitochondrial content. Moreover, we removed doublets by determining cells that contain non endogenous gene markers. (e.g., presence of cardiomyocytes genes such as *Myh6* in fibroblasts subset). Figure(2.1 e, g) shows subsets after filtering and removing doublets/multiples. Highly variable genes across individual datasets were identified with the *FindVariableFeatures* method from the Seurat R package (version 4.1) by selecting 4000 genes with the highest feature variance after variance-stabilizing transformation. Integration of multiple single-nucleus RNA-seq datasets was performed in Seurat to enable harmonized clustering and downstream comparative analyses across conditions <sup>66,67</sup>. Anchoring cell pairs between datasets were identified by Canonical Correlation Analysis and the mutual nearest neighbor's method using the Seurat *FindIntegrationAnchors* function.

### **2.5.6: Spatial Transcriptomics**

Sections obtained from C57BL/6J (Jackson Laboratories) mice were imaged and processed for spatially resolved gene expression using the Visium Spatial Transcriptomics kit (10x Genomics). Samples were immediately snap-frozen in OCT using isopentane that was cooled in

a liquid nitrogen bath. For cryosectioning, samples were equilibrated to  $-22\text{ }^{\circ}\text{C}$ .  $10\text{ }\mu\text{m}$  thick short axis sections were cut from the blocks onto Visium slides (10X Genomics) and processed according to the manufacturer's protocol. Tissue permeabilization time was optimized at 30 minutes for infarcted mouse hearts. Hematoxylin and eosin (H&E) images generated during the Visium protocol were captured at 20x magnification on Nikon Eclipse Ti2-E widefield microscope and exported as tiled tiffs for analysis. Libraries were sequenced on the Illumina NovaSeq platform, and resulting data were processed using SpaceRanger (v.1.2.2, 10X Genomics).

For single-molecule FISH and Sequential Imaging, a panel of target genes was designed to label functionally distinct cell populations identified by single cell/single nuclei transcriptomic data. Primary target probes (22-96 oligonucleotides) were designed for each RNA species and corresponding readout probes were labeled with fluorescent Atto532, Atto594, or Atto647 dyes. Samples for spatial transcriptomics were harvested and flash frozen in OCT. Ventricular short axis cross sections were cut on a cryostat ( $10\text{ }\mu\text{m}$ ), mounted onto functionalized coverslips, and fixed for 10 minutes in 4% paraformaldehyde. The sample was assembled onto a flow cell and loaded into the Rebus Esper spatial omics platform (Rebus Biosystems, Santa Clara). The system automates sequential immunostaining and imaging of RNA spots using on-system fluidics, single molecule fluorescence in situ hybridization (sM-FISH) chemistry, and synthetic aperture optics (SAO) microscopy. Raw images obtained from the High-Fidelity Assay were reconstructed by the Rebus Esper image processing software to generate high-resolution images, which were then registered with immunohistochemistry stains of adjacent tissue sections.

### **2.5.7: Borderzone mapping strategy**

To quantify the spatial distribution of various cell subsets, we performed unsupervised clustering of spatial transcriptomic data and superimposed subset-specific gene scores derived

from snRNA-seq data. Spatial transcriptomic datasets (Visium, 10X Genomics) were integrated into a single unified object (using R package Seurat as described above for snRNA-seq) to permit unsupervised clustering analyses. In this unified space, pixels were classified as either RZ, BZ1, BZ2 or IZ by increasing clustering resolution until respective gene signatures emerged. IZ pixels were sub-clustered for immune niche analyses. Zones were quantified as a fraction of total pixels for a given sample and reported.

Spatial transcriptomic data were integrated using the Seurat workflow, as described above (referenced to 72 hrs post-MI sample), and clustered (resolution = .8), resulting in 12 clusters, which were reordered based on orientation in UMAP space. To classify clusters as RZ, BZ1, BZ2, and IZ, we implemented gene-set scores in a series of hierarchal classifiers as follows (Figure 1.2d). (1) We defined CM and IZ pixels using a CM gene-set score (sum of the top10 DEGs derived from snRNA-seq by comparing all CMs to rest of clusters using *FindMarkers()* function). (2) Clusters that qualified as CM were then classified as RZ or BZ using BZ1 score. (3) Clusters that qualified as BZ were then classified as BZ1 or BZ2 based on BZ2 scores. This hierarchal classification structure was based on snRNA-seq derived CM structure as shown in Figure S.1. To classify a given cluster based on gene-set scores, we performed ROC analysis using *FindMarkers()* with *ident.2* set to the qualifying cluster with the lowest score. Clusters with an AUC > .07 were positively classified. IZ clusters were sub-clustered for immune niche analyses. Zones were quantified as a fraction of total pixels for a given sample and reported.

### **2.5.8: Neighborhood analyses and spatial correlations**

After defining clusters based on CM structure, we qualitatively analyzed the co-localization of immune and stromal subsets by defining gene signatures of major cell types (e.g., macrophages), which formed distinct islands in UMAP plots. We then curated subset-specific gene

lists using *FindMarkers()* function ( $\log_{fc}.\text{threshold} = 1$ ,  $\text{min.pct} = .25$ ,  $\text{assay} = \text{RNA}$ ) by comparing respective clusters to relevant transcriptional neighbors. Gene lists were filtered to remove genes with adjusted p-values  $> .0001$  and sorted by  $\log_{fc}$  (see supplemental data for gene lists). The top10 genes of each list were then summed in the *Spatial* assay of the integrated spatial dataset, normalized to total UMI, and scaled by 10,000. Subset-scores were set to zero if respective major cell type signatures were not present (defined as gene-set scores less than 5). This analysis did not impose restrictions to number of cells or cell-types occupied in a given pixel.

We performed spatial correlation tests (spearman rank) using R's Giotto package. Using this package, we created a spatial network, identified genes with spatially coherent expression patterns via binary spatial extraction, and clustered spatially correlated genes. This analysis was performed with all pixels from representative D3 post-MI sample and with IZ pixels (defined by clustering) to further explore heterogeneity in this region. Correlation tests were also performed with gene-set scores to confirm colocalization patterns inferred from clustering analyses.

### **2.5.9: Pseudotime analysis**

Trajectory analysis of CMs was performed using R package Monocle (v3) with standard functions and inputs. Resolution for clustering was selected such that the resulting trajectory had no branching points. Nodes of trajectory were selected based on cluster composition of control samples.

### **2.5.10: Motif enrichment analysis and gene ontology**

Motif enrichment and gene ontology were performed with the program HOMER (version 4.11) using the *findMotifs.pl* function with the following tags:  $-\text{start} -400 -\text{end} 100 -\text{len} 8,10 -\text{p} 4$ . We used the *FindMarkers* function ( $\text{adj. p-value} < .001$ ;  $\log_{fc} \text{ threshold} > .25$ ) in R package Seurat

to define DEGs between nearest CM clusters for inputs into motif enrichment and gene ontology analyses.

### **2.5.11: Segmentation, Classification, and Quantification of FISH images**

Image analyses were performed using ImageJ or MATLAB (2020a). After FISH imaging, sections were immediately stained with WGA (as described above) to define CM perimeters and create ROIs for subsequent quantification. WGA and FISH images were tiled using *imtile* and registered using *cpselect*, *fitgeotrans*, and *imwrap* to create large, full section, aligned images. ROIs were then classified as RZ, BZ1, or BZ2 based on the percentage of Tnnt2, Ankrd1+Nppa, and Xirp2+Flnc positive pixels. To quantify neighborhood composition, we counted ROIs with centroids within ~100  $\mu\text{m}$  radius of each CM of each classification). We used Tnnt2 values to define ischemic zone border and hand measured minimum distance to each CM using *pdist* function in MATLAB. To quantify contact with neighboring CMs, we created ROI perimeters with various thickness (4, 8, 12, 16  $\mu\text{ms}$ ) and calculated the percentage of Tnnt2 pixels. The thickness of BZ1/2 was quantified by hand measuring contiguous regions of respective CMs using *pdist* function in MATLAB.

### **2.5.12: Human tissue collection**

The study was approved by the University of California San Diego Medical Center Institutional Review Board (IRB 181206) and written informed consent was obtained from the patient prior to LV assist device implantation surgery. The LV apical core biopsy was collected at the time of LV assist device implantation; flash frozen in liquid nitrogen within 10 minutes of explant and stored at  $-80^{\circ}\text{C}$  until spatial transcriptomic processing.

### **2.5.13: Statistics**

Statistical analysis was performed using GraphPad Prism software. All data are represented as mean values  $\pm$  SEM unless indicated otherwise. Unpaired Mann Whitney tests, Wilcoxon rank sum, Spearman correlation, or One-way ANOVA with Tukey's post-hoc analysis to determine statistical significance. P values are indicated by P values less than 0.05 were considered significant and are indicated by asterisks as follows: \*P < 0.05, \*\*P < 0.01, \*\*\*P < 0.001, \*\*\*\*P < 0.0001.

### **2.5.14: Data availability statement**

All original code has been deposited at [GitHub](#) ,Zenodo, DOI: 10.5281/zenodo.7055957, and is publicly available.

## **2.6.: ACKNOWLEDGMENT**

Chapter 2 is adapted is adapted from Calcagno DM\*, **Taghdiri N\***, Ninh VK, Mesfin JM, Toomu A, Sehgal R, Lee J, Liang Y, Duran JM, Adler E, Christman KL, Zhang K, Sheikh F, Fu Z, King KR. Single Cell Spatial Transcriptomics Redefine the Borderzone induced by Myocardial Infarction and Mechanical Injury. Nature Cardiovascular research. 2022(\*Co-author). The dissertation author was the co first author of this paper.

CHAPTER 3: Ischemic injury is not necessary and mechanical trauma is sufficient to elicit BZ biology

### **3.1: ABSTRACT**

In Chapter 2 we discovered the transcriptional fingerprint of Border zone(BZ) after myocardial infarction (MI) and its spatial heterogeneity. In this chapter, we determined the emergence and evolution of borderzone; Surprisingly, the transcriptional BZ emerges within an hour of injury and it's prior to immune infiltration and fibroblast activation. Additionally there is a small fraction of BZ expresses hypoxia regulated genes suggesting that BZ can be governed by non-ischemia model .Then we asked whether BZ is inducible by non-ischemic fine-needle-trauma. Our results suggest that mechanical instability and “loss of neighbor” at the BZ edge are the dominant inducers of the BZ transcriptional response.

### **3.2: INTRODUCTION**

Medical management such as management of symptoms, emergency reperfusion after MI and medication to reduce cardiac workload have dramatically reduced mortality from acute MI.. However, there are no treatment options available to mitigate adverse remodeling in the surviving myocardium BZ after MI, which causes patients progress to heart failure with reduced ejection fraction characterized by dilated ventricular chamber and thinning myocardial walls. This suggests an importance of investigating the emergence and evolution BZ biology.

Using multi-modality analysis of histological and transcriptomic data after ischemic and non-ischemic injuries, we define the spatiotemporal onset and evolution of BZ CM subsets, highlight their prominent mechanotransduction programs, and advance a “Loss of Neighbor” hypothesis to explain our observations.

### **3.3: RESULTS**

#### **3.3.1: Onset and evolution of the transcriptional border zone**

To understand the mechanism(s) that underlie CM specialization after ischemia, we subjected adult mice to left anterior descending coronary artery ligation and harvested hearts at various timepoints along with sham controls and isolated single cells and nuclei (no injury; n = 3, 31580 sc/sn), 1hr (n = 3, 17442 sc/sn), 4hrs (n = 1, 8523 sc/sn), 24hrs (n = 6, 33,336), 72hrs (n = 3, 10380 sc/sn) and 168hrs (n = 3, 20926 sc/sn) for sc/snRNA-seq (Figure S.1a,b). We collected myocardial tissue extending from the non-infarcted RZ to the frankly infarcted IZ to ensure comprehensive capture of BZ biology. The resulting counts matrices were integrated with our previously published single cell RNA-seq (scRNA-seq) datasets collected at similar timepoints after MI to create a unified sc/snRNA-seq object with clusters representing cardiomyocytes (CMs), fibroblasts (Fibs), endothelial cells (ECs), smooth-muscle cells (SMCs), neutrophils (Neus), dendritic cells (DCs), monocytes (Monos), and macrophages (Macs) (Figure S.1.e, f). Most cell types were represented in both whole cell and nuclei data; however, CMs, which are large and difficult to isolate as intact cells, were exclusively represented as nuclei, whereas neutrophils, which have fragile polymorphic nuclei, were primarily represented in whole cell samples (Figure S.1 g-l). From these data, we generated subset-specific gene signatures or gene-set scores (Figure S.1e).

In parallel, we performed spatial transcriptomics (Visium, 10X Genomics) on short-axis sections of hearts from mice subjected to: (i) sham surgery (ii) experimental MIs harvested at 1hr, 4hrs, and 72hrs, and 168hrs post-MI, or (iii) mechanical, nonischemic injury including isoproterenol-treatment, transaortic constriction, and needle pass injury. In total, we analyzed the transcriptomes of 128,192 single nuclei and cells across 23 samples, and 31,359 pixels across 16

spatial transcriptomic samples (Figure S.1b). To quantify the spatial distribution of cell subsets, we integrated spatial transcriptomic data and performed clustering analysis to first understand the native structure of the transcriptomes across space before mapping sn/scRNA-seq-derived CM labels and projecting subset-specific gene-set scores onto space to infer cellular composition, spatial patterning and colocalization, followed by validation using probe-based mFISH (see mapping strategy in methods; Figure.S. 1a).

Our data indicated enrichment of pathways associated with mechanosensing including up-regulation of focal adhesions, cytoskeleton, and sarcomere -associated genes as well as genes previously shown to be regulated by the transcription factor TEAD (YAP/TAZ), a classic mechanotransduction pathway. Together with histological analysis, this led us to propose the “Loss of Neighbor” (LON) hypothesis. Although the BZ is often viewed as being governed by a zone of residual ischemia, only a small fraction of BZ2 CMs expressed genes associated with HIF- or heat shock-regulated genes (Figure 1e). Therefore, we propose a model that does not depend on residual ischemia. Instead, we propose that when cells die due to ischemia, the surviving neighbor cells experience a resulting mechanical instability due to the highly asymmetric loss of force, leading to mechanotransduction that activates cell signaling changes that not only effect the immediate neighbors but also propagate surprising distances to precipitate development of the BZ1 transcriptional phenotype hundreds of microns away.

A prediction of the LON hypothesis is that the BZ should develop quickly. To test this, we performed temporal profiling of CM transcriptomes after ischemia, strategically selecting early time points (1hr and 4hrs post-MI) before immune infiltration as well as later time points (24hrs, 72hrs, and 168hrs). Indeed, we observed rapid development of BZ CM subsets suggesting that immune and fibroblast signaling likely does not cause the observed CM specialization (Figure

3.1a,b). At 1hr post-MI BZ1 CMs represented an average of 29.32% of all CMs whereas BZ2 CMs were not appreciably detected. By 4 hrs post-MI, BZ1 CMs rose to nearly 33% and remained at that level through 168hrs post-MI. BZ2 CMs, although not present at 1hr post-MI, reached maximal abundance at 4hrs post-MI (33%) and monotonically decreased at 168hrs post-MI. To confirm these results, we performed spatial transcriptomics at early timepoints and at 168 hrs post-MI (Figure 3.1c,d). These data showed evidence of BZ1 CMs as early as 1hr post-MI, and a BZ2 signature directly neighboring the infarcted region of anterolateral left ventricle at 4 hr post-that persisted through 168 hrs post-MI (Figure 3.1c,d); however, clustering did not yield BZ2 classification early timepoints despite elevated gene signatures. Comparison of respective zones between times after ischemia showed that markers of immune and fibroblast specialization were not upregulated until later time points demonstrating that BZ specialization occurs prior to immune infiltration and fibroblast activation, though colocalization is required for the full spatial transcriptomic signature (Figure 3.1e).

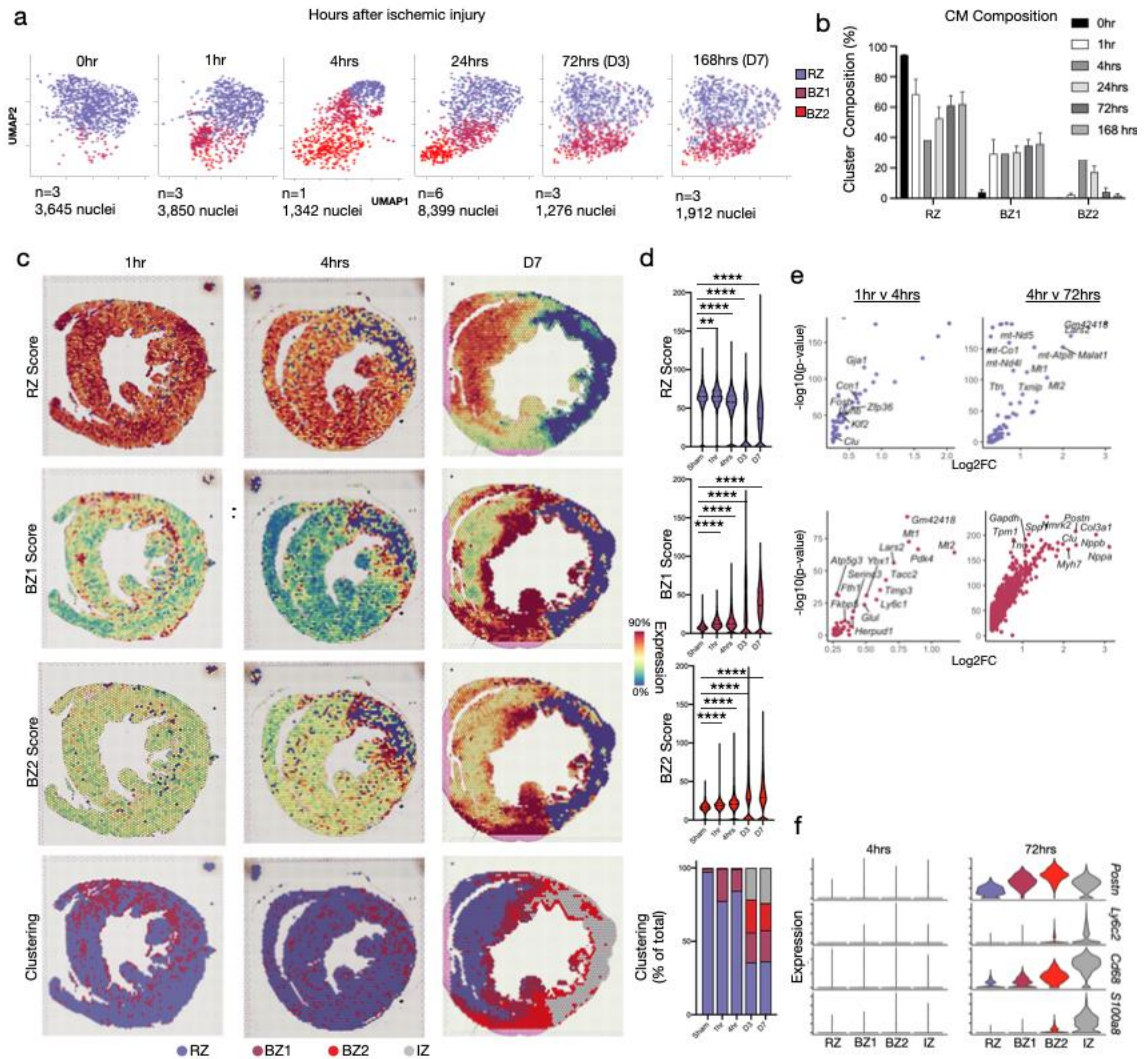


**Figure 3. 1 The transcriptional BZ emerges rapidly after ischemia**

(a) UMAP plots of integrated CMs split by time after ischemic injury. (b) Cluster composition (percentage of total CMs per sample) as a function of time post injury (average displayed). (c) Spatial feature plots of RZ, BZ1, BZ2 scores and clustering results of cross sections from mouse heart 1hr (left), 4hrs (center), and 168hrs (right) post-MI. Clustering results are based integrated spatial dataset. (d) Violin plots of CM subset scores as shown in (c) (median and 25<sup>th</sup>/75<sup>th</sup> percentile demarcated with dashed lines). Bottom: cluster ownership as percentage of total pixels capture. (e) Volcano plots displaying up-regulated genes between indicated times across respective CM subsets. (f) Fib, Mono, Mac, and Neut markers at 4 hrs and 72 hrs post-MI.

Because BZ specialization temporally coincides with early histopathological features of ischemic injury (e.g., contraction band necrosis and wavy myofibrils), we looked for histologic

correlates of BZ1 and BZ2 beginning with H&E-stained sections. Morphological inspection showed normal myocardium in the RZ and disorganized, yet intact, CMs in the IZ where few CM transcripts were captured. In regions with high BZ2 scores we observed wavy myofibrils (Figure 3.2a, box 1) and evidence of CM detachment (Figure 3.2b, box 2). To test this further, we performed actin staining (via phalloidin) and FISH-based spatial transcriptomics on serial sections. *Flnc* expression resembled BZ2 pattern observed by Visium (Figure 3.2b). Analyses of these data revealed that at 4hrs post-MI, BZ2 CMs directly neighbored regions of CMs with highly disordered myofilaments and high actin density indicative of contraction band necrosis in support of the LON hypothesis (Figure 3.2c). Furthermore, TUNEL staining showed that while BZ2 CMs were TUNEL negative, they were immediately adjacent to the densely TUNEL-positive ischemic zone, suggesting that BZ2 CMs are not directly ischemic (Figure 3.2d). Taken together, our data show that the transcriptional BZ develops rapidly, within hours of ischemia, in regions neighboring detached, frankly ischemic CMs.

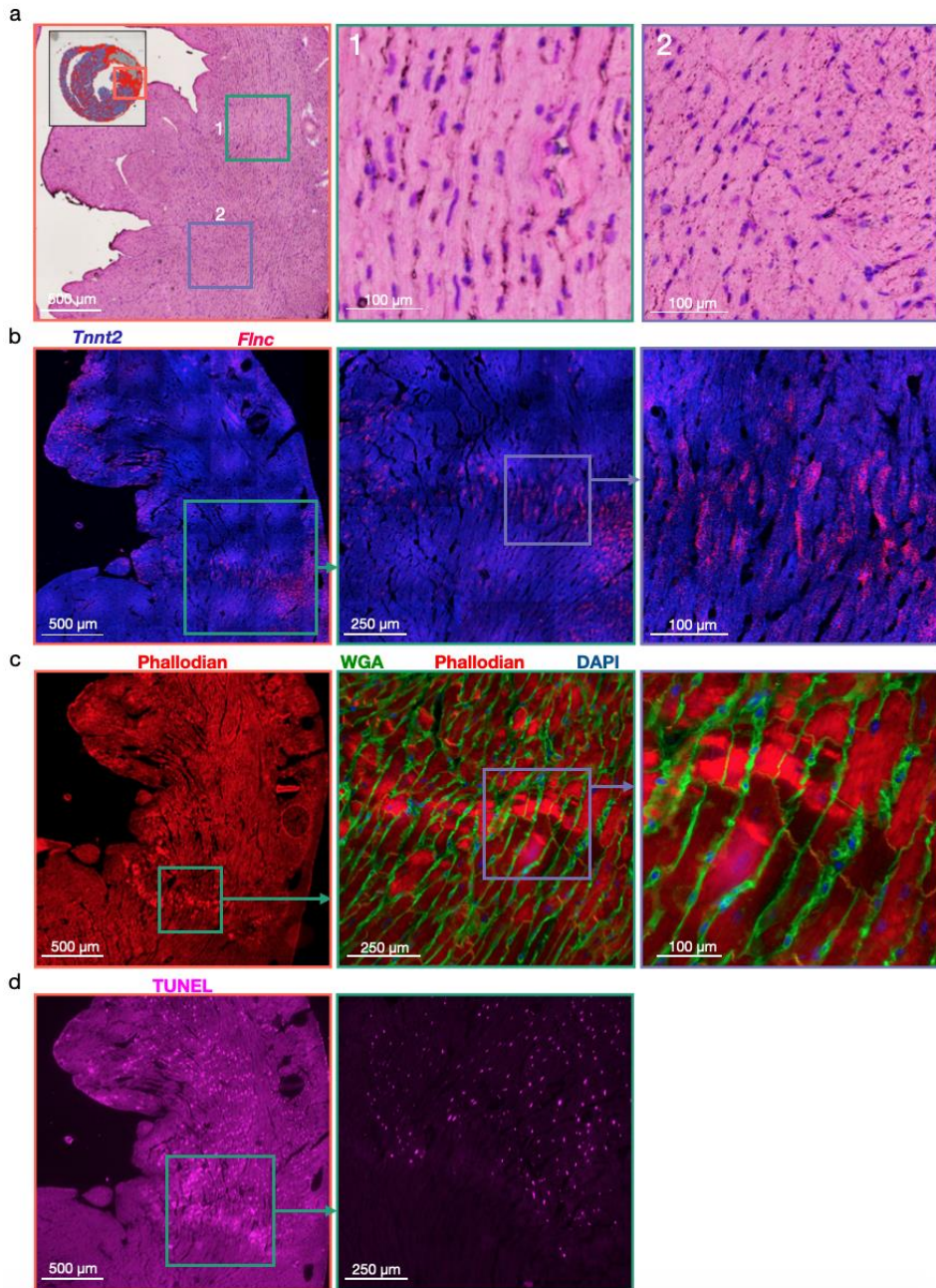


**Figure 3. 2 Morphological features of the emerging borderzone**

(a) H&E-stained serial section of 4 hrs post-MI sample shown in Figure 3.1c(inset). (b) FISH image showing *Tnnt2* (blue) and BZ2 marker gene, *Flnc* (red). (c) Phalloidin (red), WGA (green), and DAPI (blue) staining of consecutive serial section shown in (b). (d) TUNEL staining of consecutive serial section shown in (c).

### **3.3.3: The transcriptional BZ in fine mechanical injury model *invivo***

A prediction of the LON hypothesis is that non-ischemic injuries can also cause LON events and precipitate BZ1 and BZ2 transcriptional responses. To test this, we subjected mice to sharp needle trauma (needle pass, NP) from the epicardium into the mid-myocardium with the goal of causing mechanical disruption without ischemia and harvested the tissue for spatial transcriptomics after 72 hrs (n = 4, Figure 3.3a, b Figure see methods). We excised only a portion of the LV wall. NP injury sites were identifiable in HE-stained sections by regions of detached CMs surrounded by immune infiltrate (Figure 3.3a). Integration of the resulting spatial counts matrices with data from ischemic models showed that the NP injury recapitulated MI with comparable fractions of RZ, BZ1, BZ2, and IZ pixels in the excised areas, and elevated BZ1 and BZ2 gene scores relative to sham (Figure 3.3c,d,e,f).

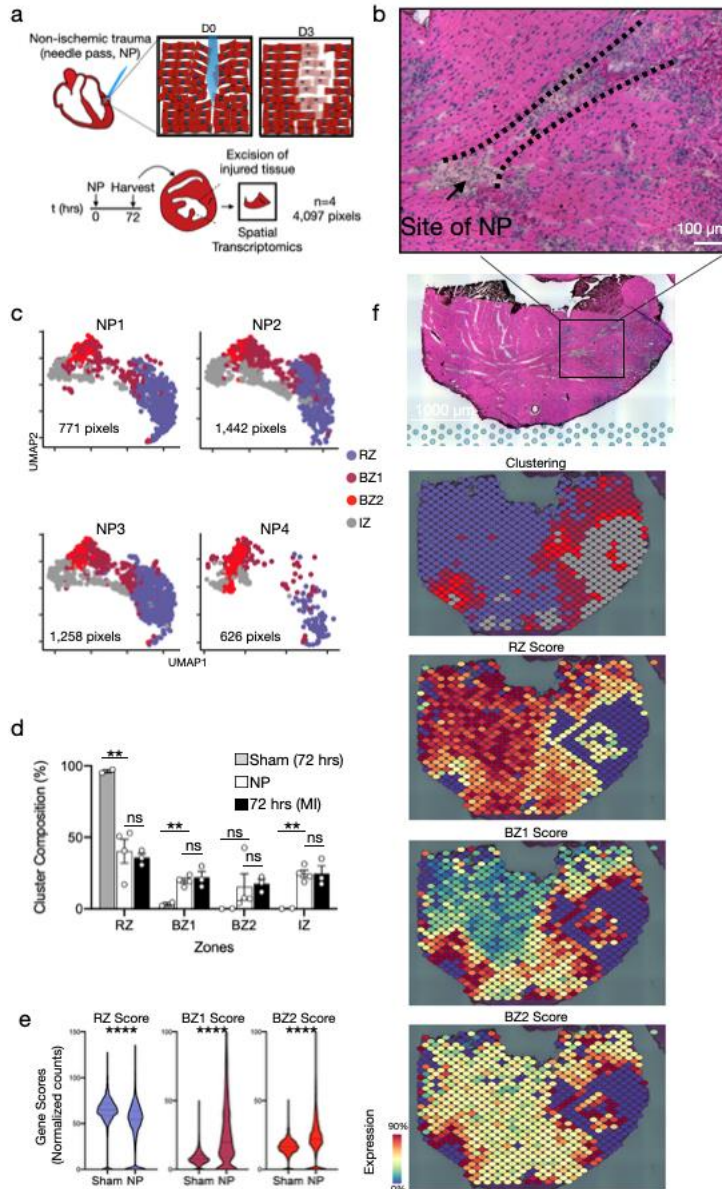


**Figure 3. 3 Micro mechanical trauma is sufficient to elicit BZ biology**

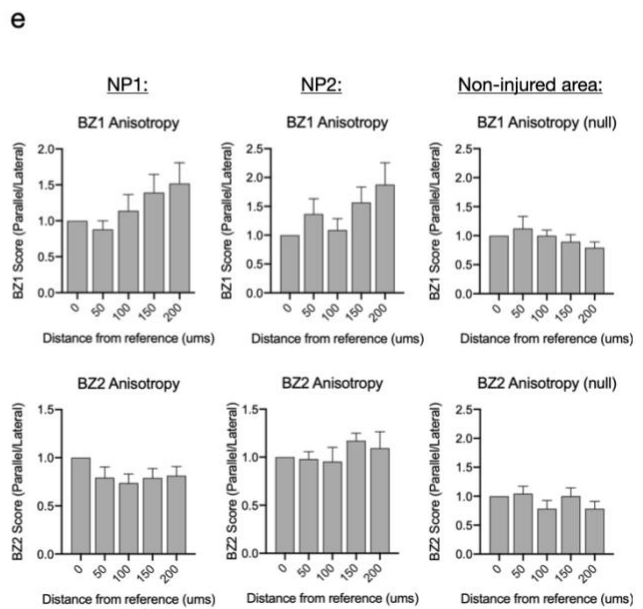
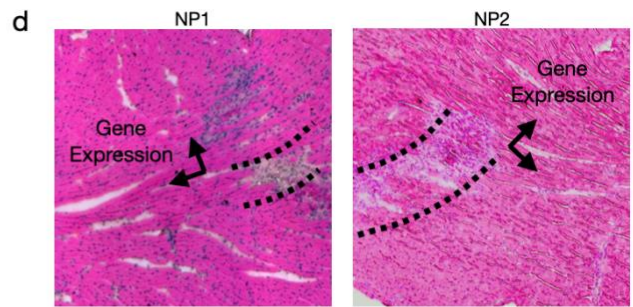
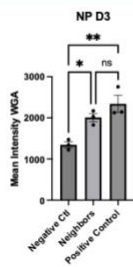
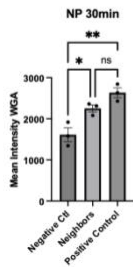
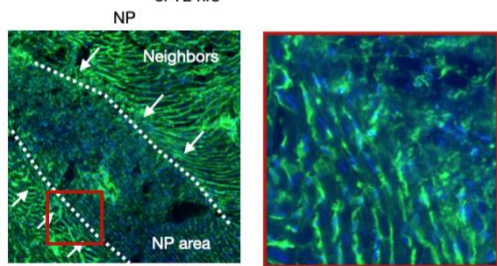
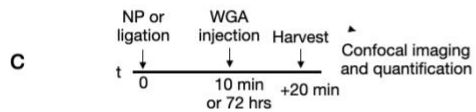
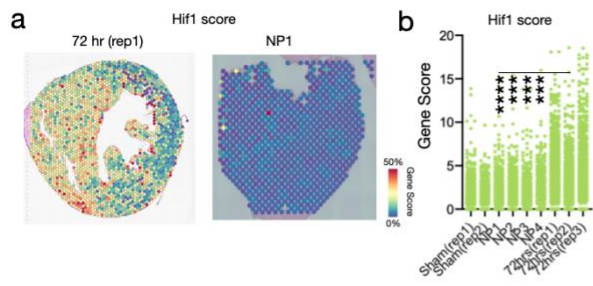
(a) To induce non-ischemic, mechanical trauma in the heart, we subjected hearts to fine needle pass injury (NP, see methods for full details), harvested tissue 72 hrs after injury, and excised injured section of left ventricle for spatial transcriptomics (n = 4; 4,097 pixels). (b) Site of NP injury is identified in HE stained sections by immune infiltrate and disrupted myocyte bundles. (c) UMAP plots of each NP replicate in same integrated space as permanent ligation samples. (d) Bar plots comparing cluster composition of NP (n=4) to sham (n=2) and 72 hrs post-MI (n=3) sample. (e) Violin plots of RZ, BZ1, and BZ2 scores comparing sham to NP injury (all samples combined; median and 25<sup>th</sup>/75<sup>th</sup> percentile demarcated with dashed lines). (f) Spatial plots showing BZ1 and BZ2 signatures (top: clustering; below: gene-set scores) surrounding the site of injury; \*\* P-value < .01, unpaired Student's t-test (d), Mann-Whitney Test (e).

### **3.3.4: Determination of hypoxia in fine mechanical injury**

Since CMs directly lacking contact-neighbors had elevated BZ2 scores and BZ1 scores persisted over couple hundred microns towards the RZ (Figure 3.3f), it is possible that NP injury causes local micro-ischemic events. To test this, we examined NP injury for transcriptional evidence of ischemia by constructing and comparing Hif1 scores (composed of Hif1-dependent genes, see methods) in NP injury to sham and 72 hrs post-MI samples. We found Hif1 scores were significantly decreased relative to 72 hrs post-MI sample and were comparable to sham (Figure 3.4 a,b). In addition, we performed a dye perfusion assay by injecting WGA into LV wall at either 10 min or 72 hrs after NP injury, waited 20 mins for WGA binding, and harvested tissue for imaging . CMs at the site of injury exhibited WGA staining levels similar to RZ suggesting areas are well perfused both immediately and 72 hrs after injury (Figure 3.4 c). Taken together these data show that NP injury is sufficient to induce transcriptional BZ phenotype. Given the dependency of force transmission and muscle fiber orientation, we quantified the anisotropy of BZ gene propagation relative myocyte bundle direction (Figure 3.4 c). To reduce the confounding effects of complex 3D geometries, we limited our analyses to borderzone created by NP injury rather than ischemia because it creates a more focal injury and to myocyte bundles on their longest extent (cut long axis), directly neighboring the site of injury. These analyses showed that BZ1 scores, but not BZ2, propagated greater in the direction parallel to myocyte bundle compared to lateral (Figure 3.4 d, e ,See methods for more information).

### Figure 3. 4 Induction of BZ is independent of ischemia

(a) Hif1 scores applied to representative 72 hrs post-MI sample (left) and NP (right) with quantifications plotted per pixel in (b). In comparison to post-MI hearts, needle pass injuries have a significantly lower Hif1 score compared to the positive control (72 hr MI) samples and is unchanged from negative controls in sham samples. (c) Experimental design of fluorescent dye assay to assess regional perfusion. Wheat germ agglutinin (WGA) conjugated to AlexaFluor 488 was injected directly into LV 10 min or 72 hrs post NP injury and hearts were harvested 20 minutes after injection for imaging and quantification. The representative image in the left panel designates the visualization of the needle pass area designated as the negative control and the reference site designated as neighbors, and the right panel represents a positive control area remote from the site of injury. Quantification of samples harvested 30 minutes and 72 hrs post-NP injury reveal that in both time courses, Neighbors and Positive controls are significantly increased as compared to the Negative Control (Needle pass) sites and are not different from each other (d) Representative H&E stained sections of NP injuries highlighting area of injury in dash lines and directions of adjacent myocyte bundles in arrows used to quantify gene expression. (e) Anisotropy ratios in each sample with non-injured area (right) showing no significant anisotropy in the borderzones of needle pass injuries. \*P-value < 0.05, \*\*P-value < 0.01, \*\*\*P-value < 0.001, \*\*\*\*P-value < 0.0001; One-way ANOVA with Tukey's post-hoc analysis.



### 3.3.5: The transcriptional BZ in other mechanical injury model *in vivo*

We investigated if other non-ischemic injury models were also sufficient to induce BZ signatures. We subjected mice to either a single high-dose of isoproterenol-treatment (ISO) or transaortic constriction (TAC) and performed spatial transcriptomics after 72 hrs (Figure 3.5a). These data show that both injury models result in a predominate BZ1 signature, homogenously dispersed throughout the myocardium suggesting that BZ1 can be induced by CM stretch (Figure. 3.5 b,c ,d).

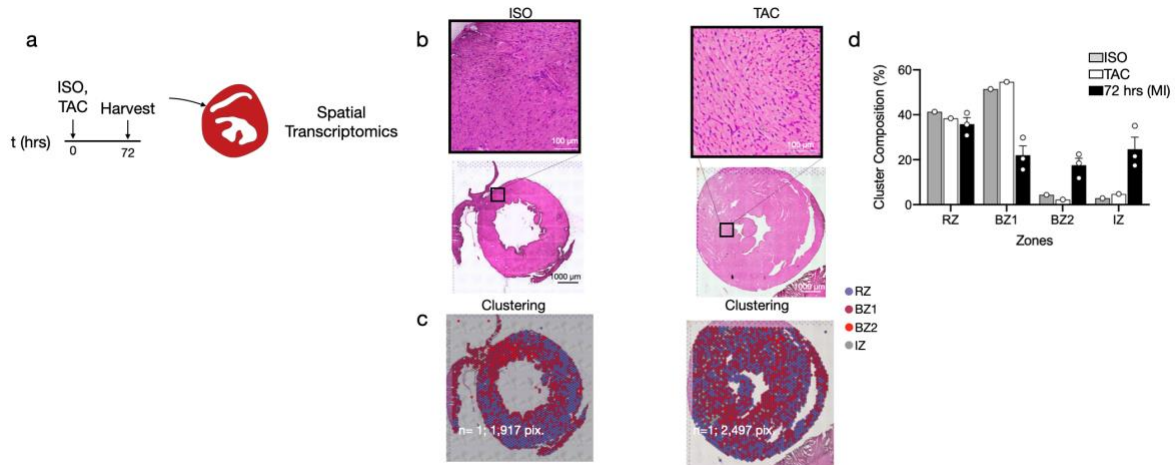


**Figure 3. 5 Induction of BZ in other mechanical injury model**

(a) Mice were subjected to either isoproterenol-treatment (ISO; n=1) or transaortic-constriction (TAC; n=1) and harvested for spatial transcriptomics after 72 hrs. (b) H&E sections at low magnification (lower panel) and high magnification (top panel) on ISO and TAC. (c) Clustering results of spatial transcriptomic data based on integrated dataset (d) Cluster composition quantified below (percentage of total pixels per sample); \*\* P-value < .01, unpaired Student's t-test (d).

### 3.3.6: The transcriptional BZ in fine mechanical injury model *in vitro*

Finally, we repurposed the canonical *in vitro* scratch assay to test our LON hypothesis in confluent cultures of isolated neonatal rat ventricular myocytes (Figure 3.6). The physical scratches in the culture plates separated myocytes from their neighbors, and we measured their

transcriptional responses to the mechanical separation. The loss of cardiomyocyte neighbors created transcriptional upregulation of BZ2 genes *Flnc* and *Xirp2*, and to a lesser extent BZ1 gene *Ankrd1* compared to unscratched control plates. Taken together, these data show that non-ischemic, mechanical trauma is sufficient to induce the development of BZ and provides support for our loss of neighbor hypothesis.

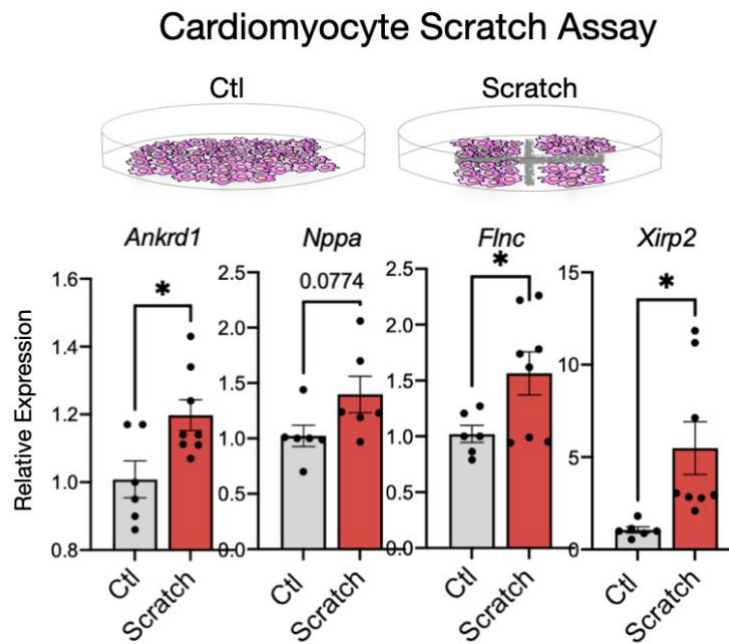


**Figure 3. 6 Induction of BZ in micro injury model invitro (NRVM)**

Scratch assay was performed on confluent cultures of neonatal rat ventricular myocytes (NRVM's) seeded on 6 well plates, and RNA was isolated from cultured cells 24 hrs after scratch was performed. Borderzone genes *Ankrd1*, *Flnc*, and *Xirp2* were significantly increased in scratched NRVM's compared to unscratched control plates (n = 6-8, \*P-Value < 0.05) and *Nppa* did not reach statistical significance (P-value = 0.0774).

### 3.4: DISCUSSION

In this chapter we found that the transcriptional BZ develops rapidly, within hours after ischemia, arguing for a direct response by cardiomyocytes rather than an indirect response to infiltrating myeloid cells and activation of fibroblasts. Although prevailing wisdom attributes

borderzone biology to residual peri-infarct ischemia, we found only subsets of BZ CMs expressing HIF-dependent gene programs and they were primarily limited to post-MI Day 1. By contrast, we found that the dominant transcriptional fingerprint of BZ CMs was detectable throughout the first week after MI and was characterized by expression of genes encoding mechanosensing and mechanotransduction proteins. This prompted us to test whether mechanical injury was sufficient to induce BZ transcriptional profiles. Indeed, spatial transcriptomic profiling in three in vivo models (TAC, Isoproterenol, and needle pass) as well as qPCR of BZ marker genes following mechanical scratch of cardiomyocyte cultures all suggested that mechanical injury is sufficient to induce BZ expression patterns. This inspired the “Loss of Neighbor Hypothesis” (LON), in which we propose that ischemia causes cell death in the IZ, which results in loss of cell neighbors from the perspective of surviving cells at the IZ-BZ interface. We propose that LON at the IZ-BZ interface causes mechanical destabilization that can be transmitted across many cell lengths (hundreds of microns) into the surviving myocardium to induce CM to express BZ1 genes. We speculate that pressure overload and isoproterenol predominantly induce BZ1 because they generate destabilizing mechanical forces minimal frank LON whereas the needle pass model generates a combination of LON and mechanical destabilization, resulting in BZ2 and BZ1 CMs. The in vitro scratch test is arguably the clearest evidence that mechanical cell disruption can induce BZ genes.

Finally, it is tempting to speculate that if morphologically deranged BZ2 CMs at the IZ edge are fated to die, then they would create new LON events for their closest BZ1 CM neighbors and provide a plausible mechanism for “infarct expansion”, a long investigated phenomenon wherein infarcts extend well beyond territories supplied by an obstructed vessel <sup>13, 65, 66</sup>. Future

work will aim to mechanistically explore these ideas via modulation of candidate determinants of BZ1 and BZ2 in the above injury models.

### **3.5: METHODS**

#### **3.5.1: Animals**

Adult C57BL/6 J (WT, stock 000664) was purchased from the Jackson laboratory. All experiments were performed with 10- to 14-week-old animals and were carried out using age- and gender-matched groups without randomization. All mice were maintained in a pathogen-free environment of the University of California San Diego facilities, and all animal experiments were approved by the Subcommittee on Animal Research Care at University of California San Diego.

#### **3.5.2.: Permanent ligation (MI)**

For the following surgical procedures, mice were intubated and ventilated with 2% isoflurane. For MI, thoracotomy at the fourth left intercostal space was performed to expose the heart. The left anterior descending artery (LAD) was permanently ligated with an 8-0 nylon suture in MI mice; for I/R injury, the LAD was occluded for 30 minutes to induce ischemia after which the ligature was released to reperfuse the myocardium. Hearts were harvested at various timepoints post-surgery (1hr, 4hrs, 24hrs, 72hrs, and 168hrs).

#### **3.5.3: Transverse Aortic Constriction (TAC) and Isoproterenol treatment (ISO)**

Pressure overload injury was surgically produced by constriction of the transverse aorta. The chest was opened at the second left intercostal space, and a 7-0 nylon suture was loosely tied around the transverse aorta between the left carotid and innominate arteries. A blunt-end 27G needle was placed across the nylon knot along the transverse aorta to control the degree of constriction. The nylon knot was then tightened against the 27G needle. Once the constriction was secured with a double knot, the needle was quickly removed. The ribs and intercostal muscles were

closed by 6-0 absorbable nylon sutures, and the skin was sutured with 6-0 nylon suture. Hearts were harvested at day 3 post-surgery.

Isoproterenol hydrochloride salts were dissolved in 1 mL of saline for a final concentration of 100 mg/mL and administered via intraperitoneal injection at a dose of 300 mg/kg body weight. Hearts were harvested 3 days post treatment for downstream analysis. All mice used in these studies were monitored for signs of distress, acute heart failure, and administered Buprenorphine as an analgesic in surgical conditions.

#### **3.5.4: Cardiac Needle Pass Injury (NP)**

Mice were anesthetized under 2% isoflurane. Partial thoracotomy was performed between the third and fourth left intercostal space and a chest retractor was inserted. Following identification of the left anterior descending artery (LAD), a 28G beveled needle was inserted into the lateral left ventricular (LV) wall to the right of the LAD at the level in which the vessel is usually occluded in the MI or ischemia/ reperfusion (I/R) surgical models. The needle is held in position for 3 seconds before withdrawn. The chest retractor is removed, and the chest and skin are closed with 6-0 prolene sutures. To reduce complications due to pneumothorax, a sterile 20G flexible angiocatheter is placed within the pleural space before the chest is sutured closed. After closure of the skin, a syringe is attached to the angiocatheter and negative pressure is manually applied as the catheter is withdrawn. Surgical glue is then applied to the remainder of the skin incision.

#### **3.5.5: Scratch Assay**

Neonatal rat ventricular myocytes (NRVM's) were isolated from 1-day old Sprague-Dawley hearts. Cardiomyocytes were liberated by collagenase II digestion (Worthington) and were then purified by percoll density gradient. Myocytes were then seeded onto gelatin-coated, 6-well

plates at a density of  $6.5 \times 10^6$  cells per well in 10% fetal bovine serum in DMEM supplemented with 100 units/ml penicillin. Once confluent and simultaneously beating, myocytes were serum starved for 24 hours. Scratch was performed across the cell layer in a vertical line using 1 mm pipette tip held perpendicular to the bottom of the well. An additional scratch was performed perpendicular to the first line. Cells were washed with PBS 24 hours post-scratch, and RNA was isolated from the cells using RNeasy Mini kit (Qiagen 74536) and reverse transcribed (Applied Biosystems 4368813). Real-time qPCR was performed with the following TaqMan specific primers for Ankrd1 (4448892 Rn00566329\_m1), Flnc (4351372 Rn01500378\_m1), Nppa (4331182 Rn00664637\_g1), Xirp2 (4331182 Rn01640240\_m1), and Gapdh (4331182 Rn01775763\_g1).

### **3.5.6: Immunohistochemistry**

Hearts were perfused with 10 ml of cold PBS through the ventricular apex to remove contaminating blood. Ventricular tissue was embedded in OCT and flash frozen in an isopentane bath on dry ice. OCT-embedded hearts were sectioned into serial 10  $\mu\text{m}$  thick short axis sections to use for immunohistochemical staining with hematoxylin and eosin according to the manufacturer's instructions. Sections were stained with the following primary antibodies to identify cellular and biochemical features: cell boundaries (WGA Alexa Fluor488, Invitrogen), actin (Phalloidin Alexa Fluor64, Cell Signaling), and apoptosis (TUNEL Alexa Fluor647, Invitrogen). Slides were imaged and tiled on Nikon Eclipse Ti2-E widefield microscope.

### **3.5.7: Single-nucleus RNA-seq**

Single nuclei were isolated from frozen tissue using a modified version of the protocol described<sup>80</sup> in 2.5.4.

### **3.5.8: Quality control, normalization, and integration**

To account for variations in sequencing depth, total transcript count for each cell was scaled to 10,000 molecules, and raw counts for each gene were normalized to the total transcript count associated with that cell and then natural log transformed. Cells with between at least 200 uniquely expressed genes and genes that at least expressed in 3 cells were retained for further analysis. Ribosomal and hemoglobin genes were excluded to avoid incorporation of any artifacts such as technical variables. Low quality/ dying cells present a mitochondrial genome were calculated as a mitochondrial QC metrics for all samples and replicates from single nuclei and single cells using the *PercentageFeatureSet* function. Cells that present more than 5% mitochondrial content were then removed. Moreover, we removed doublets by determining cells that contain non endogenous gene markers. (e.g., presence of cardiomyocytes genes such as *Myh6* in fibroblasts subset). Figure S.1f, h, l) shows subsets after filtering and removing doublets/multiples. Highly variable genes across individual datasets were identified with the *FindVariableFeatures* method from the Seurat R package (version 4.1) by selecting 4000 genes with the highest feature variance after variance-stabilizing transformation. Integration of multiple single-nucleus RNA-seq datasets was performed in Seurat to enable harmonized clustering and downstream comparative analyses across conditions. Anchoring cell pairs between datasets were identified by Canonical Correlation Analysis and the mutual nearest neighbor's method using the Seurat *FindIntegrationAnchors* function.

### **3.5.9: Spatial Transcriptomics**

Sections obtained from C57BL/6J (Jackson Laboratories) mice were imaged and processed for spatially resolved gene expression using the Visium Spatial Transcriptomics kit (10x Genomics). Samples were immediately snap-frozen in OCT using isopentane that was cooled in

a liquid nitrogen bath. For cryosectioning, samples were equilibrated to  $-22\text{ }^{\circ}\text{C}$ .  $10\text{ }\mu\text{m}$  thick short axis sections were cut from the blocks onto Visium slides (10X Genomics) and processed according to the manufacturer's protocol. Tissue permeabilization time was optimized at 30 minutes for infarcted mouse hearts. Hematoxylin and eosin (H&E) images generated during the Visium protocol were captured at 20x magnification on Nikon Eclipse Ti2-E widefield microscope and exported as tiled tiffs for analysis. Libraries were sequenced on the Illumina NovaSeq platform, and resulting data were processed using *SpaceRanger* (v.1.2.2, 10X Genomics).

### **3.5.10: Determination of Regional Ischemia or Hypoxia**

Needle pass injury was performed, and wheat germ agglutinin conjugated (WGA) to Alexa Fluor 488 (Invitrogen W11261) was injected directly into the left ventricle (1 mg/ml) at 10 minutes or at 72 hrs after needle pass injury. Hearts were harvested 30 minutes after WGA injection and embedded in OCT followed by flash freezing in isopentane cooled with dry ice. Needle pass injury site was visualized and captured in  $10\text{ }\mu\text{m}$  thick sections using Nikon Eclipse Ti2-E widefield microscope under 20x objective. Fluorescent pixel intensities were quantified by sampling 4 regions of interest (ROI's) of equal areas at the site of needle injury used as the negative control, the zone directly neighboring the site of injury designated as Neighbors, and an uninjured area of individual hearts designated as the positive control for WGA fluorescence. ROI's from each site were analyzed for fluorescence intensity using Fiji image analysis software. These perfusion experiments were complimented with gene scores derived from unsupervised analysis of differentially expressed genes in hypoxia inducible transcripts in the Hif1 pathway (Egln3, Vegfa, Gbe1, Atf3, Pfkf, Mthfd11).

### **3.5.11: Spatial patterning of CM signatures**

Line scans were performed by drawing a vector from RZ to IZ pixels (defined by spatial clustering analyses and *Tnnt2* expression). Genes scores were reported as a function of distance from a reference line (orthogonal to line scan). Scores from pixels with similar distances were averaged.

For CM neighbor analysis, we quantified the fraction of RZ, BZ1, and BZ2 pixels in second-order neighbors (defined by clustering analyses). IZ pixels were not considered. Results were binned based on reference pixel CM classification and reported.

For muscle fiber and gene expression analyses, due to the complex 3D geometry of heart muscle fibers, we limited our analyses to borderzone created by needle pass injury rather than ischemia because it creates a more focal injury and to myocyte bundles on their longest extent (cut long axis), directly neighboring the site of injury. This increased the chance of analyzing bundles traveling in the same plane as the 2D section. We examined HE stained sections of needle pass injury to qualify corresponding spatial transcriptomic pixels and to determine the orientation of vectors parallel and lateral to muscle fiber. From this, we quantified BZ scores as a function of distance (0 to 200 microns) relative to qualified reference pixels in both directions (parallel and lateral) and calculated an anisotropy ratio (parallel/lateral).

### **3.5.12: Statistics**

Statistical analysis was performed using GraphPad Prism software. All data are represented as mean values  $\pm$  SEM unless indicated otherwise. Unpaired Mann Whitney tests, Wilcoxon rank sum, Spearman correlation, or One-way ANOVA with Tukey's post-hoc analysis to determine statistical significance. P values are indicated by P values less than 0.05 were considered

significant and are indicated by asterisks as follows: \*P < 0.05, \*\*P < 0.01, \*\*\*P < 0.001, \*\*\*\*P < 0.0001.

### **3.6.: ACKNOWLEDGMENT**

Chapter 3 is adapted is adapted from Calcagno DM\*, **Taghdiri N\***, Ninh VK, Mesfin JM, Toomu A, Sehgal R, Lee J, Liang Y, Duran JM, Adler E, Christman KL, Zhang K, Sheikh F, Fu Z, King KR. Single Cell Spatial Transcriptomics Redefine the Borderzone induced by Myocardial Infarction and Mechanical Injury. Nature Cardiovascular research. 2022(\*Co-author). The dissertation author was the co first author of this paper.

## **CHAPTER 4: Macrophage calcium reporter mice reveal immune cell communication *in vitro* and *in vivo***

### **4.1: ABSTRACT**

Cell communication underlies emergent functions in diverse cell types and tissues. Recent evidence suggests that macrophages are organized in communicating networks, but new tools are needed to quantitatively characterize the resulting cellular conversations. Here, we infer cell communication from spatiotemporal correlations of intracellular calcium dynamics that are non-destructively imaged across cell populations expressing genetically encoded calcium indicators. We describe a hematopoietic calcium reporter mouse (Csf1r<sup>Cre</sup>GCaMP5<sup>fl</sup>) and a computational analysis pipeline for inferring communication between reporter cells based on “excess synchrony.” We observed signals suggestive of cell communication in macrophages treated with immune-stimulatory DNA *in vitro* and tumor-associated immune cells imaged in a dorsal window chamber model *in vivo*. Together, the methods described here expand the toolkit for discovery of cell communication events in macrophages and other immune cells.

### **4.2: INTRODUCTION**

Cell communication underlies emergent functions such as cognition in the brain <sup>81</sup>, metabolism in the liver <sup>82</sup>, and cyclic contraction in the heart<sup>83</sup>. It productively coordinates tissue morphogenesis during development, but it can also be maladaptive by spreading cell damage after injury <sup>84-88</sup>. Substantial efforts have been devoted to advancing the experimental toolkit for discovery of communication between electrically excitable cells such as neurons; however, considerably less is known about the functional connectedness of the far more numerous “non-excitable” cells <sup>89,90</sup>. Detection of information transfer between non-excitable cells requires a high degree of suspicion and experimental serendipity when investigated using destructive, low

throughput, and low temporal resolution assays <sup>91-93</sup>. However, once discovered, mechanisms of communication such as mechanical coupling, transmembrane signaling, gap junction communication, secreted cytokines, or extracellular vesicles can be systematically explored with molecular specificity using genetic and pharmacologic perturbations as well as co-cultures or chimeric mouse models <sup>94-96</sup>. Since discovery is currently a barrier, we set out to develop tools for recognition and quantification of cell communication events in non-excitabile cells. We applied them to the study of communication in macrophages and other immune cells.

Macrophages are non-excitabile innate immune cells found resident in virtually every tissue and augmented by hematopoietic sources such as the bone marrow <sup>97</sup>. They patrol local tissue microenvironments, remove dead cells after injury, mount innate and adaptive anti-pathogen responses during infections, and facilitate immune recognition of cancer <sup>98,99</sup>. Morphologic evidence suggests that macrophages are arranged as networks of cells and there is evidence that they communicate with cardiomyocytes to influence cardiac conduction <sup>7</sup>. Existing methods for studying communication between macrophages include transfer of microinjected or scrape loaded membrane impermeant dyes, fluorescence recovery after photobleaching, measurement of electrical conductance via patch clamping, or dynamic intracellular imaging of fluorescent reporter molecules <sup>8</sup>.

Calcium represents an attractive indicator of cell communication in macrophages because it is a dynamic second messenger influenced by multiple signaling pathways. In non-communicating populations of cells, calcium dynamics are not expected to be correlated. Therefore, we reasoned that correlated calcium dynamics, if detected, could be used to infer cell communication, even if the molecular stimuli, mediators, and mechanisms were not known. Measurement of calcium can be achieved by imaging exogenously loaded dye in cell culture <sup>100,101</sup>

or in intact tissue slices <sup>102</sup>, but these reagents are not reproducibly loaded *in vivo*. Genetically encoded calcium indicators (GECIs) have emerged as durable non-destructive longitudinal reporters of calcium dynamics in populations of cells both *in vitro* and *in vivo*. The methods for quantification and the number of available GECIs is rapidly expanding <sup>103-110</sup>. When absolute quantification of calcium concentrations are required, ratiometric GECI's can be used, however monochromatic GECI's are sufficient for dynamic relative fluorescence measurements <sup>102,111</sup>.

Here, we describe a method for detecting cell communication in macrophages and other immune cells using a hematopoietic calcium reporter mouse (Csf1r-Cre x GCaMP5) and a computational pipeline that infers locations and times of communication by quantifying “excess synchrony.” We show that these methods allow discovery and quantification of cell communication in DNA-stimulated macrophages *in vitro* and peri-tumor immune cells *in vivo*. Together, the methods expand our toolkit for discovering and quantitatively investigating immune intercellular communication.

## **4.3: RESULTS**

### **4.3.1: Immune calcium reporter mouse construction and characterization**

To enable non-destructive quantification of calcium dynamics in macrophages, we bred mice expressing Cre recombinase under the transcriptional regulation of the hematopoietic colony-stimulating factor 1 receptor promoter (Csf1r-Cre) with mice expressing a Cre-delectable LoxP-flanked STOP sequence separating a constitutive CAG promoter from the downstream genetically encoded calcium indicator (GCaMP5) followed by IRES-tdTomato as a reference reporter <sup>112</sup>.

After Cre-mediated excision of the STOP sequence, both GCaMP5 and tdTomato were expressed in a bicistronic fashion. Csf1r<sup>Cre</sup> was chosen because the Csf1 receptor is expressed broadly by adult macrophages; however, the reporter will be activated in all Csf1r-expressing cells

and their progeny. We first evaluated the distribution of expression in adult offspring ( $Csf1r^{Cre}GCaMP5^{fl}$ ) using confocal imaging of the heart, spleen, kidney, and lung (Figure S1C). We also performed flow cytometric analysis of peripheral blood leukocytes and cells released from digested solid organs. This revealed tdTomato expression in multiple hematopoietic lineages, allowing calcium dynamics to be screened across a broad range of hematopoietic subsets and tissue resident macrophages. We focused on macrophages because we and others have found them to be morphologically organized as potentially communicating networks in solid organs and because recent studies in the heart showed that they functionally alter cell communication during cardiac conduction <sup>7</sup>.

#### **4.3.2: Calcium dynamics of macrophage cell death induced by DNA sensing**

We first examined the  $Csf1r^{Cre}GCaMP5^{fl}$  reporter cells in vitro. Bone marrow-derived macrophages (BMDMs) were isolated, differentiated with macrophage colony-stimulating factor (m-CSF), and serially imaged using time-lapse fluorescence microscopy in an environmentally controlled chamber. This enabled non-destructive imaging at single-cell resolution over long durations and at multiple locations, but with limited sampling frequency. To define baseline calcium signals we imaged for 48 h at a sampling interval of 2 min and observed negligible changes in fluorescence (Figure 4.1A). We next evaluated freely diffusible innate immune stimuli such as lipopolysaccharides (LPS) or cyclic di-GMP but again observed no response. However, when we stimulated cells with double stranded DNA (dsDNA) (Herring Testis DNA, 2 kbp) complexed with a polyelectrolyte transfection reagent (Lipofectamine 2000; Invitrogen), hereafter termed dsDNA, the macrophages exhibited marked fluorescence changes, as demonstrated by maximum image projections (MIPs), percentage fluorescence area, and number of fluorescent cells ( $n = 6$ ,  $p < 0.0001$ ) (Figure 4.1B–3.1D). At a single-cell level, the calcium responses were transient ( $7 \pm 3$

min in duration), asynchronous (distributed throughout the entire 48-h observation period) (Figures 1E–1G) and lacked spatial organization (Figure 4.1H), all of which are consistent with the particulate nature of complexed dsDNA and its need for uptake by cells before engaging by cytosolic sensors<sup>85</sup>. Inspection of gray-scale differential interference contrast (DIC) images suggested that each fluorescence increase was followed closely by changes in cell morphology suggestive of cell death (Figure 1I). This is consistent with the established ability of DNA to induce pyroptosis when sensed by the cytosolic innate immune sensor, absent in melanoma 2 (AIM2)<sup>113</sup>. To enable quantitation, we subtracted successive gray scale DIC images to create a differential DIC signal that increased rapidly and then dropped to levels below baseline at the time of morphologic cell death. By comparing the timing of reporter fluorescence and differential DIC signals for each macrophage, we find that calcium overload is followed closely by cell death (Figures 3.1J and 3.1K).

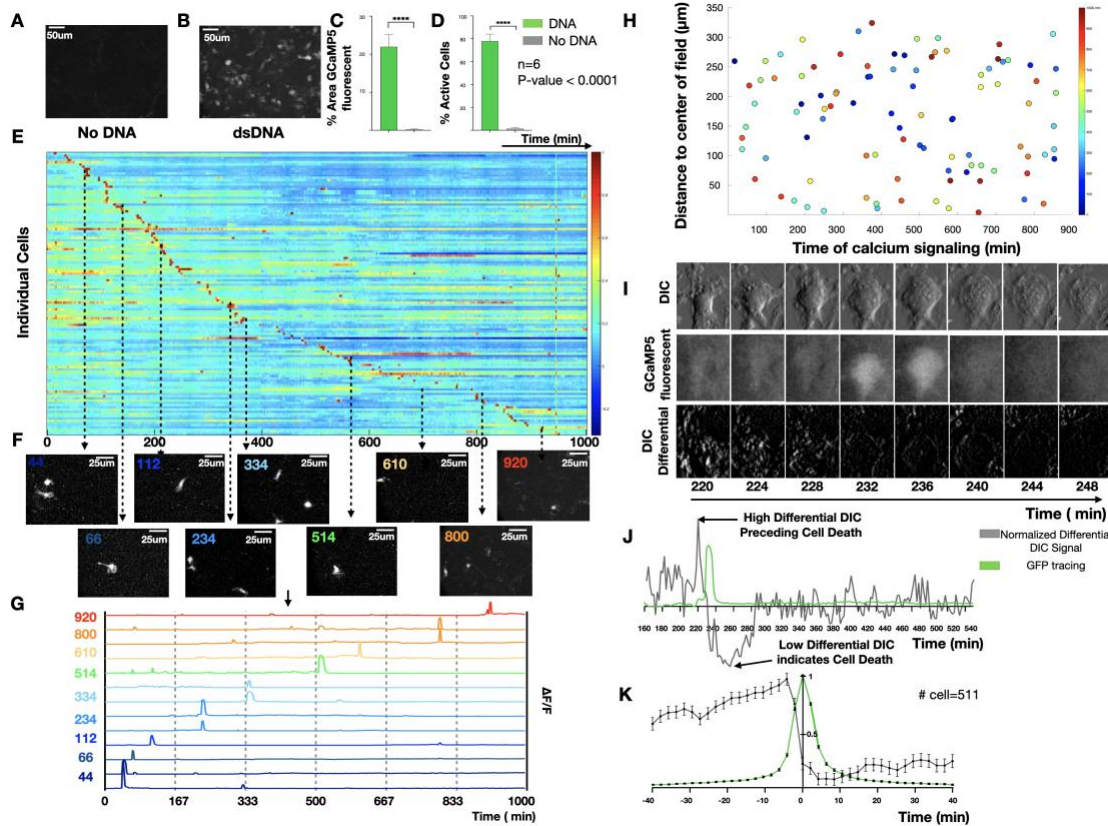


**Figure 4. 1 Calcium reporter macrophages reveal the dynamics of fatal DNA-induced calcium overload**

(A and B) BMDMs were exposed to immune-stimulatory dsDNA or vehicle control and live cell imaging was performed to quantify the resulting calcium signals every 2 min for 16 h. MIPs of representative time-lapse images for (A) no DNA compared with (B) dsDNA. (C and D) (C) Quantification of percentage of GCaMP signaling area and (D) percentage of active cells comparing no DNA with DNA (n = 6). (E) Heatmap of normalized calcium fluorescence versus time for each single cell over 16 h. (F) Example images at discrete time points illustrating asynchronous transient calcium reporter fluorescence. (G) Quantification of the fluorescence dynamics of the cells shown in (F). (H) Spatial location of single cells with color indicating the timing of cellular calcium-dependent fluorescence calcium elevations. (I) DIC (top), GFP (middle), and differential DIC (bottom) surrounding a single calcium overload event. (J) Example quantification of normalized differential DIC signal (gray) with low differential DIC indicating a lack of cell movement suggesting cell death. (K) Stereotyped dynamics of differential DIC signals (gray) and calcium-dependent fluorescence (green) surrounding each calcium overload event (n = 511).

#### 4.3.3: Macrophage cell communication is induced by fatal DNA sensing

The effects of cell death on neighboring cells are difficult to visualize in live cells and are incompletely understood. In contrast to soluble stimuli, which uniformly affect all cells,

complexed dsDNA is particulate in nature and causes asynchronous cell death in directly affected macrophages, which allows surviving neighbor cells to be interrogated for evidence of cell communication. To study neighboring cell responses to DNA-induced cell death, we used scanning confocal microscopy and performed higher-frequency longitudinal calcium reporter imaging at 2 Hz, which we confirmed did not undersample the observed calcium responses. As above, macrophages exhibited rare spontaneous calcium elevations at steady state but exhibited prominent calcium overload in response to DNA stimulation. We noticed that bystander macrophages neighboring the calcium-overloaded cell exhibited fluorescence fluctuations. Therefore, we tested whether bystander signals were the result of cell communication that could be inferred from correlated single-cell calcium dynamics.

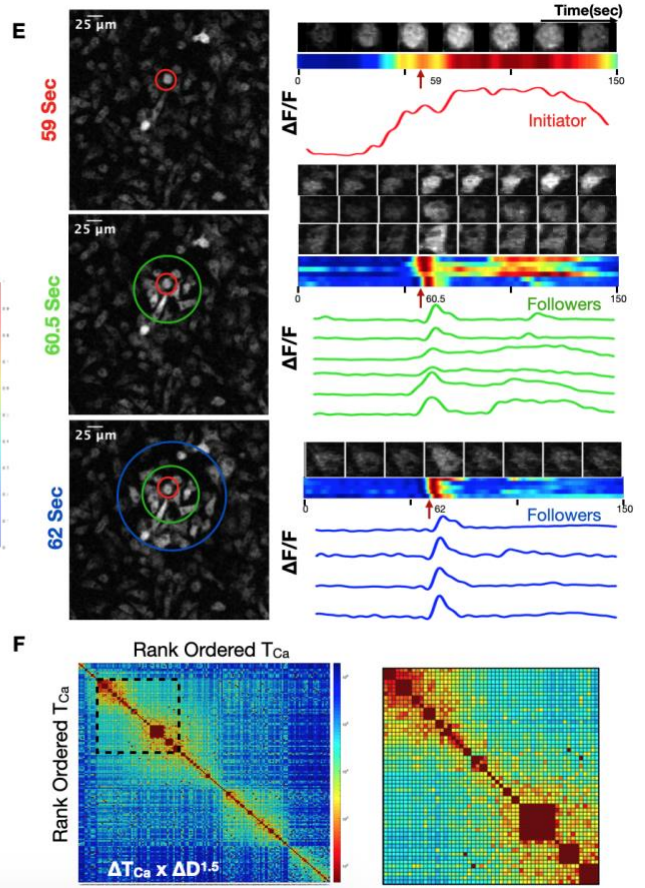
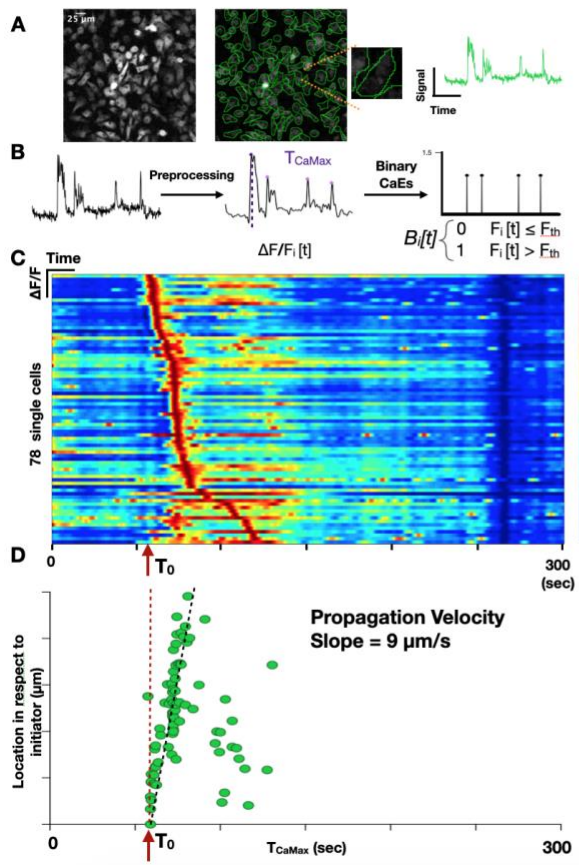
We developed a computational pipeline that converts raw time-lapse fluorescence images into single-cell impulse trains, where each impulse represents the timing of a calcium elevation ( $T_{Ca}$ ). Briefly, single-cell regions of interest (ROIs) were defined and background-corrected to yield a collection of single-cell fluorescence time series that could be low pass filtered and subjected to a peak-finding algorithm. Peaks were transformed into binary impulses at each  $T_{Ca}$ . Cells were sorted based on the timing of their maximum amplitude calcium elevation  $T_{CaMax}$  and plotted as a heatmap of single-cell calcium dynamics. This revealed a temporal progression of calcium elevations suggestive of intercellular signal propagation (Figure 4.5C).

Using the initial calcium-overloaded cell as a reference ( $T_0$ ), we plotted  $T_{CaMax}$  for each cell versus its distance from the initiating cell and revealed a propagation velocity of 9 mm/s, which is consistent with previously reported propagation velocity for intercellular calcium relays<sup>114,115</sup>. Inspection of the time-lapse images confirmed that the isolated calcium-overloaded cell

precipitates a wave of transient calcium elevations in neighboring cells (Figure 4.5E). Cross-correlations of temporally ordered calcium elevations from the entire time-lapse recording also predicted communication with similar timing (Figure 4.5F). Taken together, these data suggest that DNA induced macrophage cell death is rapidly communicated to neighboring cells, where it precipitates non-fatal calcium dynamics.

## Figure 4. 2 Macrophage DNA sensing induces cell communication in vitro

(A) Maximum image projection of BMDMs derived from the Csf1r-GCaMP5 calcium reporter mouse (left). ROIs are drawn to define cell boundaries (middle). Individual cell with corresponding single-cell fluorescence versus time tracing sampled at 2 Hz (right). (B) Signal processing, including background correction, calcium intensity changes quantification, bandpass filtering, peak-finding, and determination of time of maximum calcium elevation ( $\text{TOCaE}_{\text{Max\_CaEs}}$ ) based on the magnitude of calcium intensity and converting the fluorescence peaks into impulses at the time of calcium elevation (TOCaE). Signal processing to define calcium elevation times and convert to a binary impulse train. (C) Heatmap of single cells (y axis) versus time where intensity represents normalized change in fluorescence  $\Delta F/F$ . The time of the initiating cell calcium elevation is defined as  $T_0$ . (D) Distance of cell from the initiating cell versus time of maximum calcium elevation intensity. This reveals a slope of 9 mm/s, which is interpreted as the communication propagation velocity. (E) Frames of the time-lapse fluorescence during the propagation are shown at 59 s, 60.5 s, and 62 s (left). Color-coded concentric rings are shown to define the initiator cell, exhibiting sustained fluorescence (red), and the secondary responders (green and blue concentric rings), exhibiting brief calcium elevations. At right, time-lapse montage of individual cell calcium elevations are shown with the corresponding heatmap and fluorescence versus time tracing. (F) Cross-correlation heatmap of rank-ordered calcium elevations for all cells. Color represents the product of calcium elevation time difference and Euclidean spatial distance  $\Delta \text{TOCaE} \times \Delta D^{1.5}$ . Inset shows the region of high cross-correlation indicating calcium elevations that are highly localized in time and space.

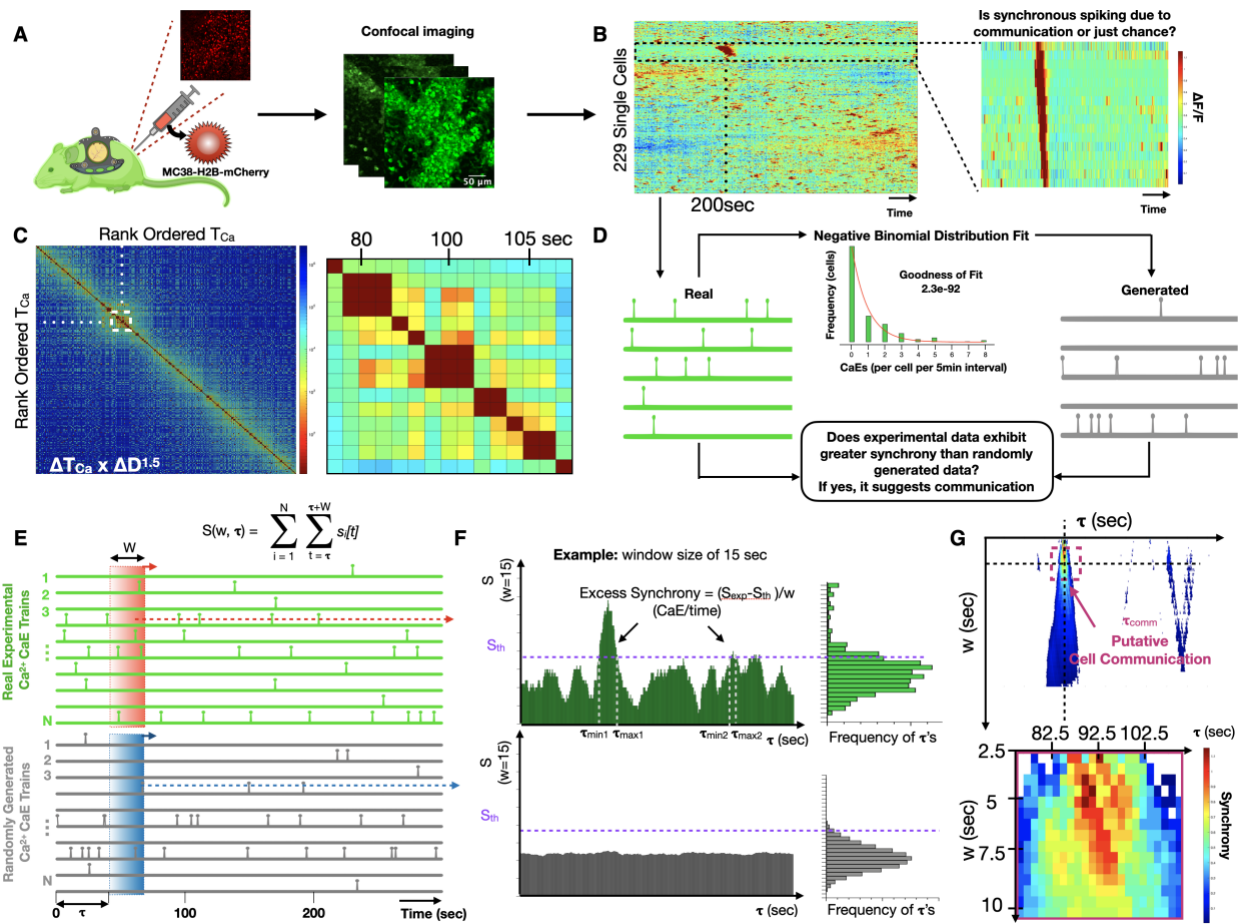


#### **4.3.4: Inference of cell communication from $Csf1r^{Cre}GCaMP5^{fl}$ reporter dynamics in vivo**

Next, we asked whether the calcium reporter could infer cell communication in the complex and dynamic tissue microenvironments in vivo. To facilitate in vivo imaging, we installed a dorsal window chamber in the  $Csf1r^{Cre}GCaMP5^{fl}$  reporter mouse and performed time-lapse imaging (Figure 4.3A) <sup>98</sup>. We implanted 1 million MC38-H2B-mCherry colon adenocarcinoma cells into the tissue underlying the window chamber to facilitate host immune cell recruitment. Within 24–72 h of MC38-H2B-mCherry cell implantation, we discovered host  $Csf1r^{Cre}GCaMP5^{fl}$  reporter cells with highly dynamic calcium elevations. We defined ROIs and quantified each single cell fluorescence across time. Heatmaps were then created by hierarchically clustering the single-cell dynamics. This revealed cells with synchronous calcium elevations amid a background of seemingly random calcium elevations, suggesting possible cell communication (Figure 4.3B). Cross-correlations of temporally ordered calcium elevations revealed similar timing and duration of synchronous calcium elevations (Figure 4.3C). We therefore set out to determine if the observed synchrony was best explained by cell communication.

**Figure 4. 3 Csf1r-GCaMP5 reporter cell communication in vivo revealed by intravital imaging through a dorsal window chamber**

(A) Cartoon illustration of the intravital imaging of a calcium reporter mouse with a dorsal window chamber and orthotopically injected MC38-H2B-mCherry tumor cells. (B) Heatmap of single-cell fluorescence dynamics hierarchically clustered with single cells (y axis) versus time (x axis) where color represents the normalized change in fluorescence  $\Delta F/F$ . Inset shows a cluster of cells with temporally localized calcium elevations. (C) Cross-correlation heatmap of rank-ordered calcium elevations for all cells. Color represents the product of calcium elevation time difference and Euclidean spatial distance  $\Delta T O C a E \times \Delta D^{1.5}$ . Inset shows the region of high cross-correlation indicating calcium elevations that are highly localized in time and space. (D) Strategy for constructing generated (simulated) cells sampled from the same negative binomial distribution of calcium elevation trains as the “real” experimental calcium elevation trains. Comparisons allow estimation of whether synchrony occurs by chance or exhibits excess synchrony, beyond chance, which we interpret as putative cell communication. (E) Method for quantifying normalized number of calcium elevations ( $S/w$ ), also known as synchrony, for real and generated single-cell calcium elevation trains, where  $S$  is a function of temporal window size,  $w$ , and window initiation time,  $\tau$ . (F) Method for defining the timing of excess synchrony of real cell populations compared with the corresponding generated populations. (G) Heatmap of excess synchrony ( $\Delta S/w$ ) as a function of temporal window size,  $w$ , and window initiation time,  $\tau$ . Inset shows timing of high excess synchrony and putative cell communication.



#### 4.3.5: Excess synchrony: A metric for identifying cell communication events in vivo

To determine whether correlated calcium elevations are due to cell communication or if they can be explained simply by chance, we defined a metric called excess synchrony. The metric quantifies the extent to which calcium elevations in a specific window of time exceed randomly generated calcium elevations sampled from a statistically comparable population of cells. We first used the experimental data to assemble the overall distribution of calcium elevation frequencies (calcium elevations per 5-min recording) and modeled it as a negative binomial. Next, we sampled from the distribution to create a “generated” population of synthetic cells (Figure 4.3D). Synchrony was then defined as the number of calcium elevations ( $S$ ) within a defined region of time ( $\tau$ ). Excess synchrony was defined as  $(\Delta S / w = (S_{\text{exp}} - S_{\text{th}}) / w)$ , where  $\Delta S$  was the difference between the amount of experimentally observed synchrony ( $S_{\text{exp}}$ ) and a threshold of generated synchrony ( $S_{\text{th}}$ ) chosen to emphasize specificity over sensitivity, and where  $w$  was the window of time within which calcium elevations are deemed synchronous (Figure 4.3E). At the extremes of large and small window sizes, random calcium elevations dominate and  $\Delta S$  approaches zero; however, at an optimal window size ( $w_{\text{opt}}$ ), a putative cell communication process creates a local maximum of excess synchrony ( $\Delta S / w$ ) due to temporally concentrated calcium elevations that exceed the synchrony predicted by generated cells (Figure 4.3F). To identify cell communication events, we plotted a heatmap of excess synchrony as a function of window size and time. We threshold it at the 80<sup>th</sup> percentile to balance sensitivity and specificity. We then inferred communication events, defining the duration of communication to be the window size at which with most contiguous time points were above threshold and the timing of communication ( $\tau_{\text{comm}}$ ) to be the midpoint of time points above threshold (Figure 4.3G).

To validate the predictions, we examined the spatial distribution of synchronous cells at time  $t$  and observed two qualitative groups, one that was highly localized in space and one that was dispersed (Figure 4.4A). We separated these populations using unsupervised k-means clustering of Euclidean distances (Figure 4.4B). Heatmaps of normalized fluorescence dynamics showed that localized cells from cluster 1 only had calcium elevations one or two times during the recording, whereas spatially dispersed cells from cluster 2 exhibited calcium elevations more frequently and were likely the cells that appeared synchronous by chance, as predicted above (Figures 4.4C–4.4D). Inspection of the time-lapse images confirmed these predictions, as it showed organized waves of calcium fluorescence propagation in cluster 1 but no qualitative evidence of communication in cluster 2 (Figures 4.4E–4.4G). Cluster 1 also exhibited different calcium elevation character with significantly higher calcium fluorescence fullwidth half-maximum (FWHM) and relative calcium elevation amplitude ( $\Delta F/F$ ) (Figures 4.4H–4.4K). Together, these data demonstrate that excess synchrony can be used to identify cell communication events in vivo amid a background of random calcium elevations.

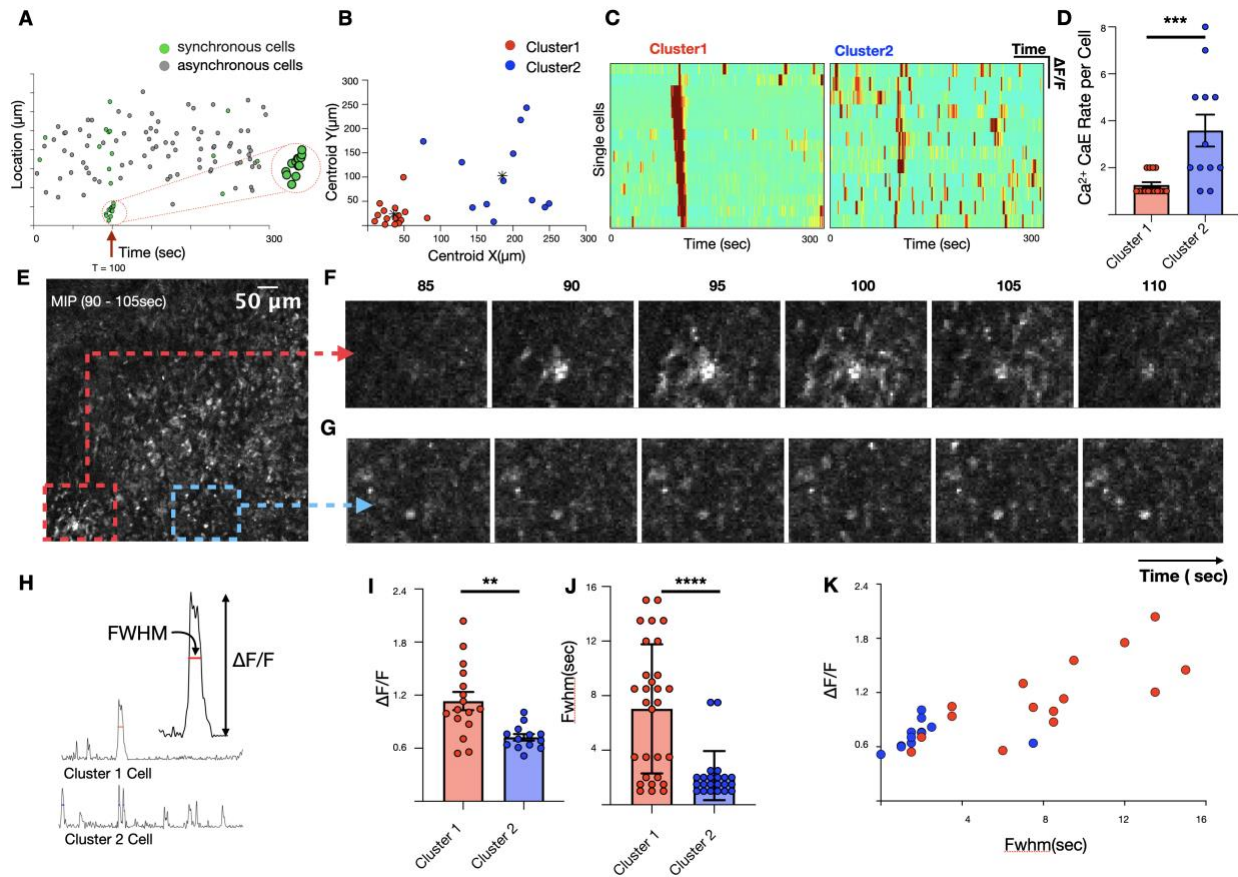


**Figure 4. 4 Characterization of spatiotemporally synchronous cells**

(A) Correlation between location and timing of individual cells and calcium elevation during synchrony event. (B) Unsupervised k-mean clustering based on Euclidean distances reveals two categorical clusters of synchronous cells: those that are spatially localized (red) and those that are disperse (blue). (C) Heatmap of single-cell fluorescence dynamics for clusters 1 and 2. (D) Comparison of single-cell calcium elevation rate for clusters 1 and 2. Error bars represent standard deviations (unpaired t test,  $p < 0.001$ ). (E) MIP spanning the time of high excess synchronicity (90–105 s). (F and G) Localized region containing cluster 1 cells (F) compared with comparable-sized region (G). (H and K) Comparison of normalized calcium-dependent fluorescence changes ( $\Delta F/F$ ) and FWHM of clusters 1 and 2. Error bars represent standard deviations (Unpaired t test,  $p = 0.002$  for I,  $p < 0.001$  for J)

#### 4.3.6: Prediction of spatiotemporal cell communication and regulation in a tumor context in vivo

To enable quantification of reporter fluorescence and inference of putative cell communication in dense communities of reporter cells, we expanded the temporal synchrony

pipeline to add spatial resolution. A maximum image intensity plot of an example recording is shown (Figure 4.5A). In this dataset, the dynamics of 522 single cells were quantified using the pipeline above and displayed as a heatmap. We spatially subset the field into 50 mm x 50 mm sub-images with 25-mm overlap to identify local areas of excess synchrony. This resulted in a 3D volume of excess synchrony versus space and time (Figure 4.5C), which enabled identification, localization, and counting of cell communication events at different levels of stringency. Slices from the volume at locations of excess synchrony are shown as a function of space (Figures 4.5D and 4.5E), as a function of time (Figures 4.5F and 4.5G), and as a kymograph in space-time (Figures 4.5H and 4.5I). We repeated the analysis for several temporal window sizes and synchrony stringencies to show how predicted cell communication events would vary (Figure 4.5J). The resulting self-similar curves revealed peaks of synchrony when the window size approximated the characteristic timescale of cell communication. Increasing the stringency by increase the synchrony threshold led to fewer but more prominent cell communication events, as expected. Finally, we compactly displayed the predicted communication events by color-encoding synchrony events on a spatial map which facilitated comparisons to the underlying fluorescence time-series data (Figure 4.5K).

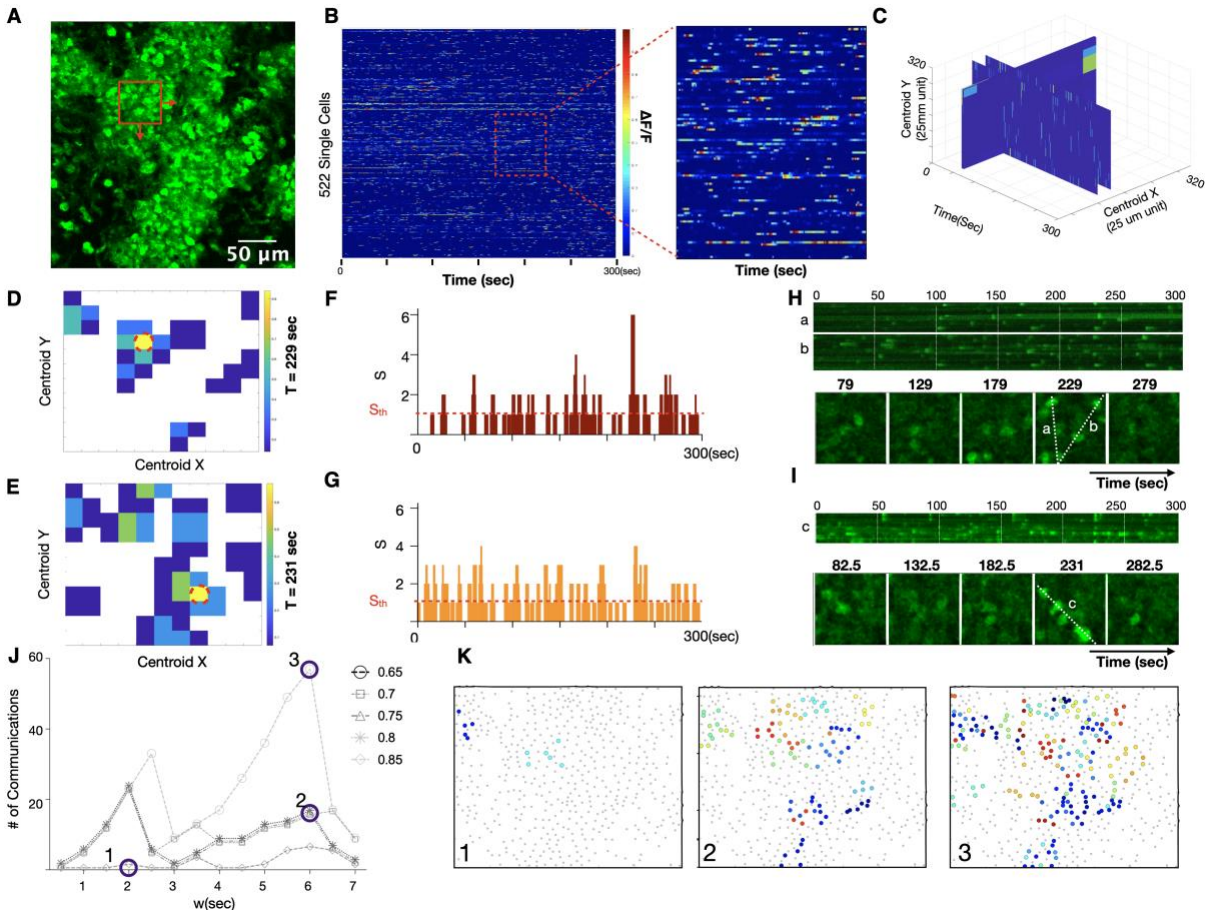


**Figure 4.5 Quantification of excess synchrony and inference of communication in highly dynamic in vivo microenvironments**

(A) MIP of highly dynamic cellular population in vivo. Scale bar, 80  $\mu$ m. (B) Heatmap of 522 single-cell calcium fluorescence dynamics versus time. Color represents normalized calcium-dependent fluorescence changes  $\Delta F/F$ . Inset shows close-up of individual cells. (C) Spatiotemporal calcium dynamics as a volume of 50 mm  $\times$  50 mm regions shifted by 25-mm increments in the x and y directions over the 300-s (600-sample) time-lapse recording. (D and E) Two time points where excess synchrony is calculated versus x and y locations. The red dotted circle indicates the location of the highest excess synchrony. (F and G) Number of calcium elevations ( $S$ ) versus time for the high synchrony locations circled red in (D) and (E). The threshold for treating  $S$  as excess synchrony and considering it a putative cell communication event is shown as a red horizontal dotted line. This line can be increased to create a more stringent threshold for interpreting synchrony as putative cell communication. (H and I) Line scans (top) and montage of individual time frames (bottom) for the locations circled red in (D) and (E). (J) Number of inferred communication events as a function of temporal window size and synchrony stringency. (K) Locations of communication events at different window sizes and synchrony stringency. Color indicates the timing of peak communication (maximum excess synchrony).

#### 4.4: DISCUSSION

We have constructed and characterized a  $Csf1r^{Cre}GCaMP5^{fl}$  calcium reporter mouse and used it to infer immune cell communication in vitro and in vivo. In vitro, the reporter and the associated analysis pipeline enabled direct visualization of fatal calcium overload precipitated by DNA sensing and rapid non-fatal communication to surviving macrophage neighbors. In vivo, in the context of an MC38-H2B-mCherry tumor, it enabled immune cell communication to be inferred from spatiotemporal analysis of  $Csf1r^{Cre}GCaMP5^{fl}$  calcium elevations. Because cell communication occurs in a background of ambient calcium fluctuations of unknown etiology, we defined a metric termed excess synchrony and an associated computational pipeline to identify putative cell communication events amid random calcium elevations. The tools are highly generalizable and should be applicable to other genetically encoded calcium reporter experiments. Importantly, the inference method involves correlating single-cell calcium dynamics but does not require a priori knowledge of the molecular stimulus, the mediators, or the mechanisms of communication. It is therefore a convenient tool for discovery of communication events. However, once discovered, the inference method can be used to probe mechanism by quantifying how cell communication changes in response to genetic or pharmacologic modulation of candidate mediators. For example, one can use co-cultures, chimeric mice, adoptive transfers, bone marrow transplantation, window chamber cell transplantation, or parabiosis to delineate which cell types and mediators are involved in sending versus receiving signals.

The potential mechanisms underlying the observed cell communication are diverse and span length and time scales as well as target site specificity. For example, gap junction intercellular communication (GJIC) enables rapid contact-dependent exchange of intracellular molecules less than 1 kDa between neighboring cells expressing compatible connexins<sup>96</sup>. GJIC can be controlled

dynamically through modulation of cell contact and channel gating and thus offers a mechanism for creating functional networks with selected cells in a shared microenvironment. Mechanotransduction also provides a mechanism for rapid relay of signals such as stretch and loss of neighbors in scratch assays <sup>94</sup>. At the other extreme, secreted factors such as chemokines, cytokines, and growth factors can be released to travel through the extracellular space through diffusion or convection and target distant cells that express the appropriate cognate receptor <sup>116</sup>.

In our *in vitro* experiments, the *Csf1r*<sup>Cre</sup>*GCaMP5*<sup>fl</sup> reporter enabled real-time visualization of complexed DNA inducing calcium overload and cell death followed by rapid communication to neighboring cells. Although we and others have shown that cytosolic DNA sensing precipitates spread of gap junction permeable cyclic di-nucleotide second messengers after cytosolic DNA sensing <sup>85,86</sup>, we were unable to induce calcium fluctuations with cell-permeable cyclic-di-GMP in our reporter. This suggests communication is mediated by a different highly diffusive mediator, such as ions, metabolites, or other secondary messengers, communicating via the extracellular space, gap junctions, or an intracellular relay system.

In our *in vivo* experiments, the possible mechanisms and mediators are diverse, but can be probed using pharmacologic modulators such as selective ion channels blockers or gap junction inhibitors (e.g., carbenoxolone). In addition, to gain more cell type specificity, it would be valuable to cross the *GCaMP* reporter with more selective Cre-inducing promoter such as *S100a8* for neutrophils or *Cx3cr1* for monocytes and macrophages.

A limitation of our study is that we lack gold standard methods to validate whether correlated dynamics are indeed the result of cell communication. Some of our studies *in vivo* show spatially isolated communication events where propagation of calcium dynamics is evident by inspection. However, in other experiments where calcium reporters are highly dynamic and

densely packed in tissue, it is difficult to confirm. Application of mutual information theory and causal inference may be helpful for determine whether correlated calcium dynamics are cell autonomous or the result of cell-to-cell versus environment-to-cell communication<sup>117-119</sup>.

Finally, at first glance, it may appear to be a weakness that calcium is not unique to a single specific signaling pathway. However, calcium was chosen precisely because it integrates inputs from so many different sources and because it has high bandwidth to reflect dynamic cell states faithfully. Here, we use the calcium reporter to discover where and when immune cells are “talking” but we sacrifice knowledge of the specific stimuli and mediators. This is analogous to watching a film in a foreign language, where one can infer which characters are conversing, when, and where, but the detailed meaning of the conversation is unknown. Nevertheless, this is useful because, once communication events are recognized, they can mechanistically probed, as detailed above.

In conclusion, discovery of cell communication in non-excitabile cells has historically required serendipity or a high degree of suspicion. Here, we introduce a method for discovery through inference of cell communication via correlated intracellular calcium dynamics of genetically encoded calcium reporter cells. We hope that this addition to the immunologist’s toolkit will shed light on as-yet undiscovered cellular conversations.

## **4.5: METHODS**

### **4.5.1: Animals**

Mouse experiments were approved and conducted under the oversight of University of California San Diego Institutional Animal Care and Use Committee (#17144) or approved by the Subcommittee on Animal Research Care at Massachusetts General Hospital. All mice were maintained in a pathogen-free environment.  $Csf1r^{Cre}GCaMP5^{fl}$  calcium reporter mice were created

by breeding “Csf1r-Cre” C57CL/6-Tg(Csf1r-cre)1Mnz/J (The Jackson Laboratory; stock 029306), which expresses Cre recombinase under the regulation of the Csf1r promoter, with “GCaMP5” calcium reporter mice, B6;129S6-Polr2a<sup>Tn(pb-CAG-GCaMP5g,-tdTomato)</sup>Tvrd (The Jackson Laboratory; stock 024477). All Csf1r-expressing cells and their progeny express the GCaMP5 calcium reporter and constitutive tdTomato in a bicistronic fashion<sup>115,119</sup>. Genotyping was performed using Jackson Laboratory recommended methods. Experiments were performed with male reporter mice between 10-20 weeks of age.

#### **4.5.2: Tissue processing**

Peripheral blood for flow cytometric analysis was collected by retro-orbital bleeding using heparinized capillary tubes (BD Diagnostic Systems) and red blood cells were lysed with 1x red blood cell lysis buffer (BioLegend). For organ harvest, mice were perfused through the LV with 10 mL of ice-cold PBS. Hearts, spleen, lung, and kidney were enzymatically digested for 1h under continuous agitation at 37C in 450 U/ml collagenase I, 125 U/ml collagenase XI, 60 U/ml DNase I, and 60 U/mL hyaluronidase (Sigma) and filtered through a 40 mm nylon mesh in FACS buffer. to generate a cell suspension for staining and flow cytometric analysis as previously described<sup>112</sup>. To define the anatomical distribution of Csf1r-Cre-induced reporter cells within solid organs, we cut 1 mm sections with a tissue slicer (Zivic Instruments) and examined the spatial distribution of reporter fluorescence in each tissue using a Nikon STORM super resolution confocal microscope at UCSD.

#### **4.5.3: Flow cytometry**

Isolated cells were stained at 4C in FACS buffer (PBS supplemented with 2.5% bovine serum albumin) with and hematopoietic lineage markers including Ly6G (BioLegend, clone 1A8, 1:600), CD11b (BioLegend, clone M1/70, 1:600) and Ter119 (BioLegend, clone TER-119, 1:600).

This was followed by a second staining for NK1.1 (BioLegend, clone PK 136, 1:600), Thy1(CD90.2, BioLegend, clone 53-2.1 1:600), and Ly6C (BioLegend, clone HK1.4 1:600). Cell suspensions were labeled with DAPI just prior to flow cytometric analysis to allow exclusion of dead cells. Doublets, erythrocytes, and dead cells were excluded by forward scatter, Dapi, and Ter119. Neutrophils were identified as (Ter119<sup>low</sup>/CD11b<sup>high</sup>/Ly6G<sup>high</sup>). Monocytes were identified as (Ly6G<sup>low</sup>/Ter119<sup>low</sup>/CD11b<sup>high</sup>/Ly6-C<sup>high</sup>). NK or T cells were identified as (CD11b<sup>low</sup>/Ly6G<sup>low</sup>/(Nk1.1<sup>high</sup> or CD90.2<sup>high</sup>) respectively. The Cre-induced fraction of each hematopoietic lineage subset was determined based on the fraction that was tdTomato high. Data was acquired by Sony sorter MA900 at UCSD and analyzed with FlowJo software.

#### **4.5.4: Cell culture**

Bone marrow derived macrophages (BMDMs) from the Csf1rCreGCaMP5fl reporter mice were isolated, cultured in 10% FBS 1% Pen/Strep-containing DMEM, and differentiated with addition of 10 ng/mL recombinant m-CSF (Peprotech) (every other day media changes) for a period of 7 days as previously described. 10 mg of immunogenic HT DNA (Invivogen) was complexed with lipofectamine transfection agent (ThermoFisher) in serum free-media and added to 1 million BMDMs in a 6-well multi-well plate with serum- and mCSF-containing media for each experiment.

#### **4.5.5: Time-lapse imaging of calcium reporter dynamics in vitro and in vivo**

Low temporal frequency imaging was performed using an Olympus Vivaview epifluorescence microscope with a sampling interval of 2 minutes. DIC/phase contrast and GFP fluorescence time lapse images were captured before and after stimulation with complexed immunogenic dsDNA. For high frequency time-lapse imaging, we used a Fluoview FV1000 confocal microscope at a scan speed of 2 and sampling interval of 0.5 seconds. Frame sizes are

indicated by scale bars. For intravital imaging, dorsal window chambers were installed in adult male reporter mice (8 to 24 weeks old). After window stabilization, 1 million MC38-H2B-mCherry colon cancer cells were injected into the tissue underlying the window and imaging was performed at serial time points.

#### **4.5.6: Quantitative analysis of epifluorescence imaging**

Maximum intensity projections of fluorescence images were used to define regions of interest (ROIs) for each single cell. For each ROI, calcium fluorescence was quantified across time, normalized to median of fluorescence trace, and expressed as  $\Delta F/F = (F[t] - F[t_{\text{median}}])/F[t_{\text{median}}]$ . Cell viability was quantified based on microscale changes in differential DIC images defined as  $DIC[t] - DIC[t-1]$ . Pixels of each differential DIC image were summed, resulting in a scalar at each time point that reached a minimum that was interpreted as the timing of cell death. Cells were aligned by setting the timing of peak calcium fluorescence to zero.

#### **4.5.7: Inference of Cell Communication from Calcium Reporter Time Lapse Imaging**

All analyses were performed using ImageJ/Fiji and MATLAB(Mathworks). Single cell regions of interest (ROI) were defined using ImageJ/Fiji and single cell fluorescence versus time was extracted for each ROI in all data except Figure 6. Background was corrected using a rolling ball algorithm and average fluorescence was quantified for each ROI across time. Each ROI fluorescence time-series was smoothed using a zero-phase digital low pass infinite filter which strengthens the passband signals with a cutoff of 0.45 Hz half power frequency. Peak-finding was performed and transformed into unit magnitude impulses located at the time of each fluorescence peak and termed the time of calcium elevation ( $T_{Ca}$ ). This allowed construction of a discrete time series calcium elevation train  $S_i[t]$  for each cell  $i$ . Cross correlation plots were generated by rank

ordering all calcium elevations of all cells within an individual movie. For each pair of calcium elevation pairs, we calculated the product of the difference in calcium elevation timing  $\Delta T_{Ca}$  and the Euclidean distance weighted by raising to the 1.5 power ( $\Delta D^{1.5}$ ).

See Chapter 5 for more information on this section.

#### **4.5.8: Spatiotemporal Excess Synchrony pipeline details**

Methods for temporal excess synchrony calculation are detailed in the primary manuscript text. Spatiotemporal synchrony was calculated as  $(\Delta S/w)$  for each  $50\mu\text{m} \times 50\mu\text{m}$  sub-image, containing an average of 11 active ROIs, at moving temporal windows of size  $w$ . Regions of excess synchrony that were connected in either time or space were combined and interpreted as a single cell communication event. Synchrony “stringency” was defined a margin above  $S_{th}$  that would be interpreted as a genuine cell communication. It was expressed as a fraction of  $S_{max}-S_{th}$  for each movie and therefore ranged between 0 and 1.

See Chapter 5 for more information on this section.

#### **4.5.9: Quantification and statistical analysis**

All statistical analyses were conducted with GraphPad Prism software and MATLAB. Data are presented as mean  $\pm$  SEM. Statistical significance was evaluated using the two-sided Mann-Whitney test or Kolmogorov-Smirnov test.  $p$  values less than 0.05 were considered to denote significance.

#### **4.5.10: Data and code availability**

All original code has been deposited at <https://github.com/krking/GCaMP-Communication> and is publicly available (<https://doi.org/10.5281/zenodo.5668359>).

#### **4.6.: ACKNOWLEDGMENT**

Chapter 4 is adapted from **Nika Taghdiri**, David M. Calcagno, Zhenxing Fu, Kenneth Huang, Rainer H. Kohler, Ralph Weissleder, Todd P. Coleman, and Kevin R. King. Macrophage calcium reporter mice reveal immune cell communication in vitro and in vivo. *Cell Methods Report*. **2021**. The dissertation author was the primary author of this paper.

## **CHAPTER 5: Inferring cell communication using single cell calcium spatiotemporal dynamics**

### **5.1: ABSTRACT**

There are a limited number of experimental tools for non-destructively discovering cell communication events *in vitro* and *in vivo*. Here, using tissue-specific genetically encoded calcium indicator (GECI) mice, we describe a protocol to preprocess GECI fluorescence time-series measured by time-lapse imaging or intravital microscopy, detect peaks with single cell resolution, and infer cell communication from the synchrony of single cell calcium transients.

### **5.2: INTRODUCTION**

Conditional calcium reporter mice are created by crossing mice expressing Cre under the transcriptional regulation of a cell type specific promoter (e.g., *Csf1r*-Cre, *Tie2*-Cre, or *Alb*-Cre to target macrophages, endothelial cells, or hepatocytes respectively) with mice expressing a Cre-inducible GECI (e.g., GFP-calmodulin-M13 peptide (GCaMP)).<sup>101</sup> *In vitro* experiments can be performed by isolating, culturing, stimulating, and imaging primary cells in culture. Alternatively, *in vivo* experiments can be performed using disease models and intravital imaging. In this chapter, we describe the computational steps required to transform stacks of time-lapse images with defined single cell ROIs into putative cell communication events based on the spatiotemporal correlations of single cell calcium dynamics.

### **5.3: RESULTS**

#### **5.3.1 Preprocessing of fluorescence time-series image stacks collected from GECI reporter cells**

All analyses were performed using ImageJ/Fiji and MATLAB (Mathworks). The Preprocessing Step takes as input, a stack of fluorescence time-lapse images (\*.tiff) and an

associated ROI file (\*.roi), and generates as output, a list of single cells (one for each ROI) with associated centroids and mean fluorescence time series'. FIJI/ImageJ is first used to subtract background fluorescence from each image by using Median Intensity Projection (MedIP) image, extract centroids, and quantify mean fluorescence time series' for each single cell (ROI). Next, MATLAB is used to calculate differential fluorescence time series, remove cells without transients. (See below)

$$\Delta F/F[t] = (F[t] - F_{\text{med}}) / F_{\text{med}}$$

Specifically, median fluorescent is selected as a reference assumes that cells spend at least 50% at baseline. If this assumption is satisfied, then  $F_{\text{med}}$  will provide a good estimate of cell specific baseline dynamics. If it is only valid during part of the record, one should subset the time series and perform the analysis to derive  $F_{\text{med}}$ . An alternative approach to calculating relative fluorescence is to subtract an estimate of initial fluorescence,  $F_0$ . However, this assumes that cells are not in the midst of a calcium transient at time zero.

Furthermore the pipeline uses *filterDesigner* app. This is an interactive tool used to design and evaluate digital filters, which will be used to smooth the signal using zero-phase digital low pass infinite filter.

### **5.3.2: Peak finding and impulse train determination from $\text{Ca}^{2+}$ GECI time series fluorescence**

Peakfinding was performed using a pipeline created in MATLAB and a function called *findpeaks*. The pipeline asks for inputs such as minimum and maximum magnitude of peaks, minimum and maximum duration of peaks namely *threshold*, *Min peak Height*, *Min distance between peaks*, *Min prominence*, *Min width*, and *Max width*. Optimization of peak-finding parameters is critical because fluorescence kinetics and amplitudes depend on many factors

including cell type, microenvironmental context, and choice of genetically encoded calcium reporter.

Then peaks automatically transformed into unit magnitude impulses located at the time of each fluorescence peak and termed the time of calcium elevation ( $T_{Ca}$ ). This allowed construction of a discrete time series calcium elevation train  $S_i[t]$  for each cell  $i$  (Figure 5.1A).

### **5.3.3: Inference of cell communication pipeline based on “Excess Synchrony” metric**

This step of pipeline infers putative cell communication events from the spatiotemporal synchrony of single cell calcium impulse trains. The strategy is illustrated in Figure 5.2.

For purposes of this pipeline, synchrony,  $S(\mathbf{w}, \boldsymbol{\tau})$ , is defined as the number of impulses within a time window of length  $\mathbf{w}$ , beginning at time  $\boldsymbol{\tau}$ . Synchronous impulses can occur either because of true biological information transfer or simply because of chance.

By first modeling the “chance” component, we can then limit our search for cell communication to those times during which the experimentally observed synchrony exceeds the amount of synchrony expected “by chance”. We call the difference, after normalization to window size, “excess synchrony”,  $\Delta S/\mathbf{w}$ . The reason for normalizing is because synchrony increases monotonically with window size. Normalizing to  $\mathbf{w}$  enables comparison of excess synchrony across different window sizes. To determine the synchrony expected by chance, we model the statistics of experimental impulse trains from “real cells”, fit it to a probability distribution (Figure 5.1B).

Specifically, interactive *distributionFitter* app facilitates a fitting distribution by choosing a list of distribution. Then the pipeline perform a Chi square goodness of fit test using the built-in function *chi2gof* and return a test decision decision for the null hypothesis that the experimental impulse histogram data comes from the specified probability distribution. If the test decision

rejects the null hypothesis at the 5% significance level, the pipeline attempts for another distribution fit. Then the pipeline runs automatically with the assistance of only two input parameters - window size, which determines temporal resolution, and a z-score, which determines the inclusiveness or exclusiveness of communication inference (Figure 5.1 B).

Sample the distribution to create generated impulse trains from “generated cells” having the same statistics. This allows calculation of generated synchrony due to chance alone,  $\mathbf{S}_{\text{gen}}(\mathbf{w}, \boldsymbol{\tau})$ . To convert generated synchrony into a single number that can be easily subtracted from real experimentally observed synchrony,  $\mathbf{S}_{\text{real}}(\mathbf{w}, \boldsymbol{\tau})$ , to calculate excess synchrony, we define a threshold,  $\mathbf{S}_{\text{th}}$ , at a specified percentile of  $\mathbf{S}_{\text{gen}}(\mathbf{w}, \boldsymbol{\tau})$  using a **z score** (Figure 5.1 D-G).

Excess synchrony,  $\Delta\mathbf{S}/\mathbf{w}$ , is then calculated by subtracting  $\mathbf{S}_{\text{real}}(\mathbf{w}, \boldsymbol{\tau})$  and  $\mathbf{S}_{\text{th}}$  and normalizing to  $\mathbf{w}$ . Selection of  $\mathbf{S}_{\text{th}}$  via the choice of z score is a critical step because high  $\mathbf{S}_{\text{th}}$  values will predict few cell communication events but have fewer false positives than low  $\mathbf{S}_{\text{th}}$  values, which will predict more cell communication events but include more false positives (predicted communication where synchrony is actually due to chance alone) (Figure 5.1 H).

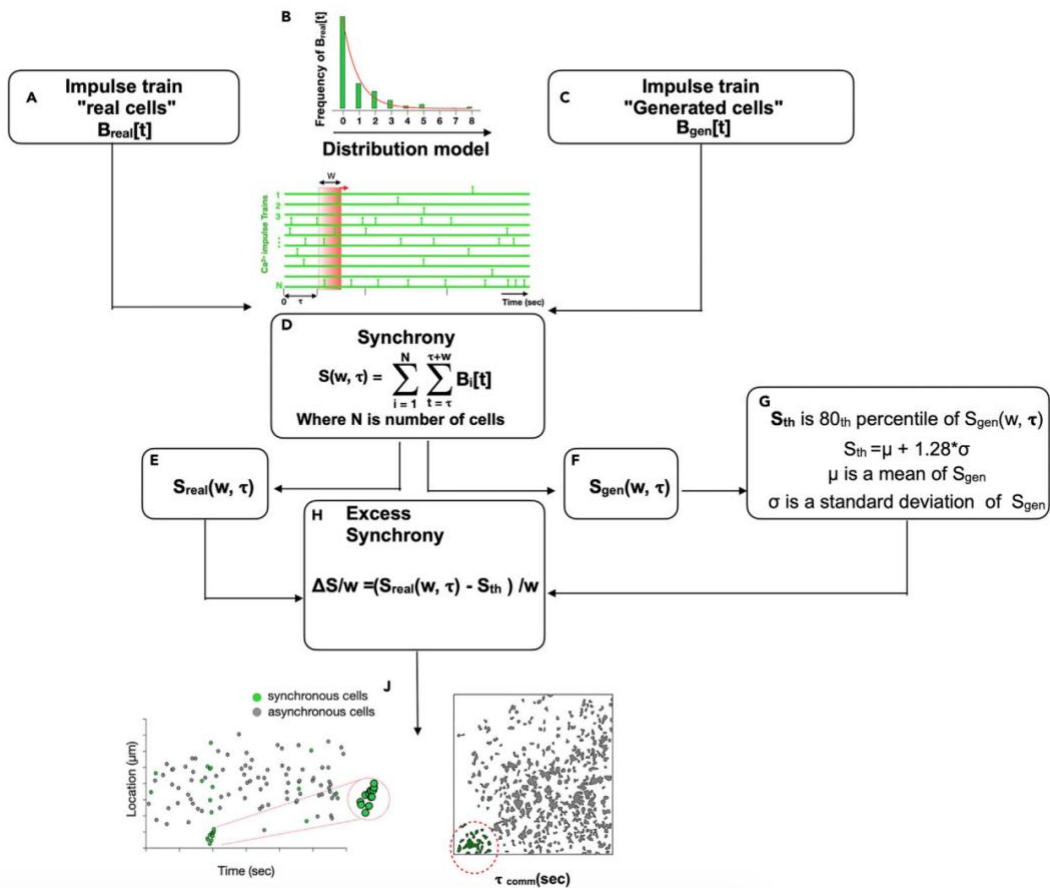


**Figure 5. 1 Diagram of cell communication pipeline inference steps**

(A–C) (A) “Real” experimental binary impulse trains are (B) modeled based on their impulse train statistics to create (C) “generated” binary impulse trains. (D–F) Real and generated impulse trains are independently used to calculate synchrony,  $S(w, \tau)$ , specifically (E,F)  $S_{real}(w, \tau)$  and  $S_{gen}(w, \tau)$ . (G) A threshold called  $S_{th}$  is defined based on generated synchrony and a user-generated z score. (H) Excess synchrony,  $\Delta S/w$ . (J) Cell communication events are identified at time  $\tau_{comm}$ ’s and spatial locations ( $X_{comm}$ ’s,  $Y_{comm}$ ’s).

Optimization of the z score is critical. The default **z score** is set at 1.28, the 80<sup>th</sup> percentile. However,  $S_{th}$  is a tunable parameter, which allows the user to alter the stringency of this threshold. At lower percentiles (lower  $S_{th}$  values), the number of identified peaks will increase, resulting in more predicted events but more false positives (i.e., more synchronous impulses that are labeled communication will actually be due to chance). Conversely, at higher percentiles (higher  $S_{th}$  values), the number of identified peaks will decrease resulting in fewer predicted events but more

risk of false negatives (i.e., missing true communication events). The z score should be optimized to balance the competing goals of maximizing the number of events detected (by lowering the z score) while minimizing the number of false positives (by increasing the z score). In practice, if one has a biologically negative control sample (i.e., few calcium transients per time) one can reduce the z score until an unacceptable number of cell communication events (of which all are considered false positives) are detected (Figure 5.2).

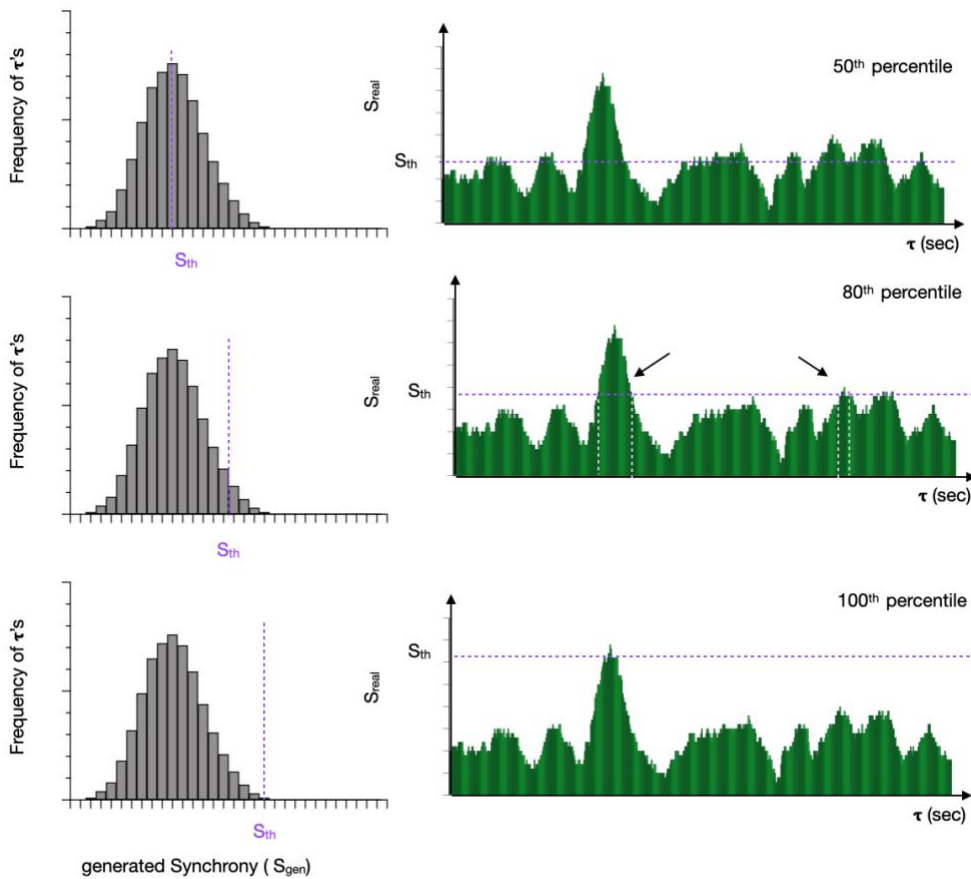


**Figure 5. 2 Example of how varying  $S_{th}$  affects predicted cell communication events**

$S_{th}$  corresponding to the 50<sup>th</sup>, 80<sup>th</sup>, and 100<sup>th</sup> percentiles of  $S_{gen}$  are illustrated. Communication is predicted where  $S_{real}$  exceeds  $S_{th}$ , (e.g., where excess synchrony is greater than zero). The initiation of each putative communication event where  $S_{real}$  sustainably exceeds  $S_{th}$  is deemed a putative communication event assigned to the start time  $\tau_{comm}$ .

To determine the timing of putative cell communication events we derive a vector of communication times  $\mathbf{t}_{\text{comm}}$  by grouping nearby values of  $\mathbf{t}$  for which excess synchrony  $\Delta\mathbf{S}/\mathbf{w}$  is greater than zero. For each  $\mathbf{t}_{\text{comm}}$ , spatial analysis is limited to only those cells with calcium impulses between  $\mathbf{t}_{\text{comm}}$  and  $\mathbf{t}_{\text{comm}} + \mathbf{w}$ . k-Means clustering using *evalclusters* is performed and the centroid of the cluster with the greatest cell density is taken as the location of putative cell communication  $\mathbf{X}_{\text{comm}}$ ,  $\mathbf{Y}_{\text{comm}}$ . The results of putative cell communication events and their component cells are reported.

#### **5.4: Discussion**

This chapter describes an imaging-based method for quantifying single cell calcium reporter responses and inferring cell communication based on “Excess Synchrony”. A computational pipeline analyzes the images and creates a list of putative cell communication events with associated timing, location, and component cells. This can then be studied using genetic or pharmacologic modulators of specific cell communication mechanisms to validate and probe mechanism via perturbation.

This computational pipeline is applicable to fluorescence live cell time series imaging with high cell density. However, a dense and very active population would degrade the confidence to find the high spatiotemporal cells as a putative cell communication using k-Means clustering. A second important limitation is that our method cannot distinguish information transfer between cells from information transfer from the environment to neighboring cells (an external stimulus). An important assumption in the current instantiation is that there is only one event per time point within one field of view. To accommodate cases where the density and frequency of cell communication is high, one can separate the image into sub-images and run the pipeline on each

sub-image. In this way, one can discover simultaneous but spatially distinct cell communication events within the same field of view.

In conclusion, this pipeline is best suited for investigators with basic signal processing and computational experience and who have access to time-lapse fluorescence recordings of cells that are potentially communicating.

### **5.5: Data and code availability**

All original code has been deposited at [https://github.com/Nikatag/inferring\\_cell\\_communication\\_pipeline](https://github.com/Nikatag/inferring_cell_communication_pipeline) and is publicly available. Any additional information required to reanalyze the data reported in this paper is available from the lead contact upon request.

### **5.6: ACKNOWLEDGMENT**

Chapter 5 is adapted from **Nika Taghdiri**, Kevin R. King. Inferring cell communication using single cell calcium spatiotemporal dynamics. STAR protocol. **2022**. The dissertation author was the primary author of this paper.

## 6. CONCLUSION

In this work, we developed methods for isolating single nuclei cardiomyocytes, performing unbiased high throughput single nuclei RNAseq (snRNAseq) and spatial transcriptomics. Our study provides the first comprehensive characterization of the BZ and RZ in the adult mouse heart after subjected to permanent ligation, an *in vivo* MI model. We found that the BZ and RZ exhibit distinct transcriptional signatures that can be revealed by unbiased clustering. To determine the spatial patterning of these CM subsets, we performed grid-based spatial transcriptomics (Visium 10x) and validated with multiplexed RNA fluorescence in situ hybridization (mFISH). Our results reveals that BZ defines in two category, BZ1 (Nppa+Xirp2<sup>-/-</sup>) and BZ2 (Nppa+Xirp2<sup>+/-</sup>). BZ1 (Nppa+Xirp2<sup>-/-</sup>) forms a hundreds-of-microns-thick layer adjacent to RZ and is transitional in space and gene expression, while BZ2 (Nppa+Xirp2<sup>+/-</sup>) forms a tens-of-microns-thick layer at the IZ edge and is a distinct transcriptomes from RZ.

Our work shows the transcriptional BZ emerges within an hour of injury arguing for a direct response by cardiomyocytes rather than an indirect response to infiltrating myeloid cells and activation of fibroblasts. In addition, the characterization of BZ CMs by gene expression encode mechanosensing and mechanotransduction proteins. This prompted us to test whether mechanical injury was sufficient to induce BZ transcriptional profiles. Indeed, spatial transcriptomic profiling in three *in vivo* models (TAC, ISO, and needle pass) as well as qPCR of BZ marker genes following mechanical scratch of cardiomyocyte cultures. Our results suggested that mechanical instability and “loss of neighbor” at the BZ edge are the dominant inducers of the BZ transcriptional response.

Finally, we developed a transgenic tool to provide a non-destructive assay with high temporal resolution for macrophage immune cells.  $Csf1r^{Cre}$  GCAMP5<sup>fl</sup> reporter measures intercellular calcium elevation upon a stimuli *invitro* or *invivo*. Our results showed that the stimulation enabled immune cell communication to be inferred from spatiotemporal analysis of  $Csf1r^{Cre}$ GCaMP5<sup>fl</sup> calcium elevations. Because cell communication occurs in a background of ambient calcium fluctuations of unknown etiology, we created a computational pipeline called ‘Excess synchrony’ to identify putative cell communication events amid random calcium elevations.

A limitation of this study is that we lack gold standard methods to validate whether correlated dynamics are indeed the result of cell communication. Some of our studies *In vivo* show spatially isolated communication events where propagation of calcium dynamics is evident by inspection. However, in other experiments where calcium reporters are highly dynamic and densely packed in tissue, it is difficult to confirm. Application of mutual information theory and causal inference may be helpful for determining whether correlated calcium dynamics are cell autonomous or are the result of cell-to-cell or environment-to-cell communication<sup>117,118</sup>. Finally, at first glance, it may appear to be a weakness that calcium is not unique to a single specific signaling pathway. However, calcium was chosen precisely because it integrates inputs from so many different sources and because it has high bandwidth to reflect dynamic cell states faithfully. Nevertheless, this is useful because, once communication events are recognized, they can mechanistically probed, as detailed above.

Macrophages are critical cells in the host response to MI and impact BZ niches functionally. Although the mechanisms underlying their function are complex and not fully understood, a number of mediators and signaling pathways have been implicated in macrophage

function. With leveraging this toolkit and pharmacologic modulators, such as selective ion channels blockers or gap junction inhibitors, can probe the possible mechanisms and mediators involved and impacted in BZ biology. In addition, to gain more cell type specificity, it would be valuable to cross the GCaMP reporter with more selective Cre-inducing promoters (such as S100a8 for neutrophils or Cx3cr1 for monocytes and macrophages.).

In conclusion, there are still many unanswered questions about the mechanisms underlying ischemic heart disease. In this work, we set out to provide a comprehensive characterization of the borderzone, a microenvironment that is critical for understanding ischemic heart disease. Our study provides important insights in macrophage communication in the context of borderzone, as their functions impact myocardial tissue over the days and weeks following MI. Overall, these applications and results offer a reference dataset for future studies aimed at improving our understanding of and therapeutic approaches to ischemic heart disease, and may be able to shed light on as-yet undiscovered cellular conversations between the BZ and immune niches .

## Supplementary Figure

### Figure S. 1 Integration of single cell and nuclei RNA-seq heart datasets during acute responses to MI

(a) Overall experimental design and integration of sc/snRNAseq data with whole transcriptome spatial data. Hearts were harvest at several time points following experimental MI and collected for snRNA-seq. The resulting data matrices were integrated with available scRNA-seq data. (b) Experimental timepoints post-MI that were examined in our study with a summary table of total numbers of cells, nuclei, and spatial pixels analyzed to support the robustness of our claims across biological replicates (c) UMAP plots annotated by major cell types (left) and subsets (right). (d) UMAP plots displaying composition of single nuclei (left) and single cell (right) derived samples. (e) Subcluster composition as derived from UMAPs shown in (c). (f) UMAP plots split by timepoint and across biological replicates. (g) Average subcluster composition displayed in (f). (h) QC metric of samples and replicates for both single nuclei and single cell represented in counts per sample (nCounts) and features per sample(nGenes).



## REFERENCES

- 1 Derek J Hausenloy , D. M. Y. Ischaemic conditioning and reperfusion injury. *Nature reveiw cardiology* **13**, 193-209 (2016). <https://doi.org/doi:10.1038/nrcardio.2016.5>
- 2 de Bakker, J. M. *et al.* Reentry as a cause of ventricular tachycardia in patients with chronic ischemic heart disease: electrophysiologic and anatomic correlation. *Circulation* **77**, 589-606 (1988). <https://doi.org/10.1161/01.cir.77.3.589>
- 3 Ursell, P. C., Gardner, P. I., Albala, A., Fenoglio, J. J., Jr. & Wit, A. L. Structural and electrophysiological changes in the epicardial border zone of canine myocardial infarcts during infarct healing. *Circ Res* **56**, 436-451 (1985). <https://doi.org/10.1161/01.res.56.3.436>
- 4 Jackson, B. M. *et al.* Extension of borderzone myocardium in postinfarction dilated cardiomyopathy. *Journal of the American College of Cardiology* **40**, 1160-1167; discussion 1168-1171 (2002). [https://doi.org/10.1016/s0735-1097\(02\)02121-6](https://doi.org/10.1016/s0735-1097(02)02121-6)
- 5 Wu, C. C. *et al.* Spatially Resolved Genome-wide Transcriptional Profiling Identifies BMP Signaling as Essential Regulator of Zebrafish Cardiomyocyte Regeneration. *Dev Cell* **36**, 36-49 (2016). <https://doi.org/10.1016/j.devcel.2015.12.010>
- 6 Leach, J. P. *et al.* Hippo pathway deficiency reverses systolic heart failure after infarction. *Nature* **550**, 260-264 (2017). <https://doi.org/10.1038/nature24045>
- 7 Hulsmans, M. *et al.* Macrophages Facilitate Electrical Conduction in the Heart. *Cell* **169**, 510-522 e520 (2017). <https://doi.org/10.1016/j.cell.2017.03.050>
- 8 Abbaci, M., Barberi-Heyob, M., Blondel, W., Guillemin, F. & Didelon, J. Advantages and limitations of commonly used methods to assay the molecular permeability of gap junctional intercellular communication. *BioTechniques* **45**, 33-52, 56-62 (2008). <https://doi.org/10.2144/000112810>
- 9 Nabel EG, B. E. A tale of coronary artery disease and myocardial infarction. *The New England journal of medicine*, 54-63 (2012). <https://doi.org/doi:10.1056/NEJMra1112570>.
- 10 Yu, B., Akushevich, I., Yashkin, A. P. & Kravchenko, J. Epidemiology of Geographic Disparities of Myocardial Infarction Among Older Adults in the United States: Analysis of 2000-2017 Medicare Data. *Front Cardiovasc Med* **8**, 707102 (2021). <https://doi.org/10.3389/fcvm.2021.707102>
- 11 Ramphul, K., Ramphul, Y., Sombans, S., Lohana, P. & Joynauth, J. Acute myocardial infarction admissions among young adults in the United States: an update on the incidence and burden. *Arch Med Sci Atheroscler Dis* **6**, e18-e20 (2021). <https://doi.org/10.5114/amsad.2021.105160>
- 12 Bishu, K. G. *et al.* Estimating the Economic Burden of Acute Myocardial Infarction in the US: 12 Year National Data. *Am J Med Sci* **359**, 257-265 (2020). <https://doi.org/10.1016/j.amjms.2020.02.004>
- 13 Timmers L, P. G., de Hoog VC, Arslan F, Appelman Y, de Kleijn DP. The innate immune response in reperfused myocardium. . *Cardiovascular research* **94(2)**, 276-283 (2012). <https://doi.org/doi:10.1093/cvr/cvs018>
- 14 Arslan F, d. K. D., Pasterkamp G. Innate immune signaling in cardiac ischemia. *Nature reviews Cardiology* **8(5)**, 292-300 (2011). <https://doi.org/doi:10.1038/nrcardio.2011.38>
- 15 Tang D, K. R., Coyne CB, Zeh HJ, Lotze MT. PAMPs and DAMPs: signal 0s that spur autophagy and immunity. . *Immunological reviews* **249(1)**, 158-175 (2012). <https://doi.org/doi:10.1111/j.1600-065X.2012.01146.x>

- 16 King, K. R. *et al.* IRF3 and type I interferons fuel a fatal response to myocardial infarction. *Nat Med* **23**, 1481-1487 (2017). <https://doi.org:10.1038/nm.4428>
- 17 Factor, S. M., Sonnenblick, E. H. & Kirk, E. S. The histologic border zone of acute myocardial infarction--islands or peninsulas? *The American journal of pathology* **92**, 111-124 (1978).
- 18 Janse, M. J. *et al.* The "border zone" in myocardial ischemia. An electrophysiological, metabolic, and histochemical correlation in the pig heart. *Circ Res* **44**, 576-588 (1979). <https://doi.org:10.1161/01.res.44.4.576>
- 19 van Duijvenboden, K. *et al.* Conserved NPPB+ Border Zone Switches From MEF2- to AP-1-Driven Gene Program. *Circulation* **140**, 864-879 (2019). <https://doi.org:10.1161/CIRCULATIONAHA.118.038944>
- 20 Vivien, C. J., Hudson, J. E. & Porrello, E. R. Evolution, comparative biology and ontogeny of vertebrate heart regeneration. *NPJ Regen Med* **1**, 16012 (2016). <https://doi.org:10.1038/npjregenmed.2016.12>
- 21 Smith, R. M., Black, A. J., Velamakanni, S. S., Akkin, T. & Tolkacheva, E. G. Visualizing the complex 3D geometry of the perfusion border zone in isolated rabbit heart. *Applied optics* **51**, 2713-2721 (2012). <https://doi.org:10.1364/AO.51.002713>
- 22 Pirolo, J. S., Hutchins, G. M. & Moore, G. W. Infarct expansion: pathologic analysis of 204 patients with a single myocardial infarct. *Journal of the American College of Cardiology* **7**, 349-354 (1986).
- 23 Erlebacher, J. A., Richter, R. C., Alonso, D. R., Devereux, R. B. & Gay, W. A., Jr. Early infarct expansion: structural or functional? *Journal of the American College of Cardiology* **6**, 839-844 (1985).
- 24 Gao, X. M., Xu, Q., Kiriazis, H., Dart, A. M. & Du, X. J. Mouse model of post-infarct ventricular rupture: time course, strain- and gender-dependency, tensile strength, and histopathology. *Cardiovasc Res* **65**, 469-477 (2005). <https://doi.org:10.1016/j.cardiores.2004.10.014>
- 25 Mounier-Vehier, F. *et al.* Borderzone infarct subtypes: preliminary study of the presumed mechanism. *Eur Neurol* **34**, 11-15 (1994). <https://doi.org:10.1159/000117001>
- 26 Wetstein, L., Michelson, E. L., Simson, M. B., Moore, E. N. & Harken, A. H. Increased normoxic-to-ischemic tissue borderzone as the cause for reentrant ventricular tachyarrhythmias. *J Surg Res* **32**, 526-534 (1982). [https://doi.org:10.1016/0022-4804\(82\)90135-4](https://doi.org:10.1016/0022-4804(82)90135-4)
- 27 Hearse, D. J. & Yellon, D. M. The "Border zone" and myocardial protection: a time for reassessment? *Acta Med Scand Suppl* **651**, 37-46 (1981).
- 28 Duncanson, E. R. & Mackey-Bojack, S. M. Histologic Examination of the Heart in the Forensic Autopsy. *Acad Forensic Pathol* **8**, 565-615 (2018). <https://doi.org:10.1177/1925362118797736>
- 29 Yang, Y. *et al.* Age-related differences in postinfarct left ventricular rupture and remodeling. *Am J Physiol Heart Circ Physiol* **294**, H1815-1822 (2008). <https://doi.org:10.1152/ajpheart.00831.2007>
- 30 Cavasin, M. A., Tao, Z., Menon, S. & Yang, X. P. Gender differences in cardiac function during early remodeling after acute myocardial infarction in mice. *Life sciences* **75**, 2181-2192 (2004). <https://doi.org:10.1016/j.lfs.2004.04.024>

- 31 Tsao, C. W. *et al.* Heart Disease and Stroke Statistics-2022 Update: A Report From the American Heart Association. *Circulation* **145**, e153-e639 (2022). <https://doi.org:10.1161/CIR.0000000000001052>
- 32 von Lueder, T. G., Kotecha, D., Atar, D. & Hopper, I. Neurohormonal Blockade in Heart Failure. *Card Fail Rev* **3**, 19-24 (2017). <https://doi.org:10.15420/cfr.2016:22:2>
- 33 Aizarani, N. *et al.* A human liver cell atlas reveals heterogeneity and epithelial progenitors. *Nature* **572**, 199-204 (2019). <https://doi.org:10.1038/s41586-019-1373-2>
- 34 Bahar Halpern, K. *et al.* Single-cell spatial reconstruction reveals global division of labour in the mammalian liver. *Nature* **542**, 352-356 (2017). <https://doi.org:10.1038/nature21065>
- 35 Calcagno, D. M. *et al.* The myeloid type I interferon response to myocardial infarction begins in bone marrow and is regulated by Nrf2-activated macrophages. *Sci Immunol* **5** (2020). <https://doi.org:10.1126/sciimmunol.aaz1974>
- 36 Calcagno, D. M. *et al.* SiglecF(HI) Marks Late-Stage Neutrophils of the Infarcted Heart: A Single-Cell Transcriptomic Analysis of Neutrophil Diversification. *Journal of the American Heart Association* **10**, e019019 (2021). <https://doi.org:10.1161/JAHA.120.019019>
- 37 Dick, S. A. *et al.* Self-renewing resident cardiac macrophages limit adverse remodeling following myocardial infarction. *Nature immunology* **20**, 29-39 (2019). <https://doi.org:10.1038/s41590-018-0272-2>
- 38 Forte, E. *et al.* Dynamic Interstitial Cell Response during Myocardial Infarction Predicts Resilience to Rupture in Genetically Diverse Mice. *Cell reports* **30**, 3149-3163 e3146 (2020). <https://doi.org:10.1016/j.celrep.2020.02.008>
- 39 Hu, P. *et al.* Single-nucleus transcriptomic survey of cell diversity and functional maturation in postnatal mammalian hearts. *Genes Dev* **32**, 1344-1357 (2018). <https://doi.org:10.1101/gad.316802.118>
- 40 Martini, E. *et al.* Single-Cell Sequencing of Mouse Heart Immune Infiltrate in Pressure Overload-Driven Heart Failure Reveals Extent of Immune Activation. *Circulation* **140**, 2089-2107 (2019). <https://doi.org:10.1161/CIRCULATIONAHA.119.041694>
- 41 Ren, Z. *et al.* Single-Cell Reconstruction of Progression Trajectory Reveals Intervention Principles in Pathological Cardiac Hypertrophy. *Circulation* **141**, 1704-1719 (2020). <https://doi.org:10.1161/CIRCULATIONAHA.119.043053>
- 42 Tucker, N. R. *et al.* Transcriptional and Cellular Diversity of the Human Heart. *Circulation* **142**, 466-482 (2020). <https://doi.org:10.1161/CIRCULATIONAHA.119.045401>
- 43 Wang, Z. *et al.* Cell-Type-Specific Gene Regulatory Networks Underlying Murine Neonatal Heart Regeneration at Single-Cell Resolution. *Cell reports* **33**, 108472 (2020). <https://doi.org:10.1016/j.celrep.2020.108472>
- 44 Cui, M. *et al.* Dynamic Transcriptional Responses to Injury of Regenerative and Non-regenerative Cardiomyocytes Revealed by Single-Nucleus RNA Sequencing. *Dev Cell* **53**, 102-116 e108 (2020). <https://doi.org:10.1016/j.devcel.2020.02.019>
- 45 Kuppe, C. *et al.* Spatial multi-omic map of human myocardial infarction. *Nature* (2022). <https://doi.org:10.1038/s41586-022-05060-x>
- 46 Heinz, S. *et al.* Simple combinations of lineage-determining transcription factors prime cis-regulatory elements required for macrophage and B cell identities. *Molecular cell* **38**, 576-589 (2010). <https://doi.org:10.1016/j.molcel.2010.05.004>
- 47 Sinn, H. W., Balsamo, J., Lilien, J. & Lin, J. J. Localization of the novel Xin protein to the adherens junction complex in cardiac and skeletal muscle during development.

- Developmental dynamics : an official publication of the American Association of Anatomists* **225**, 1-13 (2002). <https://doi.org:10.1002/dvdy.10131>
- 48 Gustafson-Wagner, E. A. *et al.* Loss of mXinalpha, an intercalated disk protein, results in cardiac hypertrophy and cardiomyopathy with conduction defects. *Am J Physiol Heart Circ Physiol* **293**, H2680-2692 (2007). <https://doi.org:10.1152/ajpheart.00806.2007>
- 49 Long, P. A., Larsen, B. T., Evans, J. M. & Olson, T. M. Exome Sequencing Identifies Pathogenic and Modifier Mutations in a Child With Sporadic Dilated Cardiomyopathy. *Journal of the American Heart Association* **4** (2015). <https://doi.org:10.1161/JAHA.115.002443>
- 50 Huang, Y. S., Xing, Y. L. & Li, H. W. Heterozygous desmin gene (DES) mutation contributes to familial dilated cardiomyopathy. *The Journal of international medical research* **49**, 3000605211006598 (2021). <https://doi.org:10.1177/03000605211006598>
- 51 McCalmon, S. A. *et al.* Modulation of angiotensin II-mediated cardiac remodeling by the MEF2A target gene Xirp2. *Circ Res* **106**, 952-960 (2010). <https://doi.org:10.1161/CIRCRESAHA.109.209007>
- 52 Verdonschot, J. A. J. *et al.* A mutation update for the FLNC gene in myopathies and cardiomyopathies. *Hum Mutat* **41**, 1091-1111 (2020). <https://doi.org:10.1002/humu.24004>
- 53 Ortiz-Genga, M. F. *et al.* Truncating FLNC Mutations Are Associated With High-Risk Dilated and Arrhythmogenic Cardiomyopathies. *Journal of the American College of Cardiology* **68**, 2440-2451 (2016). <https://doi.org:10.1016/j.jacc.2016.09.927>
- 54 Hall, C. L. *et al.* Filamin C variants are associated with a distinctive clinical and immunohistochemical arrhythmogenic cardiomyopathy phenotype. *International journal of cardiology* **307**, 101-108 (2020). <https://doi.org:10.1016/j.ijcard.2019.09.048>
- 55 Oz, S. *et al.* Reduction in Filamin C transcript is associated with arrhythmogenic cardiomyopathy in Ashkenazi Jews. *International journal of cardiology* **317**, 133-138 (2020). <https://doi.org:10.1016/j.ijcard.2020.04.005>
- 56 Begay, R. L. *et al.* Filamin C Truncation Mutations Are Associated With Arrhythmogenic Dilated Cardiomyopathy and Changes in the Cell-Cell Adhesion Structures. *JACC Clin Electrophysiol* **4**, 504-514 (2018). <https://doi.org:10.1016/j.jacep.2017.12.003>
- 57 Valdes-Mas, R. *et al.* Mutations in filamin C cause a new form of familial hypertrophic cardiomyopathy. *Nature communications* **5**, 5326 (2014). <https://doi.org:10.1038/ncomms6326>
- 58 Gunthel, M. *et al.* Epigenetic State Changes Underlie Metabolic Switch in Mouse Post-Infarction Border Zone Cardiomyocytes. *J Cardiovasc Dev Dis* **8** (2021). <https://doi.org:10.3390/jcdd8110134>
- 59 Guo, H. *et al.* Intercalated disc protein Xinbeta is required for Hippo-YAP signaling in the heart. *Nature communications* **11**, 4666 (2020). <https://doi.org:10.1038/s41467-020-18379-8>
- 60 Tao, G. *et al.* Pitx2 promotes heart repair by activating the antioxidant response after cardiac injury. *Nature* **534**, 119-123 (2016). <https://doi.org:10.1038/nature17959>
- 61 Nadadur, R. D. *et al.* Pitx2 modulates a Tbx5-dependent gene regulatory network to maintain atrial rhythm. *Sci Transl Med* **8**, 354ra115 (2016). <https://doi.org:10.1126/scitranslmed.aaf4891>
- 62 Man, J. C. K. *et al.* Genetic Dissection of a Super Enhancer Controlling the Nppa-Nppb Cluster in the Heart. *Circ Res* **128**, 115-129 (2021). <https://doi.org:10.1161/CIRCRESAHA.120.317045>

- 63 Nahrendorf, M. Myeloid cell contributions to cardiovascular health and disease. *Nat Med* **24**, 711-720 (2018). <https://doi.org:10.1038/s41591-018-0064-0>
- 64 Cao, D. J. *et al.* Cytosolic DNA Sensing Promotes Macrophage Transformation and Governs Myocardial Ischemic Injury. *Circulation* **137**, 2613-2634 (2018). <https://doi.org:10.1161/CIRCULATIONAHA.117.031046>
- 65 Farbehi, N. *et al.* Single-cell expression profiling reveals dynamic flux of cardiac stromal, vascular and immune cells in health and injury. *eLife* **8** (2019). <https://doi.org:10.7554/eLife.43882>
- 66 Muhl, L. *et al.* Single-cell analysis uncovers fibroblast heterogeneity and criteria for fibroblast and mural cell identification and discrimination. *Nature communications* **11**, 3953 (2020). <https://doi.org:10.1038/s41467-020-17740-1>
- 67 dela Paz, N. G. & D'Amore, P. A. Arterial versus venous endothelial cells. *Cell Tissue Res* **335**, 5-16 (2009). <https://doi.org:10.1007/s00441-008-0706-5>
- 68 Vanlandewijck, M. *et al.* A molecular atlas of cell types and zonation in the brain vasculature. *Nature* **554**, 475-480 (2018). <https://doi.org:10.1038/nature25739>
- 69 Kalucka, J. *et al.* Single-Cell Transcriptome Atlas of Murine Endothelial Cells. *Cell* **180**, 764-779 e720 (2020). <https://doi.org:10.1016/j.cell.2020.01.015>
- 70 Fujimoto, N. *et al.* Single-cell mapping reveals new markers and functions of lymphatic endothelial cells in lymph nodes. *PLoS Biol* **18**, e3000704 (2020). <https://doi.org:10.1371/journal.pbio.3000704>
- 71 Gerarduzzi, C., Hartmann, U., Leask, A. & Drobetsky, E. The Matrix Revolution: Matricellular Proteins and Restructuring of the Cancer Microenvironment. *Cancer research* **80**, 2705-2717 (2020). <https://doi.org:10.1158/0008-5472.CAN-18-2098>
- 72 Nishioka, T. *et al.* Tenascin-C may aggravate left ventricular remodeling and function after myocardial infarction in mice. *Am J Physiol Heart Circ Physiol* **298**, H1072-1078 (2010). <https://doi.org:10.1152/ajpheart.00255.2009>
- 73 McCurdy, S. M. *et al.* SPARC mediates early extracellular matrix remodeling following myocardial infarction. *Am J Physiol Heart Circ Physiol* **301**, H497-505 (2011). <https://doi.org:10.1152/ajpheart.01070.2010>
- 74 Murry, C. E., Giachelli, C. M., Schwartz, S. M. & Vracko, R. Macrophages express osteopontin during repair of myocardial necrosis. *The American journal of pathology* **145**, 1450-1462 (1994).
- 75 Schellings, M. W. *et al.* Absence of SPARC results in increased cardiac rupture and dysfunction after acute myocardial infarction. *J Exp Med* **206**, 113-123 (2009). <https://doi.org:10.1084/jem.20081244>
- 76 Oka, T. *et al.* Genetic manipulation of periostin expression reveals a role in cardiac hypertrophy and ventricular remodeling. *Circ Res* **101**, 313-321 (2007). <https://doi.org:10.1161/CIRCRESAHA.107.149047>
- 77 Trueblood, N. A. *et al.* Exaggerated left ventricular dilation and reduced collagen deposition after myocardial infarction in mice lacking osteopontin. *Circ Res* **88**, 1080-1087 (2001). <https://doi.org:10.1161/hh1001.090842>
- 78 Monroe, T. O. *et al.* YAP Partially Reprograms Chromatin Accessibility to Directly Induce Adult Cardiogenesis In Vivo. *Dev Cell* **48**, 765-779 e767 (2019). <https://doi.org:10.1016/j.devcel.2019.01.017>

- 79 Xiao, Y., Leach, J., Wang, J. & Martin, J. F. Hippo/Yap Signaling in Cardiac Development and Regeneration. *Curr Treat Options Cardiovasc Med* **18**, 38 (2016). <https://doi.org/10.1007/s11936-016-0461-y>
- 80 Miao Cui, E. N. O. Protocol for Single-Nucleus Transcriptomics of Diploid and Tetraploid Cardiomyocytes in Murine Hearts. *STAR protocol* **1** (2020). <https://doi.org/10.1016/j.xpro.2020.100049>
- 81 Hahn, G., Ponce-Alvarez, A., Deco, G., Aertsen, A. & Kumar, A. Portraits of communication in neuronal networks. *Nat Rev Neurosci* **20**, 117-127 (2019). <https://doi.org/10.1038/s41583-018-0094-0>
- 82 Xiong, X. *et al.* Landscape of Intercellular Crosstalk in Healthy and NASH Liver Revealed by Single-Cell Secretome Gene Analysis. *Molecular cell* **75**, 644-660 e645 (2019). <https://doi.org/10.1016/j.molcel.2019.07.028>
- 83 Tirziu, D., Giordano, F. J. & Simons, M. Cell communications in the heart. *Circulation* **122**, 928-937 (2010). <https://doi.org/10.1161/CIRCULATIONAHA.108.847731>
- 84 Ellison, D. *et al.* Cell-cell communication enhances the capacity of cell ensembles to sense shallow gradients during morphogenesis. *Proceedings of the National Academy of Sciences of the United States of America* **113**, E679-688 (2016). <https://doi.org/10.1073/pnas.1516503113>
- 85 Patel, S. J., King, K. R., Casali, M. & Yarmush, M. L. DNA-triggered innate immune responses are propagated by gap junction communication. *Proceedings of the National Academy of Sciences of the United States of America* **106**, 12867-12872 (2009). <https://doi.org/10.1073/pnas.0809292106>
- 86 Ablasser, A. *et al.* Cell intrinsic immunity spreads to bystander cells via the intercellular transfer of cGAMP. *Nature* **503**, 530-534 (2013). <https://doi.org/10.1038/nature12640>
- 87 Parthasarathi, K. *et al.* Connexin 43 mediates spread of Ca<sup>2+</sup>-dependent proinflammatory responses in lung capillaries. *The Journal of clinical investigation* **116**, 2193-2200 (2006). <https://doi.org/10.1172/JCI26605>
- 88 Garcia-Dorado, D., Rodriguez-Sinovas, A. & Ruiz-Meana, M. Gap junction-mediated spread of cell injury and death during myocardial ischemia-reperfusion. *Cardiovasc Res* **61**, 386-401 (2004). <https://doi.org/10.1016/j.cardiores.2003.11.039>
- 89 Herculano-Houzel, S. The human brain in numbers: a linearly scaled-up primate brain. *Front Hum Neurosci* **3**, 31 (2009). <https://doi.org/10.3389/neuro.09.031.2009>
- 90 Bianconi, E. *et al.* An estimation of the number of cells in the human body. *Ann Hum Biol* **40**, 463-471 (2013). <https://doi.org/10.3109/03014460.2013.807878>
- 91 Rieckmann, J. C. *et al.* Social network architecture of human immune cells unveiled by quantitative proteomics. *Nature immunology* **18**, 583-593 (2017). <https://doi.org/10.1038/ni.3693>
- 92 Browaeys, R., Saelens, W. & Saeys, Y. NicheNet: modeling intercellular communication by linking ligands to target genes. *Nat Methods* **17**, 159-162 (2020). <https://doi.org/10.1038/s41592-019-0667-5>
- 93 Shalek, A. K. *et al.* Single-cell RNA-seq reveals dynamic paracrine control of cellular variation. *Nature* **510**, 363-369 (2014). <https://doi.org/10.1038/nature13437>
- 94 Ladoux, B. & Mege, R. M. Mechanobiology of collective cell behaviours. *Nat Rev Mol Cell Biol* **18**, 743-757 (2017). <https://doi.org/10.1038/nrm.2017.98>

- 95 Peyret, G. *et al.* Sustained Oscillations of Epithelial Cell Sheets. *Biophys J* **117**, 464-478 (2019). <https://doi.org:10.1016/j.bpj.2019.06.013>
- 96 Leybaert, L. *et al.* Connexins in Cardiovascular and Neurovascular Health and Disease: Pharmacological Implications. *Pharmacol Rev* **69**, 396-478 (2017). <https://doi.org:10.1124/pr.115.012062>
- 97 Epelman, S., Lavine, K. J. & Randolph, G. J. Origin and functions of tissue macrophages. *Immunity* **41**, 21-35 (2014). <https://doi.org:10.1016/j.immuni.2014.06.013>
- 98 Pittet, M. J., Garris, C. S., Arlauckas, S. P. & Weissleder, R. Recording the wild lives of immune cells. *Sci Immunol* **3** (2018). <https://doi.org:10.1126/sciimmunol.aag0491>
- 99 Honold, L. & Nahrendorf, M. Resident and Monocyte-Derived Macrophages in Cardiovascular Disease. *Circ Res* **122**, 113-127 (2018). <https://doi.org:10.1161/CIRCRESAHA.117.311071>
- 100 Scemes, E., Dermietzel, R. & Spray, D. C. Calcium waves between astrocytes from Cx43 knockout mice. *Glia* **24**, 65-73 (1998). [https://doi.org:10.1002/\(sici\)1098-1136\(199809\)24:1<65::aid-glia7>3.0.co;2-#](https://doi.org:10.1002/(sici)1098-1136(199809)24:1<65::aid-glia7>3.0.co;2-#)
- 101 Grienberger, C. & Konnerth, A. Imaging calcium in neurons. *Neuron* **73**, 862-885 (2012). <https://doi.org:10.1016/j.neuron.2012.02.011>
- 102 Svoboda, K., Denk, W., Kleinfeld, D. & Tank, D. W. In vivo dendritic calcium dynamics in neocortical pyramidal neurons. *Nature* **385**, 161-165 (1997). <https://doi.org:10.1038/385161a0>
- 103 Pnevmatikakis, E. A. *et al.* Simultaneous Denoising, Deconvolution, and Demixing of Calcium Imaging Data. *Neuron* **89**, 285-299 (2016). <https://doi.org:10.1016/j.neuron.2015.11.037>
- 104 Berens, P. *et al.* Community-based benchmarking improves spike rate inference from two-photon calcium imaging data. *PLoS computational biology* **14**, e1006157 (2018). <https://doi.org:10.1371/journal.pcbi.1006157>
- 105 Mukamel, E. A., Nimmerjahn, A. & Schnitzer, M. J. Automated analysis of cellular signals from large-scale calcium imaging data. *Neuron* **63**, 747-760 (2009). <https://doi.org:10.1016/j.neuron.2009.08.009>
- 106 Deneux, T. *et al.* Accurate spike estimation from noisy calcium signals for ultrafast three-dimensional imaging of large neuronal populations in vivo. *Nature communications* **7**, 12190 (2016). <https://doi.org:10.1038/ncomms12190>
- 107 Perez Koldenkova, V. & Nagai, T. Genetically encoded Ca(2+) indicators: properties and evaluation. *Biochimica et biophysica acta* **1833**, 1787-1797 (2013). <https://doi.org:10.1016/j.bbamcr.2013.01.011>
- 108 Mues, M. *et al.* Real-time in vivo analysis of T cell activation in the central nervous system using a genetically encoded calcium indicator. *Nat Med* **19**, 778-783 (2013). <https://doi.org:10.1038/nm.3180>
- 109 Inoue, M. *et al.* Rational Engineering of XCaMPs, a Multicolor GECI Suite for In Vivo Imaging of Complex Brain Circuit Dynamics. *Cell* **177**, 1346-1360 e1324 (2019). <https://doi.org:10.1016/j.cell.2019.04.007>
- 110 Chen, Q. *et al.* Imaging neural activity using Thy1-GCaMP transgenic mice. *Neuron* **76**, 297-308 (2012). <https://doi.org:10.1016/j.neuron.2012.07.011>
- 111 Ulbricht, C. *et al.* Intravital quantification reveals dynamic calcium concentration changes across B cell differentiation stages. *eLife* **10** (2021). <https://doi.org:10.7554/eLife.56020>

- 112 Wei, Q. *et al.* Maea expressed by macrophages, but not erythroblasts, maintains postnatal  
murine bone marrow erythroblastic islands. *Blood* **133**, 1222-1232 (2019).  
<https://doi.org:10.1182/blood-2018-11-888180>
- 113 Horning, A. M. *et al.* Single-cell RNA-seq reveals a subpopulation of prostate cancer cells  
with enhanced cell cycle-related transcription and attenuated androgen response. *Cancer  
research* (2017). <https://doi.org:10.1158/0008-5472.CAN-17-1924>
- 114 Dieterle, P. B., Min, J., Irimia, D. & Amir, A. Dynamics of diffusive cell signaling relays.  
*eLife* **9** (2020). <https://doi.org:10.7554/eLife.61771>
- 115 Verma, A., Antony, A. N., Ogunnaike, B. A., Hoek, J. B. & Vadigepalli, R. Causality  
Analysis and Cell Network Modeling of Spatial Calcium Signaling Patterns in Liver  
Lobules. *Frontiers in physiology* **9**, 1377 (2018).  
<https://doi.org:10.3389/fphys.2018.01377>
- 116 Sonnenberg, G. F. & Hepworth, M. R. Functional interactions between innate lymphoid  
cells and adaptive immunity. *Nature reviews. Immunology* **19**, 599-613 (2019).  
<https://doi.org:10.1038/s41577-019-0194-8>
- 117 Quinn, C. J., Coleman, T. P., Kiyavash, N. & Hatsopoulos, N. G. Estimating the directed  
information to infer causal relationships in ensemble neural spike train recordings. *J  
Comput Neurosci* **30**, 17-44 (2011). <https://doi.org:10.1007/s10827-010-0247-2>
- 118 Wibral, M. *et al.* Measuring information-transfer delays. *PLoS One* **8**, e55809 (2013).  
<https://doi.org:10.1371/journal.pone.0055809>
- 119 Schreiber, T. Measuring information transfer. *Physical review letters* **85**, 461-464 (2000).  
<https://doi.org:10.1103/PhysRevLett.85.461>